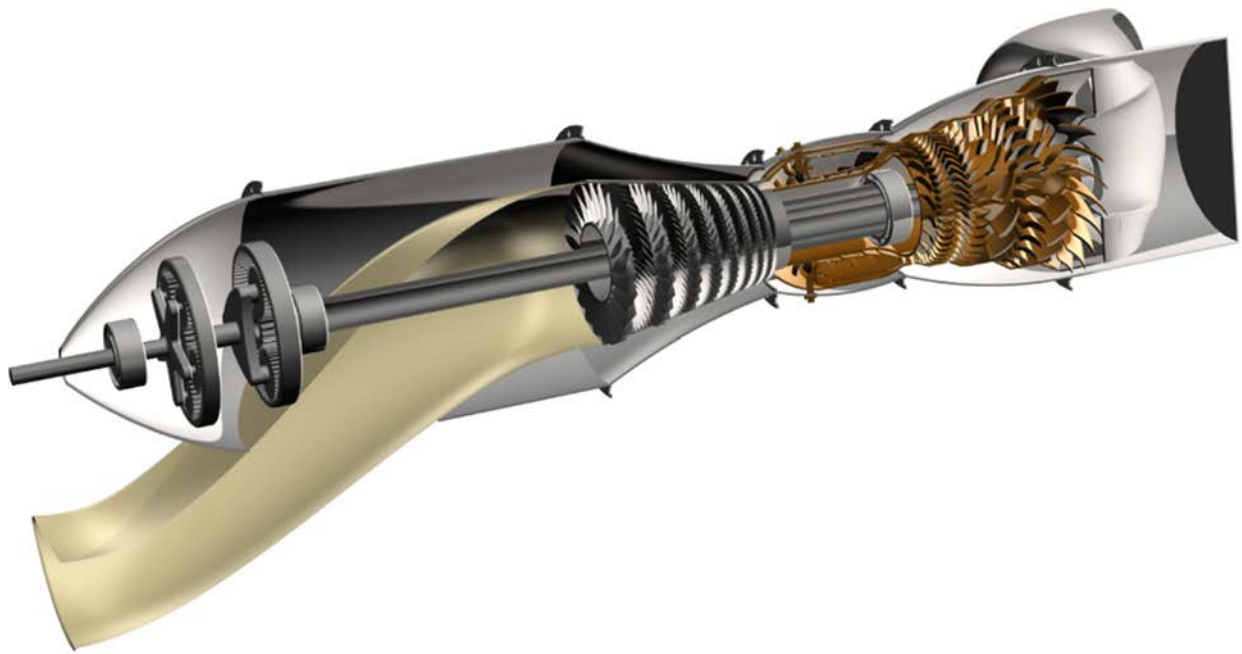

SF-1600: A Next Generation High Efficiency Turboprop for Single-Engine Aircraft



Faculty Advisors:

Saeed Farokhi and Ray Taghavi

Team Lead:

Thomas Row

Team Members:

Elliot Bicker

Alex Carnoali

Antonio Schoneich

Austin Tuggle

Christopher Bynum

Cody Hill

Juan Castro

Libby Stoops



Department of Aerospace Engineering

May 7th, 2017

SF-1600: A Next Generation High Efficiency Turboprop for Single-Engine Aircraft

Design Team:

Elliot Bicker
531124



Christopher Bynum
530767



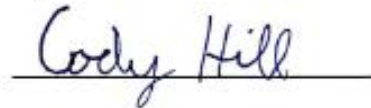
Alex Carnoali
808532



Juan Castro
808647



Cody Hill
531336



Thomas Row
808473
Team Lead



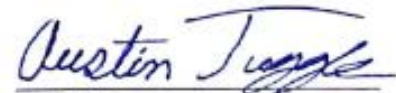
Antonio Schoneich
545336



Elizabeth Stoops
808557



Austin Tuggle
808545



Faculty Advisors

Dr. Saeed Farokhi
005092



Dr. Ray Taghavi
024860



Abstract

This report details the design of the SF-1600 turboprop replacement engine for the PT-6 in a next-generation turboprop trainer. The SF-1600 incorporates modern engine architecture and advanced technologies over the aging PT-6 including:

1. High-efficiency engine architecture
2. Higher cycle pressure ratio
3. Higher turbine inlet temperature
4. Ceramic matrix composite turbine blades, turbine nozzles, and combustor liners
5. Uncooled turbine blades and nozzles
6. TAPS injectors to improve efficiency and decrease emission

The primary design drivers for this engine were to reduce acquisition and life cycle costs, while providing more power efficiently and at a reduced weight. Advanced, high temperature materials are used to eliminate turbine cooling, significantly decreasing the turbine manufacturing cost, acquisition and operating costs associated with the high temperature components of this engine. Incorporating advanced material and manufacturing technologies in the SF-1600 drive down the cost of the engine while increasing its performance.

The SF-1600 offers a 33% decrease in PSFC, an 18% decrease in mass flow rate and an increase of 225 °R at the combustor exit when compared to the PT6A-68B. The following image shows the SF-1600 within the specified envelope, denoted by a blue box.

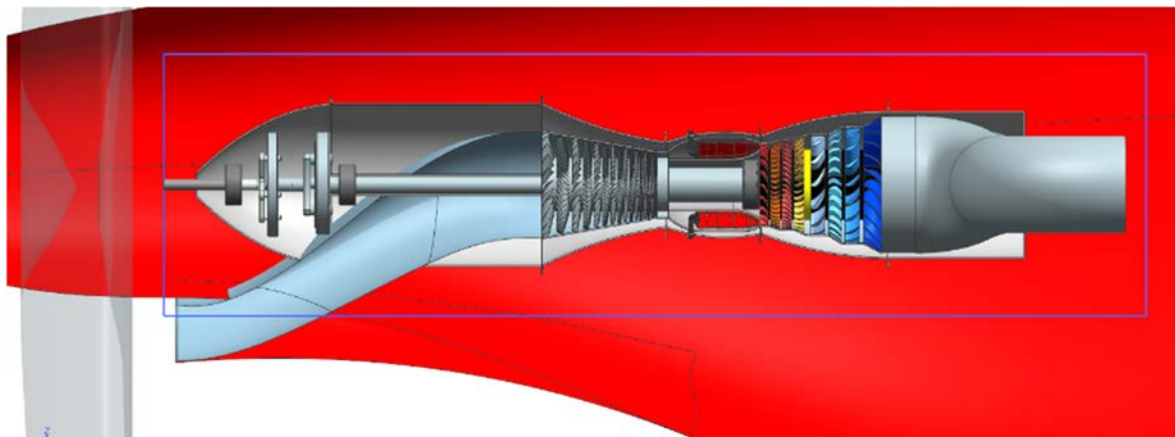


Figure 0.1: SF-1600 with PT6 Envelope

Table 0.1: SF-1600 Compliance Matrix

Performance			
Cruise Speed (kts)		337	
Cruise Mission Fuel Burn (lbs)		1166	
Cruise BSFC		0.378	
Takeoff BSFC		0.347	
Engine Weight (lbs)		136	
Engine Diameter (in)		13	
Engine Length (in)		62.5	
Trade Studies			
Engine Cycle Carpet Plots Page #	Cycle Summary Page #	Final Engine Flowpath Page #	Compressor Design Information Page #
10	12	76	41
Compressor Velocity Triangles Page #	Turbine Design Information Page #	Turbine Velocity Triangles Page #	
34	58	60	

Table 0.2: Engine Summary Table

Summary Data	
Design MN	0
Design Altitude	0
Design Shaft Horsepower	1600
Design BSFC	0.378
Design Overall Pressure Ratio	15
Design T4.1 (°R)	2560
Design Engine Pressure Ratio	15
Design Chargeable Cooling Flow (% @25)	0
Design Non-Chargeable Cooling Flow (% @25)	0
Design Adiabatic Efficiency for Turbines:	
HP Turbine	0.931
Power Turbine	0.932
Design Compressor Polytropic Efficiency	0.92
Design Shaft Power Loss (hp)	32.7
Design HP Shaft RPM	43400
Design PT Shaft RPM	34000
Additional Information	
Design HP/LP Shaft Off-Take Power	0
Design Customer Bleed Flow	7%

Table of Contents

Abstract.....	ii
Table of Contents.....	iv
List of Symbols.....	iii
List of Tables.....	iii
List of Figures.....	i
Acknowledgements.....	2
Introduction.....	3
1.0 Cycle Analysis.....	4
1.1 Design Philosophy.....	4
1.2 Engine Concepts for the SF-1600.....	4
1.3 Engine Components and Diagrams.....	6
1.4 Baseline Engine Cycle Analysis and Validation.....	7
1.4.1 On-Design Analysis of Baseline Engine.....	7
1.5 New Engine Cycle Analysis and Summary.....	8
1.5.1 On-Design Analysis of the SF-1600.....	9
1.5.2 Off-Design Analysis of the SF-1600.....	13
1.6 Performance Comparison with Baseline Engine.....	13
1.7 Interim Summary.....	15
2.0 Subsonic Inlet Design.....	15
2.1 Engine Inlet Design Philosophy.....	15
2.2 Inlet Sizing and Geometric Design.....	16
2.3 Inlet External Cowl Design.....	20
2.4 Inlet Materials and Structure.....	22
2.5 Anti-Icing Technology.....	23
2.6 Inlet Noise Control.....	23
2.7 Inlet Flow Station Data.....	24
3.0 Compressor Design.....	24
3.1 Compressor Inlet Flow Parameters.....	27
3.2 Compressor Exit Flow Parameters.....	29
3.2.1 Shaft RPM.....	29
3.3 Stage-by-Stage Analysis.....	29
3.3.1 3-D Blade Design.....	30
3.3.2 Stage Parameters.....	31
3.3.3 Number of Stages.....	36
3.3.4 Overall Compressor Parameters.....	38
3.4 Blade Structural Analysis.....	41
3.5 Compressor Rotor and Stator Blade Design.....	43
3.6 Stall Margin.....	44

3.7	Advanced Technologies	45
3.8	Compressor Flow Station Data	46
4.0	Combustion System	46
4.1	Pre-Diffuser Design.....	47
4.2	Flow Partitioning in Combustor.....	48
4.3	Combustor Geometric Parameters and Sizing	50
4.4	Combustor Efficiency	50
4.5	Temperature Profile.....	51
4.6	Material Selection	51
4.7	Fuel Injection.....	52
4.8	Ignition Source	53
4.9	Emissions	53
4.10	Three-View of the Combustor.....	54
4.11	Burner Flow Parameters.....	55
5.0	Axial-Flow Turbine Design	55
5.1	Pitchline Design Parameters.....	55
5.2	Turbine Flow Calculations and Aerothermodynamics.....	56
5.3	Turbine Blade and Annulus Sizing	61
5.4	Turbine Blade Material Selection and Stress Calculations	65
5.5	Smith Chart	66
5.6	Turbine Flow Parameters	67
6.0	Subsonic Nozzle.....	67
6.1	Nozzle Flow Station Data	68
7.0	Gearbox Design	68
7.1	Reduction Gearbox Design and Configuration	68
7.2	Reduction Gear Calculations.....	69
7.3	Accessory Gearing	71
7.4	Gearbox Systems Materials.....	71
7.5	Conclusions and Overall Design Parameters	72
8.0	Bearing Systems.....	73
8.1	Bearings Design	73
8.2	Bearing Materials	74
9.0	Flow Path Through the SF-1600.....	75
10.0	Manufacturing.....	75
10.1	Inlet materials.....	75
10.2	Compressor and Shaft New Technologies and Manufacturing Process	76

10.3	Turbine and Combustor Liner Materials and Manufacturing	76
10.4	Combustor Liner Materials and Manufacturing Process.....	78
10.5	SF-1600 Materials	78
11.0	Engine Weight Savings Analysis.....	78
12.0	Identification and Selection of Engine Subsystems.....	79
12.1	Oil and Lubrication System.....	80
12.1.1	Oil Selection	80
12.2	Engine Control System.....	81
12.3	Fuel System	83
13.0	Engine Airframe Integration	83
14.0	SF-1600 Exploded View	84
	References.....	86

List of Symbols

<u>Symbol</u>	<u>Description</u>	<u>Units</u>
A	Area	in ²
A _{HL}	Highlight Area	ft ²
A _M	Max Cowl Diameter	ft
A _R	Combustor Reference Area	in ²
AR	Aspect Ratio	~
A _{TH}	Throat Area	ft ²
b	Reaction Rate Parameter	~
B	Number of Rotor Blades	~
c	Chord	in
C	Velocity of Fluid in Absolute Frame of Reference	ft/s
C	Absolute Blade Velocity	ft/s
(Ch) _{ef}	Stalling Effective Static Pressure Rise Coefficient	~
CLP (θ)	Combustor Loading Parameter	~
C _P	Pressure Coefficient	~
C _z	Axial Velocity	ft/s
C _θ	Absolute Swirl Flow Velocity	ft/s
D	D-Factor	~
D _{add}	Additive Cowl Drag	lb
D _{spill}	Spillage Drag	lb
e _c	Polytropic efficiency	~
EI	Emissions Index	lbm/lbm
BPF	Blade Passing Frequency	Hz
h	Height	in
L	Length	in.
L _{Diff}	Diffuser Length	ft
L _{Duct}	Transition Duct Length	ft
M	Mach Number	~

\dot{m}	Mass Flow Rate	lb/s
N	Compressor Angular Velocity	RPM, rad/s
N	Number of Gear Teeth	~
o	Throat Size	in
P	Power	W, hp
P	Static Pressure	psi
PF	Pattern Factor	~
Pf	Profile Factor	~
P_t	Total Pressure	psia
$^{\circ}\text{R}$	Degree of Reaction	~
r	Radius	in
Re	Reynolds Number	~
RR	Total Reduction Ratio	~
s	Blade Spacing	in
SNOx	NOx Severity Parameter	~
t	Thickness	in
T	Temperature	$^{\circ}\text{R}$
T_c	Compressor Discharge Temperature or Coolant Temperature	$^{\circ}\text{R}$
T_g	Hot Gas Temperature	$^{\circ}\text{R}$
T_t	Total Temperature	$^{\circ}\text{R}$
T_w	Design Wall Temperature	$^{\circ}\text{R}$
U	Tangential Velocity	ft/s
V	Velocity	ft/s
V	Volume	in^3
W	Weight	lbf
W	Velocity of Fluid in Relative Frame of Reference	ft/s
wa	Combustor Inlet Airflow Rate	lb/s
war	Water-air-ratio	~

Greek Symbols

Symbol

Description

Units

ρ	Power	hp
α	Angle of Attack	$^{\circ}$
β	Relative Angle of Attack	$^{\circ}$
γ	Specific Heat Ratio	~
γ	Specific Weight	lb/hp
γ°	Stagger Angle	$^{\circ}$
η_d	Adiabatic Efficiency	~
θ_w	Inlet Average Wall Angle	$^{\circ}$
π_d	Total Pressure Ratio	~
ρ	Density	lb/in^3
ρ	Density	lbm/in^3
σ	Solidity	~
σ	Stress	psi
τ	Torque	lb-ft or N-m
Φ	Cooling Effectiveness Parameter	~
ϕ	Flow Coefficient	~

ϕ	Equivalence Ratio	~
ψ	Stage Loading Factor	~
ω	Angular speed	rpm or rad/s

Subscript

Definition

DZ	Dilution Zone
1 or 2 carrier	Reduction Stage Carrier Gear
GB	Gearbox
HL	Highlight
LPT	Low Pressure Turbine
M	Max
mat	Material
model	NX CAD Model
planet	Planet Gear
Prop	Propeller
PZ	Primary Zone
ring	Ring Gear
sun	Sun Gear
SZ	Secondary Zone
TH	Throat
TO	Takeoff
tot	Total

Acronym

Description

CMC	Ceramic Matrix Composite
CO	Carbon Monoxide
EPA	Environmental Protection Agency
GG	Gas Generator
HPT	High Pressure Turbine
LPT	Low Pressure Turbine
MS	Margin of Safety
NOX	Nitrogen Oxides
UHC	Unburned Hydrocarbons

List of Tables

Table 0.1: SF-1600 Compliance Matrix	iii
Table 0.2: Engine Summary Table	iii
Table 1.1: GasTurb Baseline Engine Summary and Validation	8
Table 1.2: Cycle Component Efficiency Parameters	9
Table 1.3: SF-1600 Summary of Optimized Cycle Parameters	12
Table 1.4: SF-1600 Off-Design Performance Characteristics	13
Table 1.5: Typical Training Mission Profile [8]	13
Table 1.6: Engine Characteristic Comparison	14
Table 1.7: PT-6 Training Mission	14
Table 1.8: PT-6 Long Range Cruise	14
Table 1.9: SF-1600 Training Mission	15

Table 1.10: SF-1600 Long Range Cruise	15
Table 2.1: Inlet Design and Performance Parameters at Cruise	22
Table 2.2: Inlet Flow Data	24
Table 3.1: Guidelines for Compressor Design Parameters [7]	25
Table 3.2: Compressor Geometry and Design Parameters	27
Table 3.3: Parameters Specified in GasTurb for Compressor Design	28
Table 3.4: Geometric Parameters at the Compressor Face	28
Table 3.5: Geometric Parameters at the Compressor Exit	29
Table 3.6: First Rotor and Stator De Haller and D-Factor Criteria	36
Table 3.7: Overall Compressor Parameters	39
Table 3.8: Overall Compressor Parameters at Pitchline for Each Stage	40
Table 3.9: Centrifugal Stress Parameters	42
Table 3.10: Calculating Ring Thickness and Stress	43
Table 3.11: Blade Design Parameters for the First Stage	44
Table 3.12: Compressor Design Data	46
Table 4.1: Flow Partitioning and Equivalence Ratios	48
Table 4.2: Combustor Zone Lengths	50
Table 4.3: Combustion Efficiency at Cruise	51
Table 4.4: Comparison of NOx Emissions	53
Table 4.5: Burner Flow Data	55
Table 5.1. Pitchline Inlet Design Parameters	55
Table 5.2. Stage Design for the High-Pressure Turbine	57
Table 5.3. Stage Design for the Low-Pressure Turbine	58
Table 5.4. Stage Degree of Reaction	58
Table 5.5: Temperatures and Pressures in the High Pressure Turbine	60
Table 5.6. Temperatures and Pressures in the Low Pressure Turbine	61
Table 5.7. Blade and Shroud Thicknesses	63
Table 5.8. Blade and Annulus Design Parameters	63
Table 5.9. Hub, Mean, and Tip Radii	63
Table 5.10: Turbine Blade Stresses and Margins of Safety	65
Table 5.11: Flow Coefficient and Stage Loading Factor for Each Stage	66
Table 5.12: HP Turbine Flow Data	67
Table 5.13: PT Flow Data	67
Table 6.1: SF-1600 Nozzle Parameters	68
Table 6.2: Exhaust Duct Flow Data	68
Table 6.3: Nozzle Flow Data	68
Table 7.1: Gearbox Material Properties [68]	71
Table 7.2: Gearing Angular Speeds and Torque at Takeoff	72
Table 7.3: Gearbox Design Parameters at Takeoff	72
Table 8.1: Bearing Material Properties [43-46]	74
Table 11.1: Component Weight	79
Table 11.2: Engine Dry Weight	79
Table 12.1: AeroShell 500 Oil Properties compared to Mil-Spec [56]	81
Table 13.1: SF 1600 Exploded View Material Legend	84

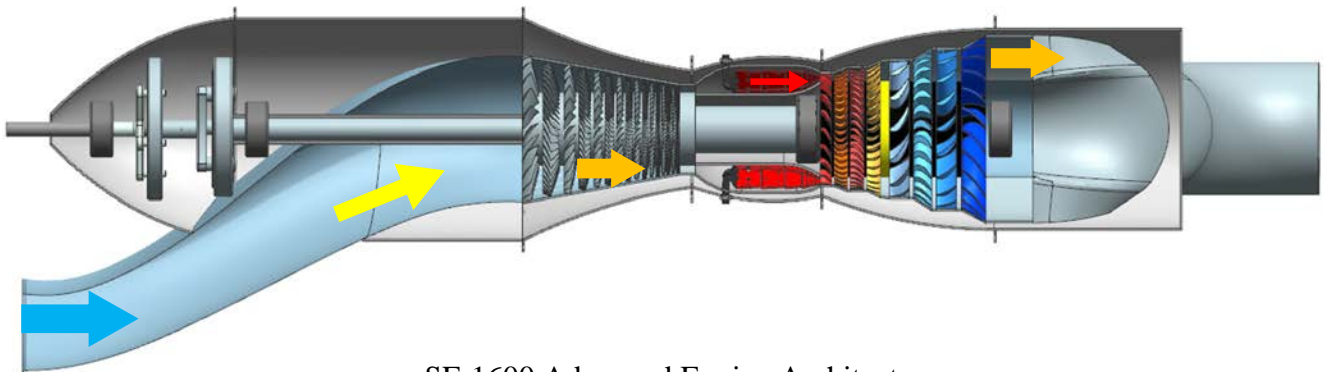
List of Figures

Figure 0.1: SF-1600 with PT6 Envelope	ii
Figure 1.1: PT-6 Engine Diagram.....	5
Figure 1.2: Axial Throughflow Turboprop Diagram.....	5
Figure 1.3: Engine Architecture.....	7
Figure 1.4: Carpet Plot of Engine Parameters Showing Specific Power, BSFC, OPR, T4, and Fuel Flow	10
Figure 1.5: Carpet Plot Showing Engine Mass, BSFC, OPR, T4, and Fuel Flow.....	11
Figure 2.1: Subsonic Inlet with Capture Ratio of 1	18
Figure 2.2: Nonuniformity in Velocity Profile Caused by Throat Contraction.....	19
Figure 2.3: Diffuser Geometry and Flow Regimes (left) Inlet Cross Section (right).....	20
Figure 2.4: SF-1600 Inlet-Airframe Integration	21
Figure 2.5: Anti-icing System for the SF-1600 Inlet Leading Edge.....	23
Figure 3.1: Solidity Trends from Wisler [20]	31
Figure 3.2: Aspect Ratio Trends from Wisler [20].....	31
Figure 3.3: Example of Velocity Triangles for a Rotor and Stator [2].....	32
Figure 3.4: Compressor Velocity Triangles at the Hub	33
Figure 3.5: Compressor Velocity Triangles at the Pitchline.....	33
Figure 3.6: Compressor Velocity Triangles at the Tip	33
Figure 3.7: Total Pressure and Temperature Ratios in Multi-Stage Compressor	37
Figure 3.8: Compressor Geometry.....	37
Figure 3.9: Compressor Inlet and Exit.....	38
Figure 3.10: Creep Rupture Strength Diagram [16]	41
Figure 3.11: Blade Cross-Sections.....	43
Figure 3.12: Geometric Parameters of Compressor Blades [7]	45
Figure 3.13: Stall Margin Chart [22]	45
Figure 3.14: Integrally Bladed Rotor Design Implementation	46
Figure 4.1: Typical Annular Combustor with Straight through Flow Burner [7].....	47
Figure 4.2: Effect of Splitter Vane on Diffuser Length [16]	48
Figure 4.3: CO and NOx Emissions as a Function of Primary Zone Temperature [16].....	48
Figure 4.4: Cooling Effectiveness, Methods, and Cooling Air [7].....	49
Figure 4.5: Lefebvre Parameter and Combustion Efficiency Correlation [7]	51
Figure 4.6: TAPS Fuel Injector [26].....	52
Figure 4.8: Isometric, Side, and Front View of the Combustor.....	54
Figure 4.7: Combustor Cutaway	54
Figure 5.1: Definition Sketch for Turbine Stage Analysis [7].....	56
Figure 5.2 Velocity Triangles at Hub, Mean and Tip.....	59
Figure 5.3: Campbell Frequency Diagram for a Turbine Blade [7]	62
Figure 5.4: Blade Design [7].....	62
Figure 5.5: Contour of Turbine.....	64
Figure 5.6: Smith Chart [31].....	66
Figure 6.1: SF-1600 bifurcated nozzle.....	67
Figure 7.1: Internal Reduction Gear Configuration [33]	68
Figure 7.2: Overall Gearbox System Configuration [35]	69
Figure 7.3: Bevel Gear Connection to Propeller Shaft	71
Figure 8.1: Ball and Roller Bearing Depiction [41]	73

Figure 8.2: Ball and Roller Bearing Configuration [40].....	73
Figure 8.3: Roller and Ball Bearing Components [43].....	74
Figure 8.1: SF-1600 Flow Path.....	75
Figure 10.1: Manufacturing Process of the Inlet [63].....	75
Figure 10.2: Bladed Ring [11].....	76
Figure 10.3: SIC CMC's Manufacturing Process [47].....	77
Figure 10.4: Cutout View of the SF-1600.....	78
Figure 12.1: Lubrication System Configuration [55].....	80
Figure 12.2: FADEC Block Diagram.....	82
Figure 13.2: U-Shaped Mount.....	83
Figure 13.2: O-Shaped Mount.....	83
Figure 13.3: SF-1600 Exploded View.....	85

Acknowledgements

Our team would like to thank Dr. Farokhi for teaching us everything we know about jet engines, and Dr. Taghavi for his support and teaching all of us fluid mechanics.



SF-1600 Advanced Engine Architecture

Introduction

The RFP [1] is calling for candidate engines to be used in the next generation turboprop trainer set to replace the PT-6 in the Pilatus PC-21. The new turboprop engine must be more efficient, higher performance, fit in the same engine envelope, and have a low acquisition and lifecycle costs.

The PC-21 is a turboprop powered trainer aircraft designed by Pilatus Aircraft. It was introduced in 2008 and is primarily used by the Swiss Air Force. It has a tandem cockpit and a low swept wing. Pratt and Whitney Canada designed the PT-6, which is used in the Pilatus. First run in 1960, it has had continuous updates throughout its 57 year life, however it is still the same architecture and has the same major cycle parameters as the original. Its architecture was applauded since its inception, no concentric shafts required; the power turbine shaft and the gas generator shaft are both short. However, in today's engineering world, it is behind times. Materials are lighter, concentric shafts are used extensively, and higher cycle pressure ratios are achievable with fewer axial stages.

The SF-1600 incorporates a number of new technologies and concepts to meet and exceed the RFP requirements. A throughflow design allows for higher efficiencies, lower cycle pressure losses and an ease of manufacturability. The use of ceramic matrix composites removes the need for turbine cooling which increases the turbine efficiency and decreases cost. This material also allows for a higher combustor exit temperature and reduced emissions from the combustor. Additionally, staged combustion will be used to further improve efficiency and decrease emissions.

1.0 Cycle Analysis

This section details the arrangement of the SF-1600 engine and the cycle analysis used in the performance assessment and design of the engine. The baseline and optimized cycles along with the comparison of key performance characteristics are included in this section.

1.1 Design Philosophy

Candidate turboshaft engines in response to the RFP [1] are required to increase take-off power to at least 1600 SHP, decrease fuel consumption over designated missions by 20%, and decrease total engine dry weight by 5%. Along with these hard requirements is the desire for the engine to have low acquisition and operating costs.

The baseline engine has a convoluted gas path that includes three 180° turn-around ducts, which cause significant total pressure losses. A goal of this design is to eliminate the total pressure losses that are accrued in turn-around ducts. An axial design gas path also simplifies manufacturing, inspection and overhaul costs. The price pain in turbine cooling is in both engine acquisition costs as well as a severe penalty on turbine efficiency. [3]. This will be accomplished with advanced materials such as Ceramic Matrix Composites(CMCs). To ensure the design will be production ready by the EIS of 2025, only technologies with a TRL of 6 or greater at the time of writing were selected.

1.2 Engine Concepts for the SF-1600

Three competing concepts were considered for this design analysis:

1. Original engine architecture with increased T4 and overall pressure ratio to bring the old engine up-to-date with higher component loadings.
2. High-efficiency engine architecture with a single spool gas generator and a single spool free power turbine with higher cycle pressure ratio and T4.
3. High-efficiency engine architecture with a two spool gas generator and a single spool free power turbine, with higher cycle pressure ratio and T4.

Concept 1 is a safe, but uses a complex and outdated engine architecture in turboprop engines. Here, we associate the outdated architecture with excessive gas path turning induced pressure losses. On the positive, it has a very short power turbine shaft length and does not require concentric shafts. This simplifies some manufacturing and reduces the weight slightly on the power turbine side, but accrues higher manufacturing costs and system weight in the remaining components with turn-around ducts. Ease of component accessibility, inspection and maintenance were additional drivers that led our team away from the complex PT-6 architecture.

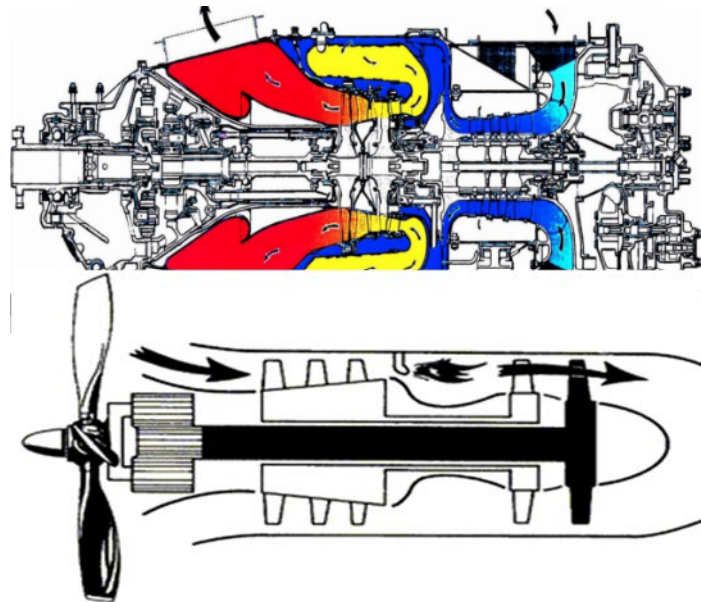


Figure 1.2: Axial Throughflow Turboprop Diagram

Concept 2 eliminates the complexity of the gas path with a high-efficiency engine architecture. This high-efficiency design uses a short concentric shaft that supports the gas generator spool and the power spool.

Concept 3 is similar to Concept 2 in overall architecture, except it has an additional gas generator spool for higher cycle pressure ratio and gas generator efficiency. This

increases the thermal efficiency of the engine at the cost of increased weight, complexity and cost.

Concept 2 is selected for the increased gas path efficiency and lower intake, burner, and exhaust complexity when compared to Concept 1. While Concept 3 offers a slightly increased thermal efficiency over Concept 2, the penalty of extra weight, manufacturing cost, and inspectability were deemed too high for the RFP criteria [1]. Concept 2 offers a lower cost design in manufacturing, acquisition, and maintenance.

1.3 **Engine Components and Diagrams**

Figure 1.3 illustrates the cycle schematic of the SF-1600, with the following eight primary components. The location of these components is shown in Figure 1.3 which was generated with GasTurb 12 [2]. The engine station numbers are defined as:

- | | | |
|----------------------|------------------|---------------|
| 1. Intake | 4. Burner Outlet | 5. LPT Outlet |
| 2. Compressor Face | 41. HPT Inlet | 6-8. Exhaust |
| 3. Compressor Outlet | 44. HPT Outlet | |
| 31. Burner Entrance | 45. LPT Inlet | |

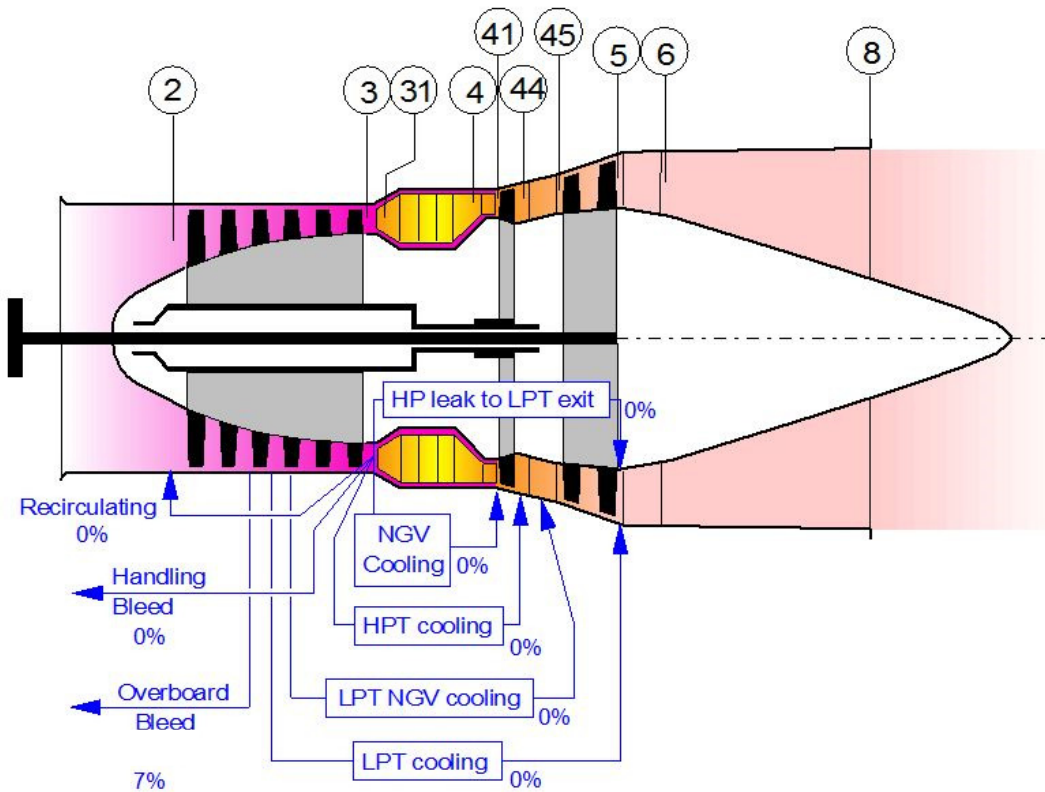


Figure 1.3: Engine Architecture

1.4 Baseline Engine Cycle Analysis and Validation

1.4.1 On-Design Analysis of Baseline Engine

The RFP [1] provides a cycle analysis of the existing engine. In order to validate the software and model, the baseline engine was modeled in GasTurb 12 [2] to match performance parameters of the existing engine. Table 1.1 shows the cycle summary generated for the baseline engine.

The baseline model generated with GasTurb does not match the provided model exactly (as explained in the RFP), but key cycle performance parameters matched exactly. For example, the turbine exit temperature was an exact match, mass flow at each station was within 0.01 lb/s and the shaft power was within 0.5% of the baseline engine. This demonstrates that the model created

accurately captures the baseline engine performance, and validates the results in our further optimization studies.

Table 1.1: GasTurb Baseline Engine Summary and Validation

Station	W lb/s	T R	P psia	WRstd lb/s		
amb		518.67	14.696		PWSD	= 1244.5 hp
1	10.580	518.67	14.696		PSFC	= 0.56582 lb/(hp*h)
2	10.580	518.67	14.696	10.580	Heat Rate	= 10471.9 BTU/(hp*h)
3	10.580	1076.70	138.907	1.613	V0	= 0.00 ft/s
31	9.870	1076.70	138.907		FN res	= 263.16 lb
4	10.066	2334.95	129.878	2.417	WF	= 0.19560 lb/s
41	10.564	2280.17	129.878	2.506	Therm Eff	= 0.24324
43	10.564	1804.39	40.282		P2/P1	= 1.00000
44	10.776	1791.00	40.282		TRQ	= 100.0 %
45	10.776	1791.00	40.081	7.342	P45/P44	= 0.99500
49	10.776	1494.71	16.945		Incidence	= 0.00000 °
5	10.776	1494.71	16.945	15.864	P6/P5	= 0.98000
6	10.776	1494.71	16.606		PwX	= 0 hp
8	10.776	1494.71	16.606	16.188	P8/Pamb	= 1.13000
Bleed	0.000	1076.70	138.906		WBld/w2	= 0.00000
-----					A8	= 72.16 in ²
Efficiencies:	isent	polytr	RNI	P/P	WCHN/w2	= 0.04710
Compressor	0.8204	0.8660	1.000	9.452	WCHR/w2	= 0.02000
Burner	0.9850			0.935	Loading	= 100.00 %
HP Turbine	0.8543	0.8356	1.561	3.224	WCLN/w2	= 0.00000
LP Turbine	0.8575	0.8436	0.635	2.365	WCLR/w2	= 0.00000
Generator	1.0000				PW_gen	= 1244.5 hp

HP Spool mech Eff	1.0000	Nom Spd	36830 rpm		eta t-s	= 0.74854
PT Spool mech Eff	1.0000	Nom Spd	30000 rpm			

hum [%]	war0	FHV	Fuel			
0.0	0.00000	18500.0	Generic			

1.5 New Engine Cycle Analysis and Summary

Two major design choices put limits on the cycle parameters for the SF-1600. The first choice was to utilize advanced turbine materials (i.e., ceramic matrix composites) suitable for uncooled turbine nozzles and blades. The CMC's have a maximum operating temperature of 2660 R [4, 5]. The maximum allowable T4 is thus set at 2560 °R, which is 100 °R below the maximum operating temperature of CMC's. The use of CMC's have been demonstrated on a GE engine, giving a TRL of 7 which is within the acceptable technology range for an EIS of 2025. This choice helps with the expected levels of temperature non-uniformity at the combustor exit, which is characterized by Pattern Factor (PF). The second choice was to use a single spool compressor for simplicity and

cost of manufacturing. The maximum pressure ratio efficiently produced by a single spool is 15 [6]. To minimize fuel burn as our optimization parameter, trade studies were conducted based on OPR, burner exit temperature, specific power, fuel flow and BSFC.

1.5.1 **On-Design Analysis of the SF-1600**

Before overall pressure ratio and burner exit temperature can be chosen, several minor design parameters must be acquired. These parameters include the pressure loss parameters across ducts and the burner as well as the combustor efficiency and mechanical efficiency in power

Table 1.2: Cycle Component Efficiency Parameters

Inlet PR	Burner PR	Turbine Interduct PR	Turbine Exit Duct PR	Nozzle PR	η_{burner}	$\eta_{\text{comp,poly}}$	$\eta_{\text{turb,poly}}$	HP η_{mech}	LP η_{mech}
0.99	0.95	0.995	0.99	1.07	0.99	0.90	0.92	0.995	0.99

transmission. Also required are the values for polytropic and isentropic efficiencies of the compressor and turbines. Table 1.2 shows all of these assumptions that are consistent with current industry practices.

Total pressure loss across turbine interconnect ducts, the burner, and the exhaust are all reduced from the baseline engine for the rationale that Concept 2, was chosen. The turbine achieves approximately 3% higher efficiency per 1% cooling reduction (according to Kerrebrock, 1992). This fact, allows our un-cooled turbine efficiency to be assumed above the current cooled turbines. The compressor efficiency is also improved in light of advanced blade profiles, through CFD optimization. For example, NASA Rotor 67 performance is measured to be superior to non-CFD-optimized compressor blades of the 1960's and 70's [7].

With the design choices outlined, we are ready to do a parametric cycle study and optimization. Carpet plots are presented in Figure 1.4 and Figure 1.5 in order to help explain the design point parameters.

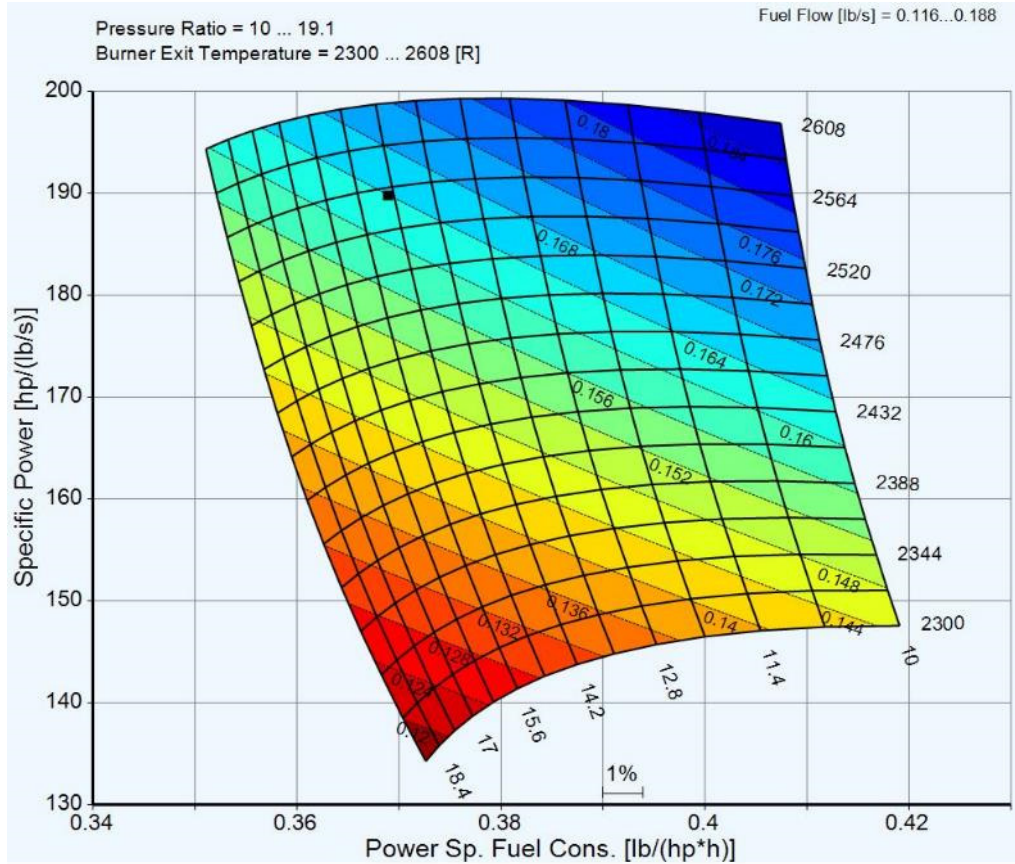


Figure 1.4: Carpet Plot of Engine Parameters Showing Specific Power, BSFC, OPR, T4, and Fuel Flow

From Figure 1.4 it is clear that overall pressure ratio is the primary driver for BSFC, and T4 is the primary driver for the engine specific power. BSFC, however, shows diminishing returns for a single value of T4 as cycle pressure ratio increases. For a given value of T4, with increasing pressure, the BSFC increases at a slower rate as the pressure rises. Also, the specific power drops as the cycle pressure ratio increases. This is due to the rising temperature of the gas at the compressor exit with pressure ratio. For a given T4 and increasing pressure ratio, the temperature rise across the burner drops, yielding reduced power in the exhaust stream to be extracted as shaft power. With rising T4, the specific power increases significantly, and the BSFC increases slightly. The specific power rise is due to the higher temperature rise across the burner. There is more power available to be extracted as shaft power.

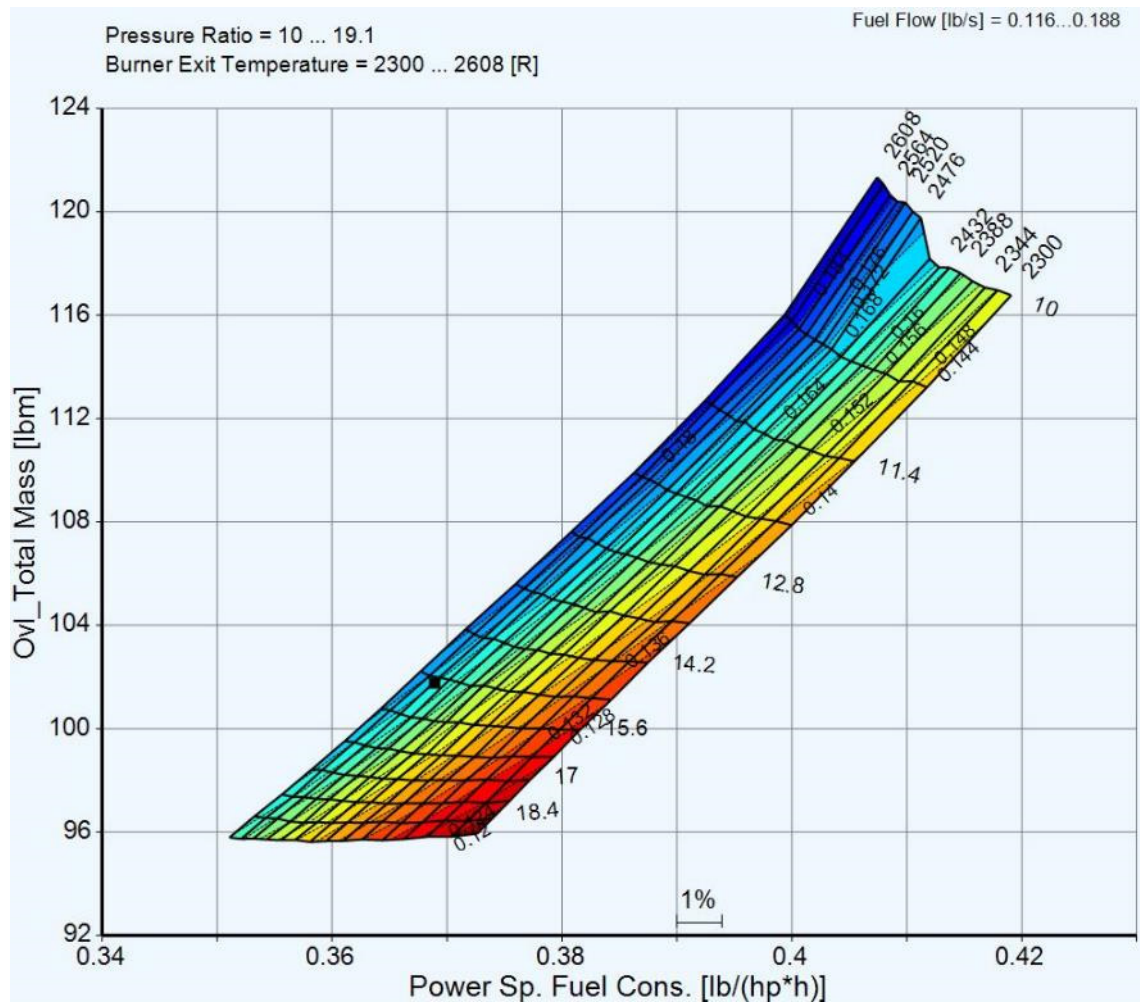


Figure 1.5: Carpet Plot Showing Engine Mass, BSFC, OPR, T4, and Fuel Flow

Now we examine the effect of design choices on engine weight, which is a critical parameter. Figure 1.5, shows the design and performance values with respect to engine mass. The complicated temperature-density-Mach number relations that give the flow area of the engine are a major driver of the engine weight. At higher pressures, the density of the gas is higher, so a smaller area is required for the same throughflow speed, hence the weight decreases. At higher temperatures, the gas is less dense, but the speed of sound increases, so the allowable gas speed through the engine increases (while maintaining the Mach number). These both affect the flow cross-section area and hence the engine weight. We note that at low pressure ratios, the effect of

the decreased density is more prevalent and the component weight increases with increasing temperature. At higher pressure ratios, the effect of increased speed of sound is more prevalent and the weight begins to decrease with increasing temperature.

Our team optimized the cycle performance by performing trade studies between pressure ratio and T4 to find the best possible efficiency while still maintaining a high specific power to keep the mass flow and engine weight down. The optimum point was found to be at the upper limit of both our pressure ratio and T4 limits. The increase in mass flow required to have a higher pressure ratio and maintain the required power output was more than offset by the increase in efficiency. The SF-1600 has a much higher T4 than the baseline engine and was therefore able to decrease the mass flow while both increasing the pressure ratio and shaft power delivered. This is

Station	W lb/s	T R	P psia	WRstd lb/s		
amb		545.67	14.696		PWSD	= 1600.0 hp
1	8.660	545.67	14.696		PSFC	= 0.37832 lb/(hp*h)
2	8.660	545.67	14.549	8.972	Heat Rate=	7021.6 BTU/(hp*h)
3	8.053	1263.66	218.235	0.846	V0	= 0.00 ft/s
31	8.053	1263.66	218.235		FN res	= 147.71 lb
4	8.222	2560.00	207.323	1.295	WF	= 0.16814 lb/s
41	8.222	2560.00	207.323	1.295	Therm Eff=	0.36276
43	8.222	1949.53	58.773		P2/P1	= 0.99000
44	8.222	1949.53	58.773		TRQ	= 100.0 %
45	8.222	1949.53	58.479	4.006	P45/P44	= 0.99500
49	8.222	1450.58	15.884		Incidence=	0.00000 °
5	8.222	1450.58	15.884	12.721	P6/P5	= 0.99000
6	8.222	1450.58	15.725		PWX	= 0 hp
8	8.222	1450.58	15.725	12.850	P8/Pamb	= 1.07000
Bleed	0.606	762.65	40.907		WBld/w2	= 0.07000
Efficiencies:					A8	= 73.63 in ²
Compressor	0.8587	0.9000	0.932	15.000	WCHN/w2	= 0.00000
Burner	0.9900			0.950	WCHR/w2	= 0.00000
HP Turbine	0.9305	0.9200	2.182	3.528	Loading	= 100.00 %
LP Turbine	0.9314	0.9200	0.841	3.682	WCLN/w2	= 0.00000
Generator	1.0000				WCLR/w2	= 0.00000
HP Spool	mech Eff	0.9950	Nom Spd	36830 rpm	PW_gen	= 1600.0 hp
PT Spool	mech Eff	0.9900	Nom Spd	30000 rpm	eta t-s	= 0.88705
hum [%]	war0	FHV	Fuel			
0.0	0.00000	18552.4	Generic			

Table 1.3:SF-1600 Summary of Optimized Cycle Parameters

also due to higher efficiency in un-cooled turbine, as demonstrated by Kerrebrock ,1992 and Farokhi, 2014. A cycle summary is shown in Table 1.3.

1.5.2 Off-Design Analysis of the SF-1600

GasTurb 12 was used to calculate the off-design cycle analysis at cruise, as specified in the RFP. Table 1.2 shows the SF-1600 key performance characteristics at cruise. The PSFC is especially critical as it is used in mission fuel calculations.

Table 1.4: SF-1600 Off-Design Performance Characteristics

Mach Number	PSFC	T4 (°R)	Mass flow (lb/s)	OPR
0.53	0.347	2350	7.207	14.3

1.6 Performance Comparison with Baseline Engine

As detailed in the RFP, the SF-1600 must demonstrate, at a minimum, a 20% decrease in fuel consumption over the aircraft missions, a 25% increase in supplied power, and a 5% decrease in engine weight. In order to find the fuel used over a mission, a mission profile must be established. An example of a typical mission profile is shown in Table 1.5 [8]. In order to calculate the fuel consumption,

Table 1.5: Typical Training Mission Profile [8]

this mission profile is simplified into cruising and combat maneuver segments as well as a long range cruise mission. These are presented in Tables 1.5 through 1.8.

Segment	Engine Rating, % RPM
Taxi and takeoff	60%
Takeoff and climb from 2000 to 2500 ft altitude	TO at 100%, then 95%
Four turns/stalls	1 min at 95% + 3 min at 60%
Climb from 2000 to 2500 ft altitude	95%
Four turn spins	60%
Climb from 2000 to 2500 ft altitude	95%
Four turn spins	60%
Four turns/stalls	1 min at 95% + 3 min at 60%
Climb from 2000 to 2500 ft altitude	95%
Aerobatics practice	95%
Descent and practice force landing	2 min at 95% + 6 min at 60%
Three circuits for landing practice	Average 80%
Approach, land, return taxi	60%
Trainee pilot allowance	95%

Table 1.6 shows the relevant characteristics for each engine and the percent difference. The SF-1600 meets all required specifications in the RFP and in all cases exceeds the required performance values. The long range cruise demonstrates a 30% fuel saving, which exceeds the RFP requirement.

Table 1.6: Engine Characteristic Comparison

	PT6A-68B	SF-1600	Percentage Difference
Aerobatic Mission Fuel Consumption (lbs)	1235	992	20% Reduction
Long Range Cruise Fuel Consumption (lbs)	1636	1243	30% Reduction
Power (hp)	1250	1600	28% Increase
Weight (lbm)	572	179	68% Reduction

Table 1.7: PT-6 Training Mission

	Takeoff	Climb	Cruise	Combat Maneuvers	Descent	Taxi
HP	1250	1250	1250	1250	480	160
BSFC	0.583	0.549	0.518	0.516	0.701	1.505
Time	0.033	0.083	0.5	1	0.33	0.33
Altitude	0	5000	10000	5000	5000	0
Fuel Used	24.3	57.2	324	645	112	80.3
Total Fuel (lbs)	1243					

Table 1.8: PT-6 Long Range Cruise

	Takeoff	Climb	Cruise	Descent	Taxi
HP	1250	1250	1250	480	160
BSFC	0.583	0.549	0.518	0.701	1.505
Speed			337		
Range			720		
Time	0.033	0.083	2.14	0.33	0.33
Altitude	0	5000	10000	5000	0
Fuel Used	24.3	57	1383	112	80.3
Total Fuel (lbs)	1657				

Table 1.9: SF-1600 Training Mission

	Takeoff	Climb	Cruise	Combat Maneuvers	Descent	Taxi
HP	1600	1360	1300	1600	480	160
BSFC	0.378	0.364	0.347	0.353	0.501	1.148
Time	0.033	0.083	0.5	1	0.33	0.33
Altitude	0	5000	10000	5000	5000	0
Fuel Used	20.16	41.25	226	564	80.16	61.2
Total Fuel	992					

Table 1.10: SF-1600 Long Range Cruise

	Takeoff	Climb	Cruise	Descent	Taxi
HP	1600	1360	1300	480	160
BSFC	0.378	0.364	0.347	0.501	1.148
Speed			337		
Range			720		
Time (hrs)	0.033	0.083	2.13	0.33	0.33
Altitude	0	5000	10000	5000	0
Fuel Used	20.2	41.3	964	80.16	61.2
Total Fuel	1166				

1.7 Interim Summary

The above engine cycle analysis confirms that the optimized cycle design parameters for the SF-1600 engine meets and exceeds the requirements put forth by the RFP [1]. Our performance improvements range from 20% in the aerobatic mission fuel consumption to 30% in long range cruise fuel consumption.

2.0 Subsonic Inlet Design

2.1 Engine Inlet Design Philosophy

Following design practices and guidelines laid out in Farokhi [7], the inlet for the SF-1600 is designed. The SF-1600 engine architecture is based on a fully axial flow engine, while the Pratt & Whitney PT6A-6B installed in the PC-21 follows a different design philosophy that incorporates four turn-around gas paths (inlet, compressor, combustor and turbine), followed by the fifth turn in the exhaust nozzles. The fully axial flow of the SF-1600 allows for a low weight and high efficiency inlet design. During low-speed, takeoff, and static conditions, the inlet acts as a nozzle, accelerating the flow to the design Mach number of 0.5 at the compressor face. Based on the Request for Proposal (RFP) [1] set forth by the AIAA, the following are major design drivers for the inlet:

- Low weight (Reduce engine weight by 5% compared to PT6A-6B [1])
- Cruise speed of 337 KTAS [1]
- Minimal installation drag
- Ease of maintenance and inspection (i.e., higher reliability)

The SF-1600 engine could be used in a number of aircraft configurations, but for this design it will be embedded in the front of the fuselage in the next generation single-engine turboprop, and so the inlet is located at the front of the aircraft, immediately below the propeller shaft. This inlet location will prevent most FOD (Foreign Object Debris) from entering the engine, as most FOD is created by landing gear, which is aft of the SF-1600 inlet in our design. The inlet is constructed from composite materials which are presented in the materials section of the report, including the construction process. The inlet cowl features anti-icing technology to maximize safety and reliability on the ground and during flight. In order to reduce the engine noise, a passive noise control strategy was considered by the team using Helmholtz resonators, as detailed by Kerrebrock, 1992,

describing the design of acoustic liners. Ultimately, this strategy was deemed unnecessary, as detailed in the Inlet Noise Control section.

2.2 Inlet Sizing and Geometric Design

The inlet of the SF-1600 is designed to provide axial flow to the compressor at the design Mach number with minimal distortion, total pressure loss, and drag. For preliminary design of the inlet for the SF-1600, the duct flow through the inlet is considered to be adiabatic. This assumption simplifies calculations by ensuring a constant total temperature throughout the inlet. Typical turboprop compressors operate with an inlet axial Mach number of 0.5-0.55 [1]. For the SF-1600, a Mach number of 0.5 was selected by the design team.

The two important parameters for determining losses incurred in an inlet are the inlet adiabatic efficiency, η_d , which is also related to the inlet total pressure recovery, π_d . These values are defined in equations 2.1 and 2.2 and are related in equation 2.3.

$$\eta_d = \frac{\left(\frac{P_{t2}}{P_o}\right)^{\frac{\gamma-1}{\gamma}} - 1}{\frac{\gamma-1}{2} M_o^2} \quad \text{Eqn. 2.1}$$

$$\pi_d = \frac{P_{t2}}{P_{t0}} \quad \text{Eqn. 2.2}$$

$$\pi_d = \left(\frac{1 + \eta_d \frac{\gamma-1}{2} M_o^2}{1 + \frac{\gamma-1}{2} M_o^2} \right)^{\frac{\gamma}{\gamma-1}} \quad \text{Eqn. 2.3}$$

According to Farokhi, subsonic cruise inlets have total pressure recoveries of 0.995-0.997 using modern design techniques [1], this yields total pressure recovery for the SF-1600 of 0.996, allowing adiabatic efficiency to be calculated using equation 2.3 giving a value of 0.978. Using the cruise speed prescribed in the RFP, a cruise Mach number of 0.528 is obtained [1]. Next for the capture area sizing, an A_0 of 0.28 ft² is calculated using the mass flow rate, cruise speed, and air density. Now the inlet area sizing at the compressor face can be performed using continuity, as shown in equation 2.4, obtaining A_2 of 0.272 ft². The difference in A_0 and A_2 areas is very

small, which is expected due to the small difference in Mach number or velocities between the two engine stations.

$$\frac{A_0}{A_2} = \frac{M_2}{M_0} \left(\frac{1 + \frac{\gamma-1}{2} M_0^2}{1 + \frac{\gamma-1}{2} M_2^2} \right)^{\frac{\gamma+1}{2(\gamma-1)}} \quad \text{Eqn. 2.4}$$

Since the cruise Mach number of 0.528 is very close to the desired Mach number of 0.5 at the compressor face, there is no need for external pre-diffusion of the flow, and thus the freestream capture area ratio is 1. This capture ratio will cause additive drag associated with the capture streamtube [7] to vanish in cruise, as calculated by equation 2.5. A capture ratio of 1 also means that flow conditions at the highlight will be the same as freestream conditions.

Figure 2.1 shows an example capture streamtube for the SF-1600, with values at station 0 equal to values at station 1.

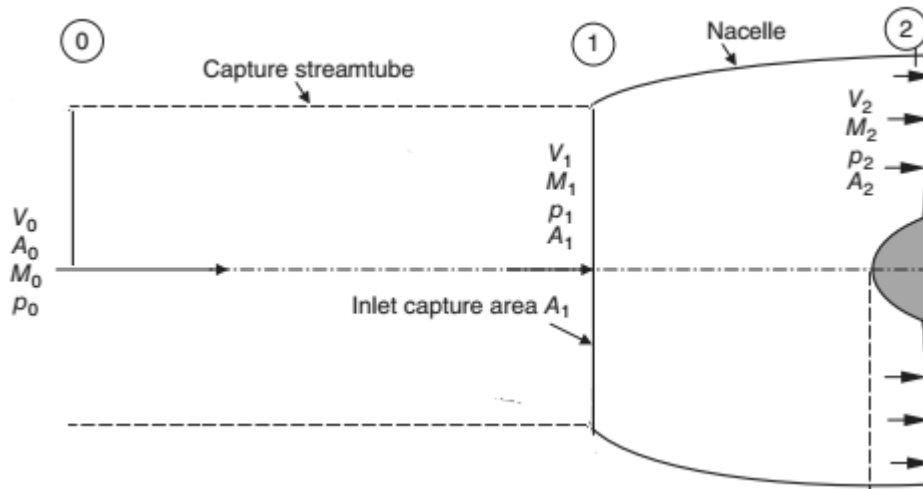


Figure 2.1: Subsonic Inlet with Capture Ratio of 1

$$D_{add} = \dot{m}_0(V_1 - V_0) + (p_1 - p_0)A_1 \quad \text{Eqn. 2.5}$$

The inner lip contour of the inlet from the highlight to the throat acts as a short subsonic nozzle, accelerating the flow. This acceleration is non-uniform, and creates a non-uniform velocity profile at the throat as shown in Figure 2.2. In order to keep the over-shoot in velocity profile in

the flow subsonic, Farokhi recommends a mass-averaged Mach number less than or equal to 0.75 at the throat. The mass-averaged Mach for the SF-1600 inlet is set to 0.56 at the throat in order to allow for future engine growth, allowing throat area to be sized using an isentropic relation similar to equation 2.4. This area contraction from highlight to throat is elliptical in shape with semi-major and minor axes, a and b [10]. The highlight and throat shapes are near ellipses contoured to the shape of the trainer which transition into a circle at the compressor face. The fineness ratio for the contraction is defined as a/b , with higher values producing a lower bluntness at the highlight. Since the role of a trainer will require high tolerance to flow angularity, the cowl lip is relatively blunt following NASA inlet design practices with a/b set to 1.25 [7].

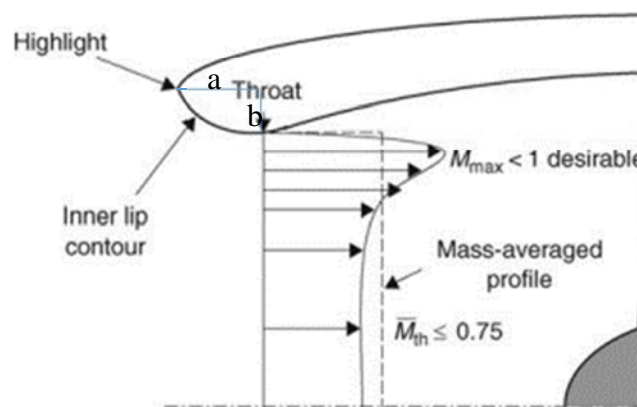


Figure 2.2: Nonuniformity in Velocity Profile Caused by Throat Contraction

Beyond the throat, the flow will decelerate until it reaches the compressor face, causing a static pressure rise in the inlet. This pressure rise is known as an adverse pressure gradient in aerodynamics, and can cause boundary layer separation in the inlet [7]. In order to prevent this separation, the average wall angle of the inlet, θ_w , is restricted based on Figure 2.3. With an area ratio of 1.04, the average wall angle can be upwards of 18° before stalling occurs [55]. Following design guidelines from NASA, the wall contour of the inlet wall is set to be a cubic with an inflection point at half the diffuser length in order to prevent boundary layer separation [10].

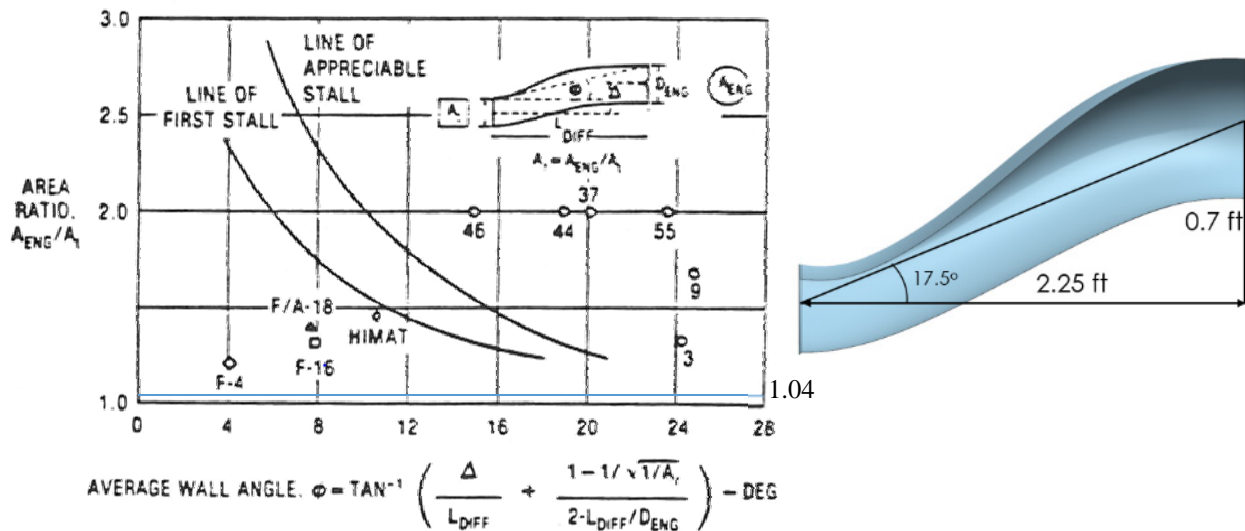


Figure 2.3: Diffuser Geometry and Flow Regimes (left)
Inlet Cross Section (right)

2.3 Inlet External Cowl Design

Performance of an air intake system at high speeds is governed by its external cowl drag characteristics. It is already known that with an inlet capture ratio of 1, additive, or pre-entry drag is 0, so this component of inlet drag is minimized. The maximum cowl diameter exposed to the flow, A_M , can be any value that satisfies the RFP requirement of a maximum diameter of 19 inches as wave drag is not an issue at the cruise Mach number of 0.53. After placement of the engine, it was determined that A_M is 4.9 inches.

Along with additive drag, there are two more external forces which act on the SF-1600 inlet outside of cruise conditions, namely spillage drag and lip suction force. Spillage drag is the difference between the additive drag and the inlet lip suction force. Lip suction is the resultant force due to a low-pressure zone that is created by the increased velocity over the outside of the cowl from spillage and will cancel out approximately half of spillage drag, but the actual value must be calculated experimentally. Spillage drag can be calculated theoretically for conditions other than cruise using Equation 2.7, where K is a coefficient for the effect of lip suction [Ref 58].

$$D_{spill} = K * (\dot{m} * [V_1 - V_0] + A_1 * [P_1 - P_0])$$

Eqn 2.6

During engine-out conditions, spillage drag will increase as there will be a blockage in the engine core, thus the air flow spills around the inlet cowl. [7]. This increase in flow spillage will cause an adverse pressure gradient on the outside cowl of the inlet, as flow moving around the cowl will decelerate compared to during operational engine conditions. This adverse pressure gradient will facilitate flow separation, further increasing drag during engine-out conditions [7]. Table 2.1 gives values for succinct characteristics of the SF-1600 inlet. Figure 2.4: SF-1600 Inlet-Airframe Integration shows the integration of the inlet into a PC-21, with the front view displaying the fairing for the inlet and a cutaway side view showing inlet offset.

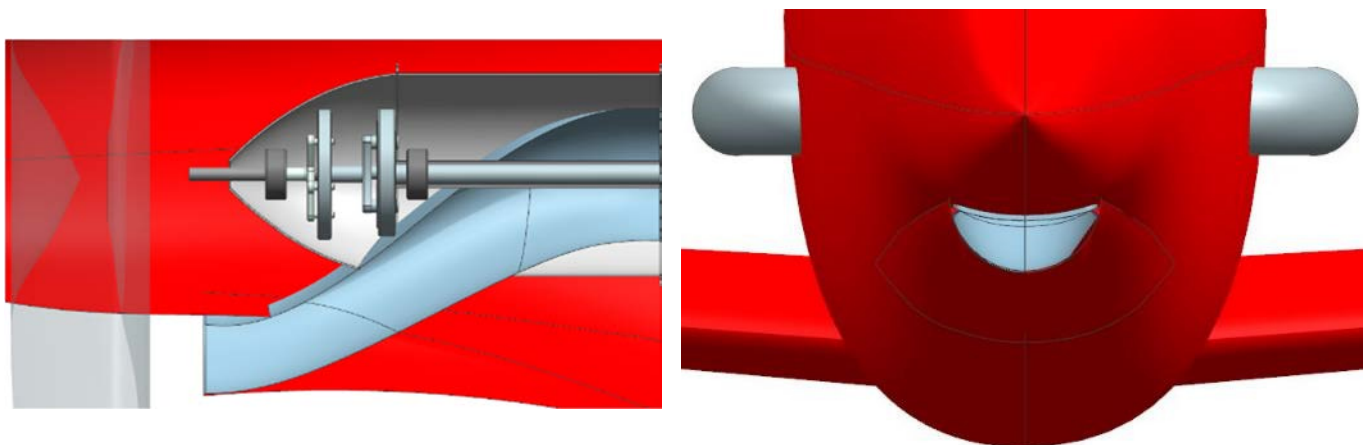


Figure 2.4: SF-1600 Inlet-Airframe Integration

Table 2.1: Inlet Design and Performance Parameters at Cruise

Parameter	Symbol	Value
Specific Heat Ratio	γ	1.4
Static Pressure (psia)	P_0	10.1
	$P_1=P_{HL}$	10.1
	P_{TH}	9.9
	P_2	10.3
Total Pressure (psia)	P_{t0}	12.21
	$P_{t1}=P_{tHL}$	12.21
	P_{tTH}	12.21
	P_{t2}	12.16
Mach Number (-)	M_0	0.528
	$M_1=M_{HL}$	0.528
	M_{TH}	0.56
	M_2	0.5
Area (ft ²)	A_0	0.269
	$A_1=A_{HL}$	0.269
	A_{TH}	0.259
	A_2	0.280
Transition Duct Length (ft)	L_{Duct}	2.2
Diffuser Length (ft)	L_{Diff}	2.25
Max Cowl Diameter (ft)	A_M	0.41
Adiabatic Efficiency (-)	η_d	0.978
Total Pressure Ratio (-)	π_d	0.996
Additive Cowl Drag (lb)	D_{add}	0
Lip Contraction Ratio (-)	A_{HL}/A_{TH}	1.04
Cowl Lip Fineness Ratio (-)	a/b	1.25

2.4 Inlet Materials and Structure

The inlet for the SF-1600 is constructed from an S2-glass cloth/epoxy composite, with the leading edge and structurally integral points constructed from an S2 aramid blend to improve damage tolerance, as recommended by Dr. Richard Hale [8]. Dr. Hale suggested that the minimum thickness for this composite layup be four to six layers of cloth thick. The design team ultimately chose a thickness of 6 plies to be on the safe side of Dr. Hale's suggestion. Based on this, the weight of the composite material in the inlet can be calculated, and is found to be 3.25 lbs for the selected six layer thickness, based on a fabric weight of 8.9 oz/yd² and an epoxy weight of 3 oz/yd² [56].

2.5 Anti-Icing Technology

It is imperative to the operation of the inlet that ice doesn't form at any point, as this could lead to a change in the lip shape, inlet distortion and engine compressor stall, which may even lead to surge. Also, ice that forms could break off and flow into the engine, damaging internal components. This leads to the necessity of an anti-icing system rather than a de-icing system, as ice cannot be allowed to form whatsoever on the inlet. In order to prevent ice formation, the inlet

utilizes electric heating elements which keep the leading edge of the inlet at an elevated temperature, preventing ice cap formation [12]. A schematic for the structure of the de-icing system is shown in

Figure 2.5.

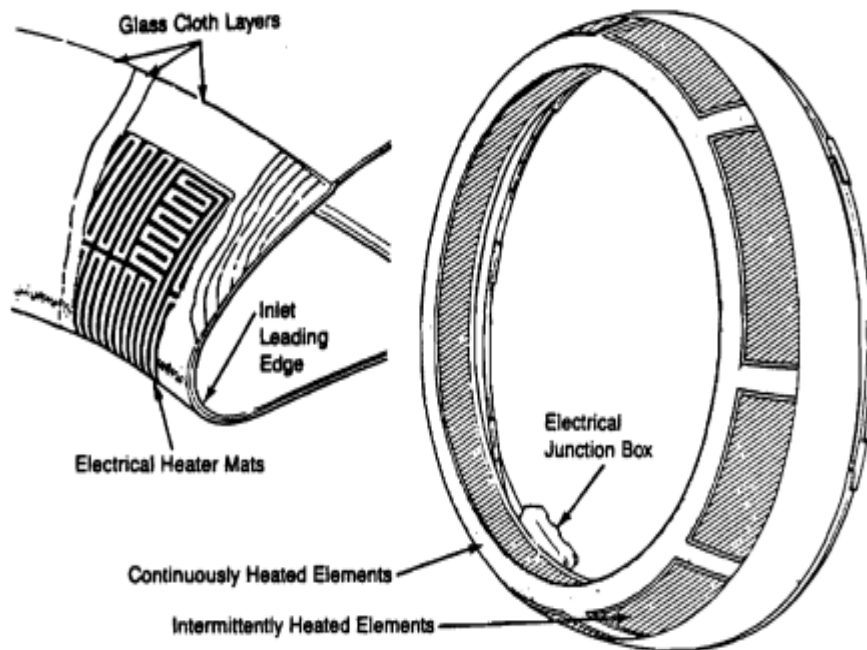


Figure 2.5: Anti-icing System for the SF-1600 Inlet Leading Edge

2.6 Inlet Noise Control

On turboprop engines, the propeller generates low-frequency noise (due to lower RPM) which is generally difficult to reduce via passive measures. Noise from the engine, however, can be suppressed by passive methods using an acoustic liner consisting of Helmholtz resonators tuned to the dominant compressor blade passing frequency and by taking advantage of the S-duct transition from the highlight to the compressor face. This represents true and tried practice in aircraft industry. The liner will be a honeycomb aluminum composite to maintain structural stiffness during flight with a drilled S2-glass perforated face sheet [57]. These Helmholtz

resonators have a fluid in their neck oscillate with a natural frequency that depends on the geometry of the cavity and the speed of sound of the gas [13]. The blade passing frequency of the compressor blades can be found using the number of rotor blades, B , and the compressor angular velocity in RPM, N via equation 2.8.

$$f_B = \frac{B*N}{60} \quad \text{Eqn. 2.7}$$

This gives a blade passing frequency of 18739 Hz, which is near the top of the audible range for humans at 20 kHz. Since the frequency of the noise from the compressor is so high, the low frequency noise from the propeller will be dominant. Based on this, the use of an acoustic liner in the inlet was deemed unnecessary for the turboprop trainer application, as the added weight of 4.3 lbs [56,57] and cost of manufacturing to integrate the liner inside the inlet duct outweigh the noise reduction benefit.

2.7 Inlet Flow Station Data

Table 2.2: Inlet Flow Data

Flow Station Data: Inlet	
Inflow (lb/s)	8.66
Corrected Inflow (lb/s)	8.66
Inflow Total Pressure (psi)	14.7
Inflow Total Temperature (°R)	545.7
Inflow Fuel-air-Ratio	0
Inflow Mach #	0.53
Inflow Area (in ²)	38.74
Total Pressure Ratio	0.996

3.0 Compressor Design

This section outlines the aerodynamic design of the compression system for the SF-1600 turboprop engine. Therefore, this chapter includes the design guidelines and assumptions, flow parameters, stage-by-stage analysis, 3-D blade design, material selection, and structural analysis for the axial-flow compressor. In pursuit of a high-efficiency engine architecture, the design team

opted for an axial-flow compressor operating on a single spool in the SF-1600 engine. To start the design process, the inlet flow conditions and the cycle pressure ratio are integrated into the compressor design. The shaft rotational speed (RPM) is established based on the design choice of the relative tip Mach number for the first stage rotor. Following this decision, the detailed stage-by-stage analysis for the three stream surfaces at the hub, pitchline, and tip develops. Optimization cycles of other design variables—degree of reaction, stage loading parameter, De Haller criterion, and diffusion factor (D-Factor)—are performed to determine the number of stages and to calculate stage characteristics that are specified in the compressor section of the AIAA RFP [1]. The design team performed the three stream surface design at the hub, pitchline, and tip to achieve this objective.

For the 3-D design of the blades, the SF-1600 engine compressor adopts the “free vortex” design. This assumption determines the swirl profile downstream of the rotor in the spanwise direction. In addition to free vortex design, the team assumed a non-repeated stage design concept with no pre-swirl. Since the projected size of the compressor is small, constant hub radius across the compressor length is selected to maximize the blade height at the exit [7]. With these design choices, the hub-to-tip radius ratio and constant hub radius are then selected. Subsequently, the velocity triangles for the hub, pitchline, and tip streamlines are calculated. The compressor team used the design guidelines on key parameters from the range of values that express modern industry practice listed in Table 3.1.

Table 3.1: Guidelines for Compressor Design Parameters [7]

Parameter	Range of Values	Typical Value
Flow Coefficient, ϕ	$0.3 \leq \phi \leq 0.9$	0.6
D-Factor	$D \leq 0.6$	0.45
Axial Mach number, M_z	$0.3 \leq M_z \leq 0.6$	0.55
Tip Tangential Mach Number, M_T	1.0-1.5	1.3
Degree of Reaction	$0.1 \leq R \leq 0.90$	0.5 (for $M < 1$)
Reynolds number based on Chord	$300,000 \leq Re_c$	> 500,000

Tip relative Mach number (1 st Rotor)	$(M_{1r})_{tip} \leq 1.7$	1.3-1.5
Stage average solidity	$1.0 \leq \sigma \leq 2.0$	1.4
Stage average aspect ratio	$1.0 \leq AR \leq 4.0$	<2.0
Polytropic efficiency	$0.85 \leq e_c \leq 0.92$	0.90
Hub rotational speed	$\omega_{rh} \leq 380$ m/s	300 m/s
Tip rotational speed	$\omega_{rt} \sim 450 - 550$ m/s	500 m/s
Loading Coefficient	$0.2 \leq \psi \leq 0.5$	0.35
DCA Blade (range)	$0.8 \leq M \leq 1.2$	Same
NACA-65 Series (range)	$M \leq 0.8$	Same
De Haller criterion	$W_2/W_1 \geq 0.72$	0.75
Blade leading-edge radius	$r_{L.E.} \sim 5-10\%$ of t_{max}	5% t_{max}
Compressor pressure ratio per spool	$\pi_c < 20$	up to 20
Axial gap between blade rows	$0.23 c_z$ to $0.25 c_z$	$0.25 c_z$
Aspect ratio, fan	$\sim 2-5$	< 1.5
Aspect ratio, compressor	$\sim 1-4$	~ 2
Taper ratio	$\sim 0.8-1.0$	0.8

Following the modern design practices on solidity and aspect ratio trends from David Wisler of General Electric (GE), the design team selected a high solidity, low aspect ratio blading for the SF-1600 compressor [18]. This selection leads to blade chord and blade spacing calculations at the pitchline, which establishes the number of blades per stage for the rotor and stator. The chosen blade chord must be compared to the minimum chord length that is required for the turbulent boundary layer formation on the blade [7].

$$Re_c = \frac{W_{1m} * c_m}{\nu_1} \geq 300,000 \quad \text{Eqn. 3.1}$$

At the cruise altitude, the minimum chord length is calculated to be 0.60 in. The design team chose the chord length of 1.28 due to the higher aspect ratio to help with stall margin [7]. This is based on the modern industry aspect ratio trends outlined by David Wisler from GE [18].

In addition, the centrifugal stress analysis determines the material selection for the rotor and stator blades. Annulus stress analysis selects the size of the integrally bladed ring (bling) [7]. Important parameters dictate the success of the compressor design, and these criteria include De Haller and D-Factor. Also, stall margin is an essential consideration for compressor design.

The axial compressor for the SF-1600 compressor turboprop engine includes eight stages with a cycle pressure ratio of 15 at design takeoff conditions. The hub-to-tip radius ratio of 0.5 and the tip tangential Mach number of 1.3 result in an operating shaft rotational speed of 46,400 RPM and a relative tip Mach number of 1.16 for the first rotor. The annulus area at the inlet of the compressor is 34.6 in² and the annulus area at the exit of the compressor is 5.02 in², which makes the last stator blade height 0.38 in. The achieved total pressure ratio in the SF-1600 compressor is 15.02. Other important parameters are summarized in Table 3.2.

Table 3.2: Compressor Geometry and Design Parameters

Parameter	Value
π_c	15.02
τ_c	2.36
P_{t1}	14.7 psi
T_{t1}	546 °R
P_{t2}	221 psi
T_{t2}	1,290 °R
e	0.92
ω	43,400 RPM
η	0.859
r_{h1}	1.92 in
r_{t1}	3.83 in
r_{h2}	1.92 in
r_{t2}	2.35 in
A_1	34.6 in ²
A_2	5.02 in ²

3.1 Compressor Inlet Flow Parameters

For the inlet properties, the total temperature, total pressure, and mass flow rate are given by GasTurb analysis [15]. In addition, GasTurb confirms the design axial Mach number at the compressor face determined from inlet calculations. The given parameters from GasTurb and the subsequent inlet design are detailed in Table 3.3.

Table 3.3: Parameters Specified in GasTurb for Compressor Design

Parameter	Measurement
Total Pressure, P_{t1}	14.7 psi
Total Temperature, T_{t1}	546 °R
Air Mass Flow Rate, \dot{m}_{dot}	8.66 lb _m /s
Axial Mach Number, M_{z1}	0.5
Static Pressure, P_1	12.4 psi
Static Temperature, T_1	520 °R
Density, ρ_1	0.0020 slug/ft ³

The driving factors determined from this portion of the design process include: axial Mach number and hub-to-tip radius ratio. The axial velocity is derived from M_{z1} and a_1 , resulting in a C_{z1} of 559 ft/s. Stemming from the former calculation, the continuity equation for steady, uniform flow establishes the sizing of the compressor inlet face [7]

$$\dot{m} = \rho AV \tag{Eqn. 3.2}$$

The team made a design choice on a hub-to-tip radius ratio of 0.5 [20]. This assumption along with the calculated compressor face area enables the calculation of the hub and the tip radii [7]. The tip radius is calculated from Equation 3.3 while the hub radius is consequently derived from the hub-to-tip radius ratio.

$$r_{t1} = \sqrt{\frac{A_1}{\pi} \left[1 - \left(\frac{r_{h1}}{r_{t1}} \right)^2 \right]} \tag{Eqn. 3.3}$$

Lastly, the pitchline radius is at the average of the hub and the tip radii. The important geometric parameters at the face of the compressor inlet are listed in Table 3.4.

Table 3.4: Geometric Parameters at the Compressor Face

Parameter	Measurement
Annulus Area, A_1	34.6 in ²
Tip Radius, r_{t1}	3.83 in
Hub Radius, r_{h1}	1.92 in
Pitchline radius, r_{m1}	2.89 in
Hub-to-Tip Radius, r_{h1}/r_{t1}	0.5

3.2 Compressor Exit Flow Parameters

The compressor team designed for a swirl-free exit to improve combustor efficiency. In addition, an important design choice is based on C_z remaining constant at the pitchline radius, which will be also remain constant along the blade span as well due to free vortex design. Since C_z is constant, the exit static temperature is calculated from the total enthalpy definition [7].

$$T_{exit} = T_{T_{exit}} - C_{exit}^2 / 2c_{p_{exit}} \quad \text{Eqn. 3.4}$$

Then, the exit static pressure and exit density are calculated from total pressure and the Perfect Gas Law. Lastly, the Mach number is determined from C_z and the speed of sound at the exit.

For geometric properties, the exit area is calculated with help from the continuity equation. Another driving design parameter is using a constant hub radius instead of constant tip or pitchline radius. From the constant hub radius and exit area, the exit tip radius is calculated [7]. Important geometric parameters at the compressor exit are listed in Table 3.5.

Table 3.5: Geometric Parameters at the Compressor Exit

<u>Parameter</u>	<u>Measurement</u>
Annulus Area, A_2	5.02 in ²
Tip Radius, r_{t2}	2.35 in
Hub Radius, r_{h2}	1.92 in
Pitchline radius, r_{m2}	2.14 in
Hub-to-Tip Radius, r_{h2}/r_{t2}	0.5

3.2.1 Shaft RPM

The SF-1600 engine compressor operates on a single spool. The single shaft's RPM is contingent on design the tip tangential Mach number and the tip radius [7]. The design team selected the $M_{T,tip}$ to be 1.3 to keep the relative tip Mach number supersonic. This results in the shaft RPM being 43,400 RPM.

3.3 Stage-by-Stage Analysis

For the compressor design, it is imperative that a stage-by-stage detailed analysis be conducted for three stream surfaces: hub, pitchline, and tip. This stage-by-stage analysis ensures the necessary

overall total temperature and pressure ratios are met without compressor stall, such as exceeding D-Factor limits. The overall compressor parameters are determined through this process.

3.3.1 **3-D Blade Design**

The design team decided to pursue free vortex design due to its simplicity. Industry has utilized a classical design tool in the past. Free vortex design follows the principle that the swirl profile resembles that of a vortex filament in other words. To establish the swirl profile, swirl is inversely proportional to the blade radius [7].

$$C_{\theta}r = Constant \qquad \qquad \qquad \text{Eqn. 3.5}$$

In addition, trade studies relating to inlet guide vanes (IGV) have been performed to see if any compressor stages could be eliminated as a result of higher stage loading. The use of IGV's to induce a pre-swirl before the first rotor did not significantly reduce the stage count [7]. Therefore, the team has agreed to not implement IGV's into the SF-1600 compressor design.

Lastly, solidity and aspect ratio are established based on projected trends from graphs taken from Wisler as displayed in Figure 3.1 and Figure 3.2 [18]. Solidity at the pitchline is initially set to 2.0, and aspect ratio is initially set to 1.5. It is important to note that the selected solidity adequately prevents exceeding D-Factor limits. After the first stage, the pitchline solidity is reduced to 1.5. The first stage solidity is 2.0 to help with start-up conditions involved with stall margin. Additional design parameters, such as stage degree of reaction, are used in stage design iterations to achieve an acceptable design.

Compressor Solidity Trend

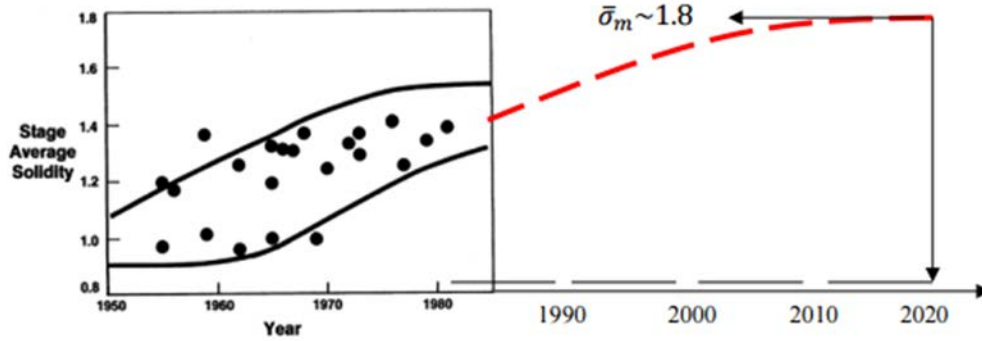


Figure 3.1: Solidity Trends from Wisler [20]

Compressor Aspect Ratio Trend

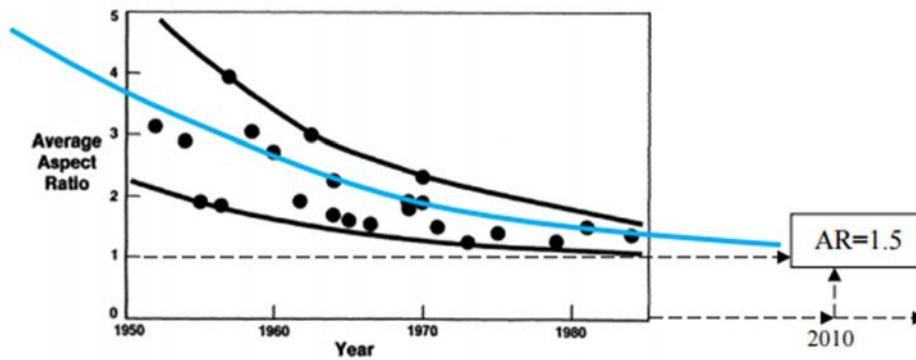


Figure 3.2: Aspect Ratio Trends from Wisler [20]

3.3.2 Stage Parameters

The stage-by-stage process follows the same procedure across each of the stages. Therefore, the aerodynamic analysis for the each stage is detailed accordingly in Figure 3.3 [2]. The velocity triangles at the hub, pitchline, and tip for the SF-1600 engine compressor are shown (to scale) in Figure 3.4, Figure 3.5, and Figure 3.6.

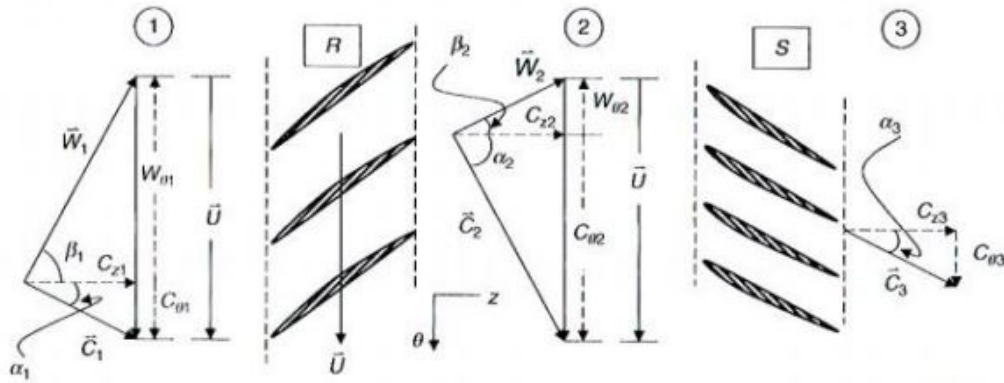


Figure 3.3: Example of Velocity Triangles for a Rotor and Stator [2]

Despite calculating the inlet and exit conditions for the SF-1600 compressor, it is imperative to perform the stage-by-stage analysis to ensure each stage operates within specified design limits, particularly relating to blade stall. As shown through the velocity triangles, the team implements the three stream surface design at the hub, pitchline, and tip. Therefore, the principles of blade vortex design are applied throughout the stage-by-stage design process. As stated previously, the team decided to implement the free vortex design to establish the swirl velocity profile in the spanwise direction downstream of the blade. With the swirl profile anchor at the pitchline, the flow parameters at the hub and tip can be determined. This design philosophy is used throughout the compressor to calculate the flow characteristics before and after both the rotor and the stator for each stage.

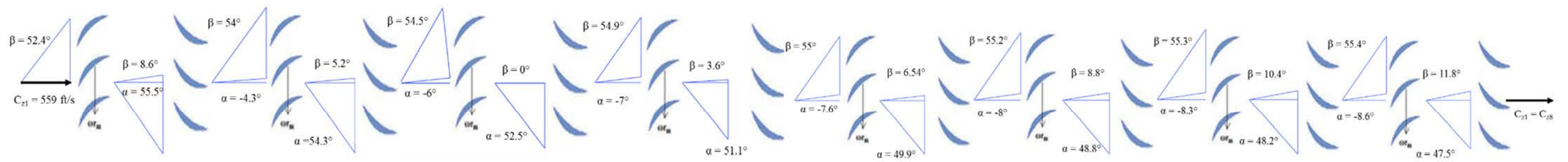


Figure 3.4: Compressor Velocity Triangles at the Hub

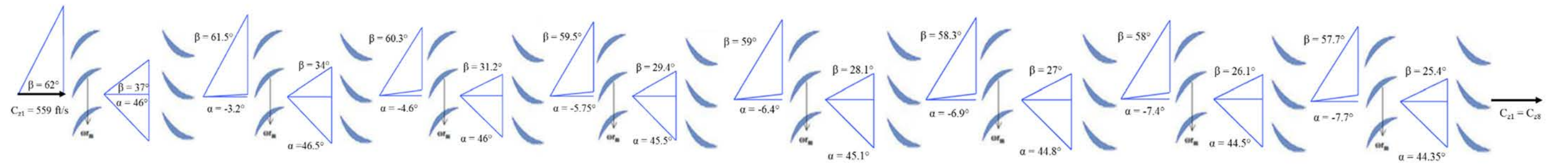


Figure 3.5: Compressor Velocity Triangles at the Pitchline

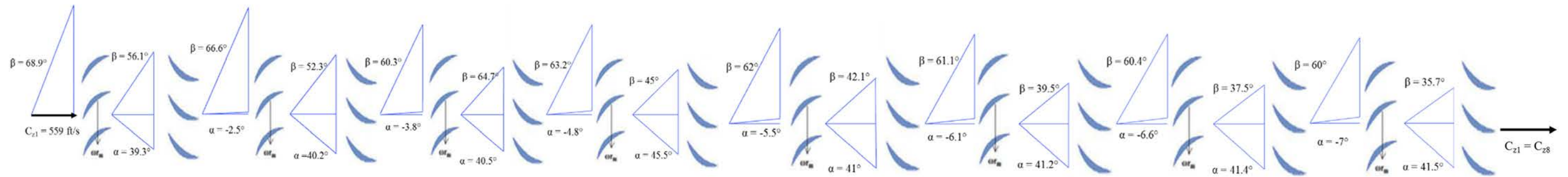


Figure 3.6: Compressor Velocity Triangles at the Tip

The stage-by-stage analysis begins with the first stage. Parameters from the inlet design with confirmation from GasTurb analysis results in P_{T1} , T_{T1} , M_{z1} , and \dot{m} are provided. Subsequently, the team selects the hub-to-tip radius ratio and the tip tangential Mach number for the first stage. The $M_{T,tip}$ results in the rotor speed, which determines the shaft rotational speed to be 43,400 RPM as shown in Equation 3.6 [7]. The selection of r_{h1}/r_{t1} allows for the determination of the first stage radii at the hub, pitchline, and tip and the compressor inlet flow area, A_1 .

$$U_x = \omega r_x \quad \text{Eqn. 3.6}$$

It is important to note that the hub-to-tip radius ratio changes across the axial span of the compressor due to the continual decrease in tip radius while the hub radius remains constant by design choice. Therefore, the area for later stages is calculated from the continuity equation. Using Perfect Gas Law, the density downstream, ρ_2 , determines the stage area, which in turns selects stage r_t while r_h remains constant. With help from Equation 3.6, the constant shaft RPM and stage radii calculates the stage rotor speed at the hub, pitchline, and tip [7].

From previously stated design assumptions, C_{z1} is calculated to be 559 ft/s, and α_1 is set to 0° due to zero pre-swirl from no implementation of IGV's. The team opted for a non-repeated stage design with inter-stage swirl for additional flow control throughout the compressor [7]. Therefore, the flow entering and leaving a given stage do not have the same flow angles α and β . It is important to note that the additional flow authority creates an additional bump in stage total temperature and pressure ratios, increasing the efficiency of each stage.

From free vortex design, the absolute swirl velocity, C_θ , is calculated for the three streamlines. This enables the determination of the absolute and relative velocities and the flow angles for each station within a given stage. To resolve the total temperature and pressure rise across the rotor for each stage, Euler's turbine equation calculates T_{12} and the total temperature

ratio in conjunction with the polytropic efficiency calculate P_2 . Equation 3.7 and Equation 3.8 outline this process [17]. Enthalpy, isentropic, and Perfect Gas relationships calculate T_2 , P_2 , and ρ_2 , respectively. Therefore, all flow parameters for each stage at the hub, pitchline, and tip can be determined from the aerodynamic characteristics and the velocity triangles.

$$T_{t2,m} = T_{t1} + \frac{U_m(C_{\theta 2} - C_{\theta 1})}{c_p} \quad \text{Eqn. 3.7}$$

$$\tau_c = \pi_c^{(\gamma-1)/\gamma e_c} \quad \text{Eqn. 3.8}$$

When determining parameters across the stator of a given, stage, it is important to note that the stator does not have a rotational velocity, so no work is performed across the row. The free vortex design produces a constant-work rotor, which establishes a uniform total temperature rise across the span [22]. Total pressure drops slightly across the stator due friction [7]. Therefore, P_T varies across the stator and the blade span. The flow characteristics after the stator of a given stage are equivalent to the flow characteristics entering the successive stage, further facilitating the stage-by-stage analysis.

Another important design choice involves the degree of reaction. As shown in Table 3.1, the degree of reaction can be between 0.1 and 0.9. To optimize the number of stages, the degree of reaction is selected to be 0.71 at the pitchline for the first stage. The degree of reaction must remain positive at the hub, pitchline, and tip for all stages. The degree of reaction is calculated using Equation 3.9 [7].

$$\circ R \cong 1 - \frac{C_{\theta 2} - C_{\theta 1}}{2U} \quad \text{Eqn. 3.9}$$

Two important parameters that ensure the success of the compressor design include D-Factor and De Haller criterion. These two parameters are calculated for the rotor and the stator at the three streamlines: hub, pitchline, and tip. The D-Factor must remain below 0.60 to prevent the blade from stalling. De Haller is supposed to remain above 0.72, but this criterion is less critical

than the D-Factor benchmark due to De Haller being exceedingly conservative [22]. In addition, there is a direct correlation between D-Factor and blade stall. The D-Factor and De Haller values for the first stage rotor and stator are included in Table 3.6. It is important to note that modern engines can have D-Factors of 0.62, so the D-Factor at the pitchline for the first rotor is acceptable.

$$D_r = 1 - \frac{W_2}{W_1} + \frac{|W_{\theta 2} - W_{\theta 1}|}{2\sigma_r W_1} \quad \text{Eqn. 3.10}$$

$$D_s = 1 - \frac{C_3}{C_2} + \frac{|C_{\theta 3} - C_{\theta 2}|}{2\sigma_s C_2} \quad \text{Eqn. 3.11}$$

$$DeHaller = \frac{W_2}{W_1} \quad \text{Eqn. 3.12}$$

Table 3.6: First Rotor and Stator De Haller and D-Factor Criteria

Parameter	First Rotor			First Stator		
	Hub	Pitchline	Tip	Hub	Pitchline	Tip
De Haller	0.616	0.572	0.644	1.682	1.670	1.404
D-Factor	0.531	0.564	0.489	0.592	0.520	0.472

3.3.3 Number of Stages

Before performing the stage-by-stage analysis, the number of stages for the axial compressor needed to obtain the necessary overall total pressure and temperature ratios can be initially calculated based on the Euler turbine equation. This process involves determining the temperature rise produced by design across one stage and comparing this value with the total temperature rise required by the cycle analysis. This is completed through the following process detailed below [7].

$$\Delta T_{t,stage} = T_{t2} - T_{t1} \quad \text{Eqn. 3.13}$$

$$\Delta T_{t,overall} = T_{exit} - T_{t1} \quad \text{Eqn. 3.14}$$

$$N_{stages} = \frac{\Delta T_{t,overall}}{\Delta T_{t,stage}} \quad \text{Eqn. 3.15}$$

The preliminary stage count calculated from the Euler turbine equation is confirmed through the stage-by-stage analysis process. The total pressure and temperature ratios across each stage are calculated. The overall total pressure and temperature ratios are determined from taking the product of all individual stage ratios. Using zero pre-swirl, the initial calculations result in a stage count of eight

stages, and the stage-by-stage analysis confirms its validity. The π_c and τ_c trends across the entire compressor are outlined in

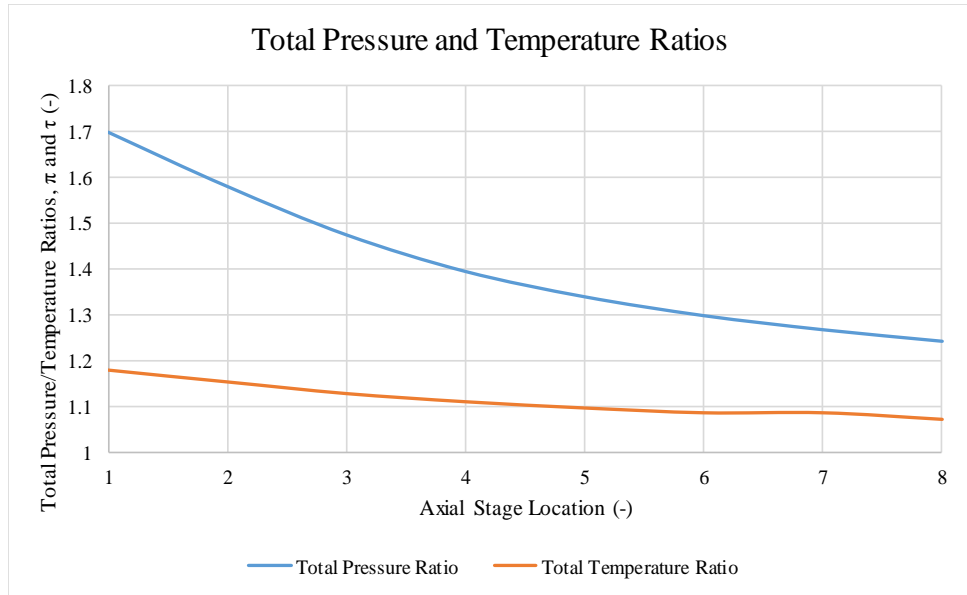


Figure 3.7.

Figure 3.7: Total Pressure and Temperature Ratios in Multi-Stage Compressor

Because eight stages reach the design compressor temperature and pressure ratios, the geometry of the compressor is acquired. The hub radius remains constant while the pitchline and tip radii

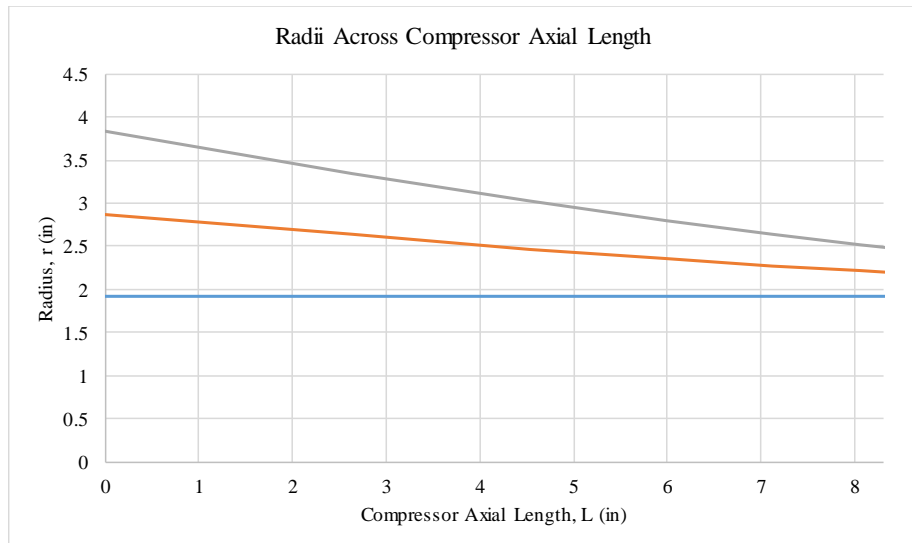


Figure 3.8: Compressor Geometry

decrease along the span. A side view of the geometry is graphically shown in Figure 3.6. A direct comparison between the inlet and exit geometry is outlined in Figure 3.9.

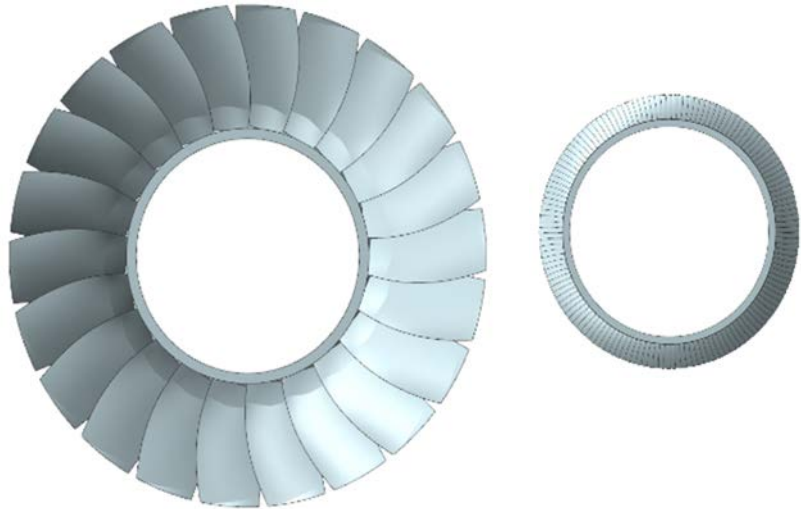


Figure 3.9: Compressor Inlet and Exit

From the stage-by-stage analysis, the hub, pitchline, and tip radii are calculated along the axial length of the compressor. It is assumed that the axial gap between blade rows is $0.25c_z$. From the calculated stagger angles, the overall compressor length is 9.19 in. The stages have an overall length of 8.37 in with a constant-area 0.82 in annulus placed between the compressor exit and the inlet to the combustor pre-diffuser to stabilize the flow.

3.3.4 Overall Compressor Parameters

After performing the stage-by-stage analysis, the optimization process begins. The different design choices have been selected to produce a π_c of 15.02 and a τ_c of 2.36. This results in an axial compressor with seven stages. The relevant parameters for the compressor design are listed in Table 3.7 for before and after both the rotor and the stator for the first stage. The compressor parameters for each stage at the pitchline are included in Table 3.8.

Table 3.7: Overall Compressor Parameters

Parameter	First Rotor			First Stator		
	Hub	Pitchline	Tip	Hub	Pitchline	Tip
U (ft/s)	727	1,090	1,450	0	0	0
r (in)	1.92	2.89	3.83	1.92	2.65	3.40
r_h/r_t	-	0.5	-	-	0.56	-
C_z (ft/s)	559	559	559	559	559	559
M_1	0.5	0.5	0.5	0.847	0.680	0.601
$M_{1,rel}$	0.820	1.096	1.394	0.486	0.589	0.835
M_2	0.847	0.680	0.601	0.460	0.459	0.459
$M_{2,rel}$	0.486	0.589	0.835	0.780	0.961	1.16
W_1 (ft/s)	917	1,230	1,560	565	701	1,000
W_2 (ft/s)	565	701	1,000	951	1,170	1,410
$C_{\theta 1}$ (ft/s)	0	0	0	812	585	457
$C_{\theta 2}$ (ft/s)	812	585	457	-42.3	-30.8	-24.2
C_2 (ft/s)	986	809	722	560	560	559
T_2 (°R)	644	644	644	644	644	644
P_{t2} (psi)	25.1	25.1	25.1	24.9	24.9	24.9
T_2 (°R)	563	590	601	618	618	618
P_2 (psi)	15.7	18.4	19.6	21.5	21.6	21.6
α_1 (deg)	0	0	0	55.5	46.3	39.3
α_2 (deg)	55.5	46.3	39.3	-4.33	-3.16	-2.48
β_1 (deg)	-52.5	-62.9	-69.0	8.65	-37.2	-56.2
β_2 (deg)	8.65	-37.2	-56.2	-54.0	-61.5	-66.6
γ (deg)	-46.7	-59.1	-67.3	14.4	-33.4	-54.4
°R	0.441	0.732	0.843	1.03	1.01	1.01
σ	3	2	1.35	2.7	1.8	1.35
De Haller	0.616	0.572	0.644	1.68	1.67	1.40
D-Factor	0.531	0.564	0.489	0.592	0.520	0.472
ϕ	0.769	0.554	0.433	0.769	0.560	0.440
ψ	1.117	0.611	0.427	-	-	-
AR	1.5	1.5	1.5	1.5	1.5	1.5
λ	0.5	0.5	0.5	0.5	0.5	0.5
i (deg)	5.73	3.72	1.72	5.73	3.72	1.72
c (in)	-	1.28	-	-	0.99	-
c_z (in)	-	0.88	-	-	0.83	-
s (in)	-	0.62	-	-	0.28	-
N_{blades}	-	2	-	-	59	-

Table 3.8: Overall Compressor Parameters at Pitchline for Each Stage

	1 st Rotor	1 st Stator	2 nd Rotor	2 nd Stator	3 rd Rotor	3 rd Stator	4 th Rotor	4 th Stator	5 th Rotor	5 th Stator	6 th Rotor	6 th Stator	7 th Rotor	7 th Stator	8 th Rotor	8 th Stator
Parameter	Pitchline	Pitchline														
U (ft/s)	1,100	0	998	0	936	0	893	0	863	0	840	0	823	0	810	0
r (in)	2.89	2.54	2.63	2.53	2.46	2.42	2.35	2.33	2.27	2.26	2.22	2.21	2.17	2.17	2.14	2.09
r _h /r _t	0.50	0.56	0.57	0.61	0.63	0.65	0.68	0.69	0.73	0.73	0.76	0.76	0.79	0.78	0.81	0.81
C _z (ft/s)	559	559	559	559	559	559	559	559	559	559	559	559	559	559	559	559
M ₁	0.50	0.68	0.46	0.63	0.43	0.59	0.40	0.55	0.38	0.52	0.36	0.49	0.35	0.47	0.34	0.46
M _{1,rel}	1.10	0.59	0.96	0.52	0.86	0.48	0.79	0.44	0.73	0.42	0.69	0.39	0.66	0.38	0.63	0.36
M ₂	0.68	0.96	0.63	0.43	0.59	0.40	0.55	0.38	0.52	0.36	0.49	0.35	0.47	0.34	0.46	0.32
M _{2,rel}	0.59	0.96	0.52	0.86	0.48	0.79	0.44	0.73	0.42	0.69	0.39	0.66	0.38	0.63	0.36	0.56
W ₁ (ft/s)	1,230	701	1,170	672	1,130	654	1,100	641	1,080	633	1,070	627	1,060	622	1,050	619
W ₂ (ft/s)	701	1,170	672	1,130	654	1,100	641	1,080	633	1,070	627	1,060	622	1,050	619	975
C _{θ1} (ft/s)	0	585	-30.8	588	-45.4	577	-56.3	569	-62.5	561	-67.9	555	-72.3	550	-75.6	546
C _{θ2} (ft/s)	585	-30.8	588	-45.4	577	-56.3	569	-62.5	561	-67.9	555	-72.3	550	-75.6	546	0
C ₁ (ft/s)	559	809	560	811	561	803	562	798	562	792	563	787	564	784	564	782
C ₂ (ft/s)	809	560	811	561	803	562	798	562	792	563	787	564	784	564	782	559
C _{2,tip} (ft/s)	809	559	811	560	735	561	739	561	741	562	743	563	745	563	746	559
T _{t2} (°R)	644	644	743	743	838	838	930	930	1,020	1,020	1,110	1,110	1,190	1,190	1,280	1,280
P _{t2} (psi)	25.1	24.9	39.5	39.3	57.9	57.9	81.0	80.8	109	108	141	140	178	178	192	206
T ₂ (°R)	590	618	689	717	785	812	877	904	967	993	1,050	1,080	1,140	1,170	1,230	1,250
P ₂ (psi)	18.4	21.6	30.2	34.7	46.0	51.9	66.0	73.1	90.3	98.7	119	129	153	164	192	206
α ₁ (deg)	0	46.3	-3.16	46.5	-4.64	45.9	-5.75	45.5	-6.39	45.1	-6.92	44.8	-7.37	44.6	-7.71	44.4
α ₂ (deg)	46.3	-3.16	46.5	-4.64	45.9	-5.75	45.5	-6.39	45.1	-6.92	44.8	-7.37	44.6	-7.71	44.4	0
β ₁ (deg)	-62.9	-37.2	-61.5	-33.7	-60.3	-31.3	-59.5	-29.4	-58.9	-28.1	-58.4	-27.0	-58.0	-26.1	-57.7	-25.4
β ₂ (deg)	-37.2	-61.5	-33.7	-60.3	-31.3	-59.5	-29.4	-58.9	-28.1	-58.4	-27.0	-58.0	-26.1	-57.7	-25.4	-55.0
γ (deg)	-59.1	-33.4	-48.3	-30.0	-48.8	-27.8	-49.2	-25.7	-49.4	-24.4	-49.5	-23.3	-49.6	-22.4	-49.7	-21.7
°R	0.732	1.01	0.690	1.04	0.667	1.05	0.650	1.07	0.493	1.08	0.630	1.08	0.622	1.09	0.616	1.05
σ	2	1.8	1.5	1.8	1.5	1.8	1.5	1.8	1.5	1.8	1.5	1.8	1.5	1.8	1.5	1.8
De Haller	0.572	1.670	0.574	1.681	0.579	1.726	0.582	1.685	0.586	1.683	0.588	1.683	0.590	1.682	0.591	1.576
D-Factor	0.564	0.520	0.63	0.526	0.610	0.520	0.609	0.515	0.607	0.510	0.607	0.505	0.607	0.547	0.607	0.479
φ	0.554	0.433	0.581	0.597	0.609	0.626	0.632	0.645	0.650	0.665	0.666	0.679	0.678	0.690	0.689	0.700
ψ	0.611	-	0.657	-	0.685	-	0.710	-	0.727	-	0.742	-	0.755	-	0.766	-
AR	1.5	1.5	1.5	1.5	1.5	1.5	1.5	1.5	1.5	1.5	1.5	1.5	1.5	1.5	1.5	1.5
λ	0.5	0.5	0.5	0.5	0.5	0.5	0.5	0.5	0.5	0.5	0.5	0.5	0.5	0.5	0.5	0.5
i (deg)	3.72	3.72	3.72	3.72	3.72	3.72	3.72	3.72	3.72	3.72	3.72	3.72	3.72	3.72	3.72	3.72
c (in)	1.28	0.99	0.95	0.82	0.73	0.67	0.58	0.55	0.48	0.46	0.40	0.39	0.34	0.34	0.29	0.30
c _z (in)	0.88	0.83	0.63	0.71	0.48	0.59	0.38	0.50	0.31	0.42	0.26	0.36	0.22	0.32	0.19	0.28
s (in)	0.62	0.28	0.61	0.29	0.48	0.23	0.38	0.19	0.32	0.16	0.26	0.13	0.22	0.11	0.19	0.10
N _{blades}	29	59	27	55	32	65	39	79	45	91	53	107	61	123	70	141

3.4 Blade Structural Analysis

The blade structural analysis is performed to select the material for the rotor and stator blades for each stage. To start the process, the maximum temperature of the compressor is calculated, and an initial material selection is made based on this parameter. The maximum temperature in the compressor is 1,290 °R, which translates to 830 °F. A titanium alloy is selected from the Mattingly, Heiser, and Pratt creep rupture strength diagram [16]. Therefore, the titanium alloy of Ti-5Al-2.5Sn is an adequate initial selection due to the material melting point of 2,890 °F [18]. In addition, the Ti-5A-2.5Sn should be able to withstand the stress concentrations the compressor blades experience.

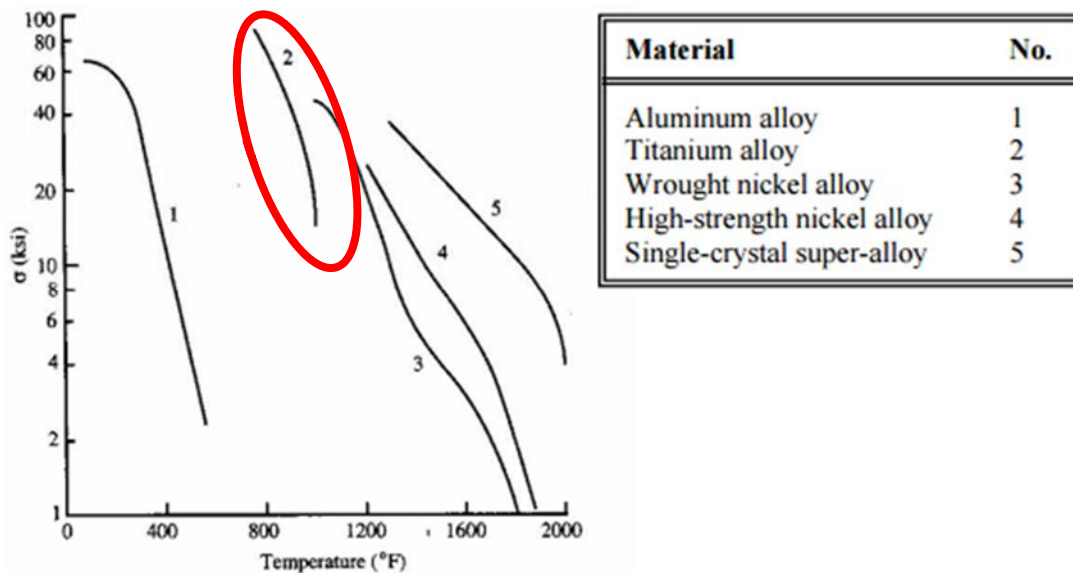


Figure 3.10: Creep Rupture Strength Diagram [16]

After the initial material selection, the stresses associated with the compressor are observed. The compressor blades experience multiple types of stress loadings, but centrifugal stress is considered the critical stress for blade design. Therefore, centrifugal stress is the driving design factor. To calculate the centrifugal stress, the taper ratio and blade density are selected as design choices. The shaft RPM and flow area are necessary as well. The flow area and the centrifugal stress are calculated from the following equations [19].

$$A = 2\pi r_{m1}(r_{t1} - r_{h1}) \quad \text{Eqn. 3.16}$$

$$\sigma_c = \rho_{blade} \frac{\omega^2 A}{4\pi} (1 + A_t/A_h) \quad \text{Eqn. 3.17}$$

With a blade density of 0.162 lb_m/in³ and a taper ratio of 0.5, the centrifugal stress is 53,800 psi, and this includes an additional factor of safety of 1.5. The allowable stress for the titanium alloy is 120,000 [18]. This results in a positive margin of safety of 1.23. This means that the Ti-5A-2.5Sn material is adequate to withstand the stresses the rotor and stator blades experience. Table 3.9 outlines the important parameters involved in the centrifugal stress calculations.

Table 3.9: Centrifugal Stress Parameters

Parameter	Value
Allowable Centrifugal Stress, σ_{all}	120,000 psi
Blade Density, ρ_{blade}	0.162 lb _m /in ³
Taper Ratio, A_t/A_h	0.5
Flow Area, A	34.6 in ²
Shaft Speed, ω	43,400 RPM
Design Centrifugal Stress, σ_c	53,800 psi
Margin of Safety, MS	1.23

The SF-1600 engine implements integrally bladed rings (“blings”) into the compressor design. From Equation 3.25, the bladed ring thickness is 0.125 in. Material properties provide ultimate bending stress values. The thickness is solved through an iterative method to calculate the ring radius. The allowable stress for the titanium alloy is 120,000 psi, and the stress exerted on the ring is determined to be 94,200 lbf, which includes a factor of safety of 1.5. This results in a positive margin of safety of 0.274. Table 3.10 outlines the important parameters involved in the ring stress calculations.

$$\sigma_{ring} = \frac{m_{blade} r_{blade} \omega^2 + m_{ring} r_{ring} \omega^2}{2 \sin \theta A} \quad \text{Eqn. 3.18}$$

Table 3.10: Calculating Ring Thickness and Stress

Parameter	Value
Allowable Centrifugal Stress, σ_{all}	120,000 psi
Blade Density, ρ_{blade}	0.162 lb _m /in ³
m_{blade}	0.00929 lb _m
r_{blade}	2.99 in
m_{ring}	0.0132 lb _m
r_{ring}	1.79 in
t	0.125 in
A_{ring}	0.154 in ²
Shaft Speed, ω	43,400 RPM
Design Centrifugal Ring Stress, σ_{ring}	94,200 psi
Margin of Safety, MS	0.274

3.5 Compressor Rotor and Stator Blade Design

The Mach number varies from hub-to-tip of the compressor blade. The flow is transonic at the hub and the pitchline and supersonic at the tip. A controlled diffusion airfoil (CDA) is best for the hub and pitchline region while a double circular arc (DCA) is best for the tip region. [7]. The thickness to chord ratio tapers linearly up the blade. Being 10% at the hub and 3% at the tip. The figure below shows the two types of blade profiles.

Using the thickness over chord ratio the incidence angle was approximated for each section. With the incidence angle known more geometric parameters can be calculated. These parameters are the deviation angle (δ^*), the leading-edge angle (κ_1), and trailing-edge angle (κ_2). These are calculated by using the cascade geometric equations below.



Figure 3.11: Blade Cross-Sections

$$\delta^* = \frac{\Delta\beta}{4\sqrt{\sigma}} \quad \text{Eqn. 3.19}$$

$$\kappa_1 = \beta_1 - i \quad \text{Eqn. 3.20}$$

$$\kappa_2 = \beta_2 - \delta^*$$

Eqn. 3.21

Table 3.11: Blade Design Parameters for the First Stage

	i	κ_1	κ_2	δ^*	Units
Hub	5.73	-58.18	-1.53	10.18	Degrees
Pitchline	3.72	-66.59	-42.41	5.24	Degrees
Tip	1.72	-70.69	-59.17	3.02	Degrees

3.6 Stall Margin

Stall margin is a very important when designing a compressor. Koch developed a method to estimate the maximum pressure rise and stall margin per stage in an axial-flow compressor by relating it to a two-dimensional diffuser. Two main parameters are calculated to find the stall margin, the stalling effective static-pressure rise coefficient $(C_h)_{ef}$ and the average diffusion length ratio of the stage L/g_2 . The parameters or calculated by the two equations below.

$$(C_h)_{ef} = (C_h)_{adj} \left[\frac{(v_1^2)_{rotor} + (v_1^2)_{stator}}{(v_1^2)_{rotor} + F_{ef}(v_1^2)_{stator}} \right] \quad \text{Eqn. 3.22}$$

$$\left(\frac{L}{g_2} \right)_{stage} = \left[\frac{(L/g_2)_{rotor} * q_1' + (L/g_2)_{stator} * q_1}{q_1' + q_1} \right] \quad \text{Eqn. 3.23}$$

Figure 3.12 displays the geometric parameters of the compressor blades used to calculate L/g_2 . The rest of the values can be taken from the velocity triangle data obtained from free vortex design. These values are shown above in Section 3.3.2. The stalling effective static-pressure rise coefficient was calculated to be 0.476 and the average diffusion length ratio of the stage was calculated to be 2.06. The red dot on Figure 3.11 represents the calculated value. The stall margin is between 10 and 15 percent.

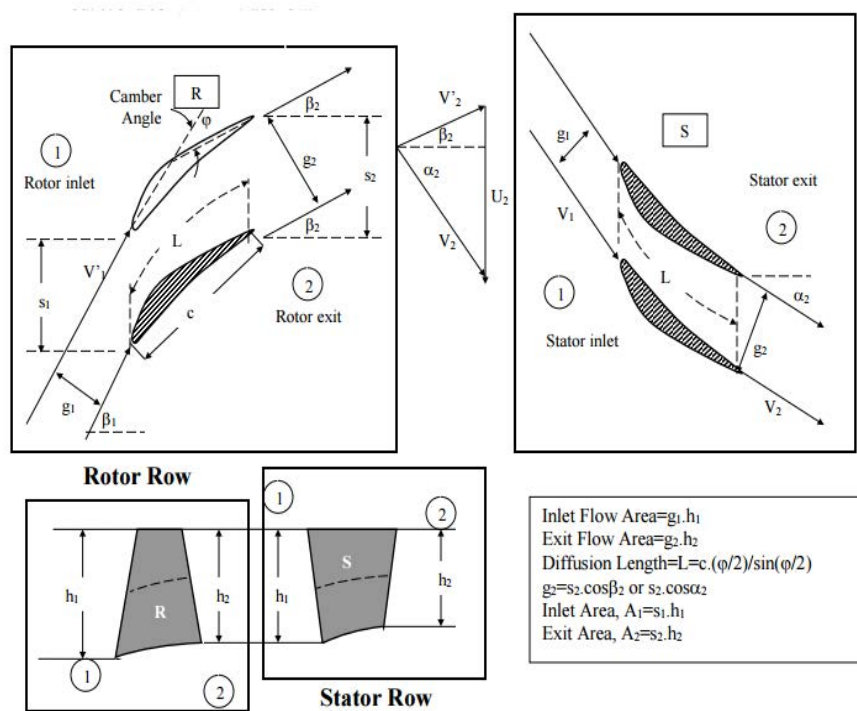


Figure 3.12: Geometric Parameters of Compressor Blades [7]

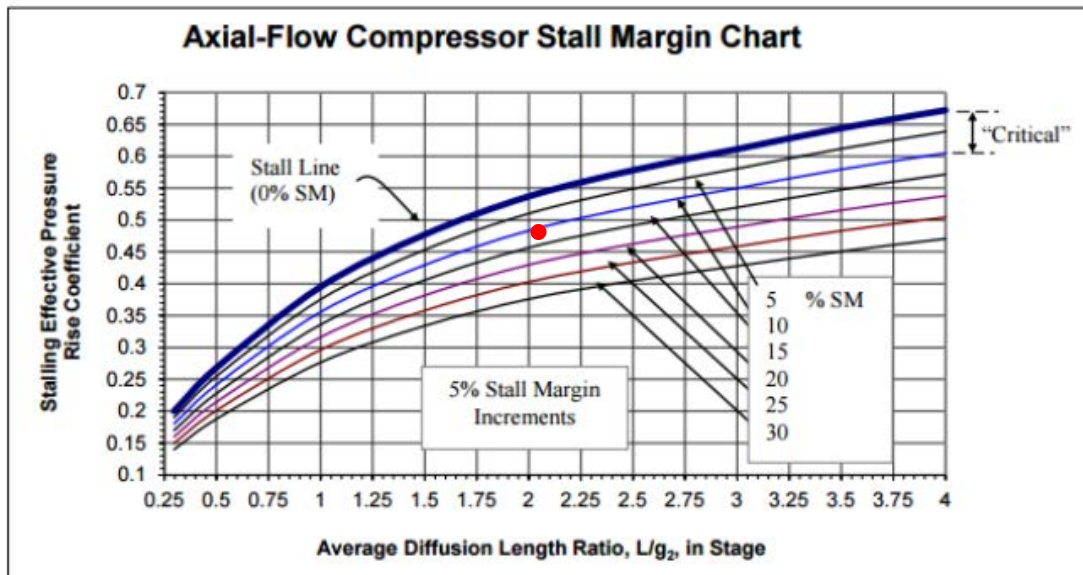


Figure 3.13: Stall Margin Chart [22]

3.7 Advanced Technologies

The SF-1600 engine compressor includes two advanced technologies: integrally bladed rings and variable stators. Blings act as a replacement for the shaft, causing a reduction in part count and

weight. In addition, blings increase reliability, maintainability, and performance of the compressor [65]. The design team implemented variable stators on the first three stages. The variable stators rotate based on fuel (throttle) setting and RPM to help with engine start-up

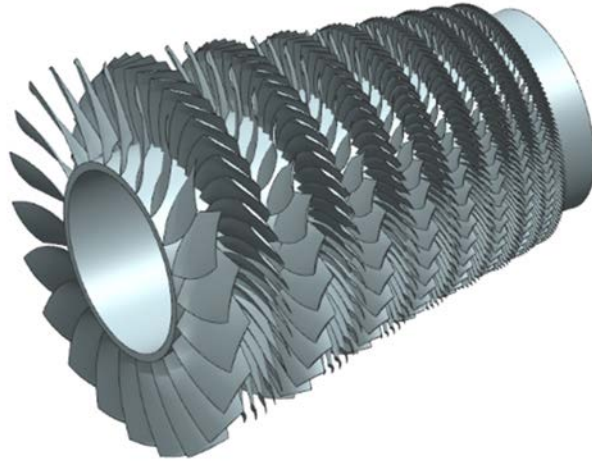


Figure 3.14: Integrally Bladed Rotor Design Implementation

and shutdown conditions. Therefore, the slope of the surge/stall line is reduced [7].

3.8 Compressor Flow Station Data

Table 3.8 summarizes the important compressor design parameters.

Table 3.12: Compressor Design Data

Flow Station Data: Compressor	
Inflow (lb/s)	8.66
Corrected Inflow (lb/s)	8.97
Inflow Total Pressure (psi)	14.5
Inflow Total Temperature (°R)	545.7
Inflow Fuel-air-Ratio	0
Inflow Mach #	0.5
Inflow Area (in ²)	34.6
Pressure Ratio	15

4.0 Combustion System

The following section presents the design and analysis of the combustion system for the SF-1600 engine. The SF-1600 will employ an annular combustor with a straight throughflow burner. The baseline engine, from the RFP, also uses an annular configuration, but it uses a reverse flow combustor. Figure 4.1 shows the major features and flow patterns of an annular combustor that has the same general configuration as the design.

From the optimized cycle analysis, the combustor needs to be design for: a T_{T4} of 2560°R, a P_{T4} of 207.3 psia, the ability to burn JP-8 (Jet A) fuel, high burner efficiency, and low-emissions. The following subsections detail the geometric design of the combustor components and properties.

4.1 Pre-Diffuser Design

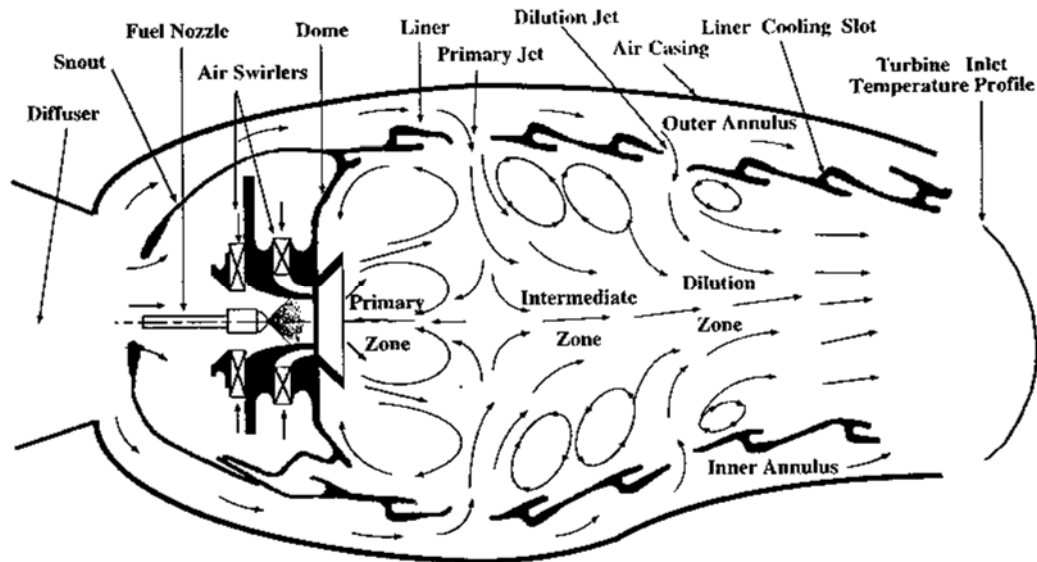


Figure 4.1: Typical Annular Combustor with Straight through Flow Burner [7]

The flow exiting the compressor has a Mach number of 0.31. For proper combustion, the Mach number needs to be decelerated to approximately Mach 0.1. A flat-walled diffuser with two splitter vanes will be used in the design. The splitter vanes were added to reduce the length of the diffuser; this effect is shown in Figure 4.2. Splitter vanes prevent diffuser stall and make the velocity profile of the flow more uniform [25]. A flat-walled configuration was chosen to reduce total pressure loss, when compared to other diffuser configurations, such as a dump diffuser [16].

4.2 Flow Partitioning in Combustor

The airflow that exits the pre-diffuser is partitioned into four flows, the primary zone, secondary zone, dilution zone, and cooling airflows, as

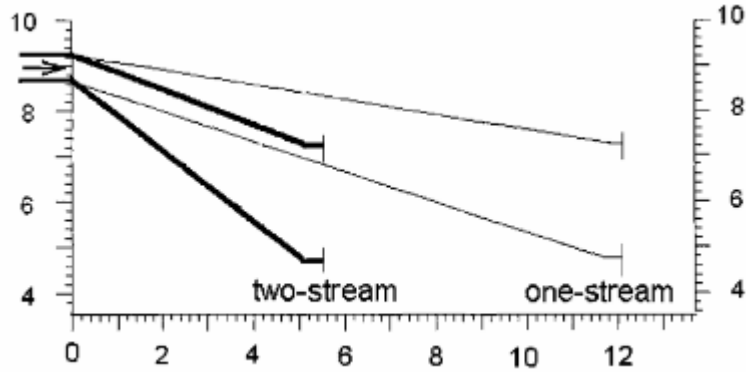


Figure 4.2: Effect of Splitter Vane on Diffuser Length [16]

enters the combustor. Table 4.1 shows the parameters in our combustor design. In this report, we outline the methodology that was used to yield these design parameters. In particular, the design methodology of Mattingly, Heiser and Pratt is implemented in our design.

Table 4.1: Flow Partitioning and Equivalence Ratios

ϕ_{PZ}	ϕ_{SZ}	\dot{m}_{PZ} (lb/s)	\dot{m}_{SZ} (lb/s)	\dot{m}_{cool} (lb/s)	\dot{m}_{DZ} (lb/s)	\dot{m}_{fuel} (lb/s)	\dot{m}_{total} (lb/s)	Φ
0.652	0.457	3.76	1.61	0.185	2.51	0.168	8.22	0.281

We start our design with the Bragg criterion that states that the maximum combustor efficiency occurs near the lean blowout condition, which corresponds to a primary zone equivalence ratio of 0.55. Operational combustors should stay safely above the blowout condition, to avoid damage to the engine [16].

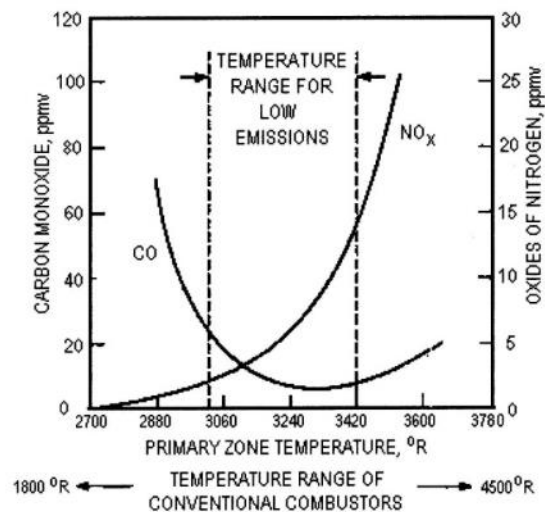


Figure 4.3: CO and NOx Emissions as a Function of Primary Zone Temperature [16]

Figure 4.3 shows that a primary zone temperature around 3200 °R is desirable to help reduce CO and NO_x emissions. CO and NO_x are both regulated by the Environmental Protection Agency and thus must be kept at levels deemed acceptable by the EPA. Our team decided to embrace/adopt low-emission design principles, even in this military aircraft engine.

The second step is to address liner cooling. The cooling effectiveness parameter is a function of the hot gas temperature of the combustor, the compressor discharge temperature, and the desired wall temperature, which is a function of material properties. This parameter will determine the amount of cooling airflow needed to keep the combustor liner at the desired temperature.

$$\Phi = \frac{T_g - T_w}{T_g - T_c} \quad \text{Eqn. 4.1}$$

Using the cooling effectiveness parameter and Figure 4.3, the amount of cooling airflow was determined. The design team chose to use a convection/film cooled liner for the design. While not as effective as transpiration cooling, convection/film cooling will require only slightly more

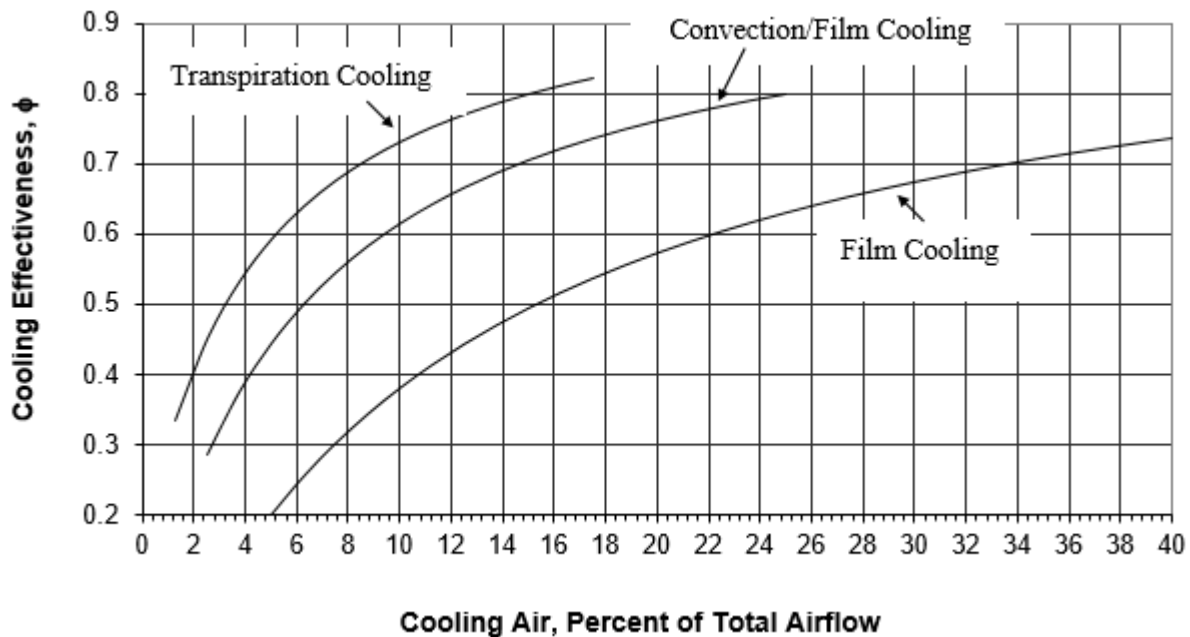


Figure 4.4: Cooling Effectiveness, Methods, and Cooling Air [7]

cooling air for this design. Figure 4.4 shows how cooling methods affect the amount of cooling air needed for the combustor liner. Transpiration cooling may also face problems with the pores clogging [7]. This issue would cause the liner to be considered a Life-Limited Part, meaning it would require more frequent inspection and replacement [28].

4.3 Combustor Geometric Parameters and Sizing

The length of each combustor component is shown in Table 4.2. Methods from Aircraft Engine Design by Mattingly, Heiser, and Pratt were used to calculate the lengths in Table 4.2. The total combustor length was found to be 6.71 inches, over 3 inches shorter than the combustor in the baseline engine.

Table 4.2: Combustor Zone Lengths

L_{pz} (in.)	L_{sz} (in.)	L_{dz} (in.)	L_{diffuser} (in.)	L_{total} (in.)
0.939	2.28	1.96	1.53	6.71

4.4 Combustor Efficiency

To accomplish our goal, we used the Lefebvre combustor loading parameter (CLP). Methods from Aircraft Propulsion by Farokhi were used to calculate the CLP and efficiency of the combustor.

$$CLP = \theta = \frac{p^{1.75} A_R h e^{t/b}}{w_a} \quad \text{Eqn. 4.2}$$

$$b = 382(\sqrt{2} \pm \ln \frac{\phi}{1.03}) \quad [(+) \text{ for } \phi < 1.03, (-) \text{ for } \phi > 1.03] \quad \text{Eqn. 4.3}$$

The reaction rate parameter, b, is a function of the primary zone equivalence ratio [7]. The efficiency of the combustor was estimated using the relationships shown in Figure 4.5. Under the cruise condition, it can be seen from values in Table 4.3 and Figure 4.5 that the combustor will be operating at an efficiency of nearly 100%. To satisfy the EPA regulations, a combustor must have a combustion efficiency of at least 99% [7].

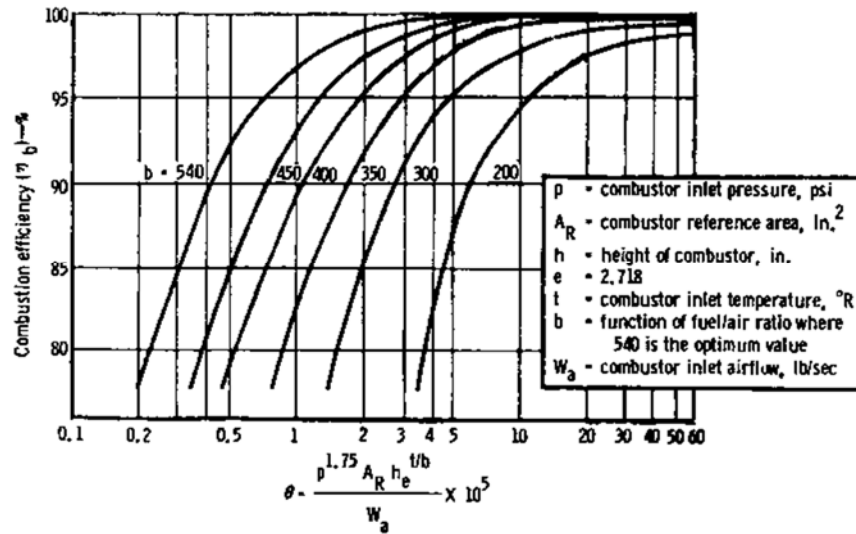


Figure 4.5: Lefebvre Parameter and Combustion Efficiency Correlation [7]

Table 4.3: Combustion Efficiency at Cruise

ϕ_{PZ}	CLP	b	Combustion Efficiency
0.652	16.4×10^5	366	>99%

4.5 Temperature Profile

The temperature profile at the combustor exit exhibits non-uniformity. This non-uniformity can be described using Equations 4.4 and 4.5. Equation 4.4 is used to calculate the pattern factor. Based on the methodology of Farokhi, a pattern factor of 0.15 was selected. This yielded a T_{t-max} of 2751 °R. T_{t-max} is the maximum exit temperature the turbine nozzle would be subjected to.

$$PF = \frac{T_{t-max} - T_{t-avg}}{T_{t-avg} - T_{t-in}} \quad \text{Eqn. 4.4}$$

$$P_f = \frac{T_{t-max-avg} - T_{t-in}}{T_{t-avg} - T_{t-in}} \quad \text{Eqn. 4.5}$$

A profile factor of 1.04 was selected using the methods of Farokhi. Using Equation 4.5, $T_{t-max-avg}$ was found as 2610 °R. $T_{t-max-avg}$ is the circumferential average of the maximum temperature. The turbine rotor will see this temperature profile.

4.6 Material Selection

The combustor liner will experience temperatures above 3200 °R. Materials traditionally used as liner materials, such as superalloys, would require a significant amount of cooling air to

withstand that temperature. The SF-1600 will utilize a liner made of ceramic matrix composites, CMC. According to Benzakein, CMC's are able to withstand temperatures of nearly 2800 °R, which significantly decreases the amount of cooling air needed for the liner. The CMC liner will also be lighter weight than the baseline engine [23]. CMC liners are currently being used on the CRM International LEAP engine and GE will be using CMC parts in the GE9X engine, which is scheduled to be produced in 2019 [24].

Silicon carbide composite CMC's exhibit high strength, high stiffness, and are oxidatively stable at temperatures that are much higher than what could be tolerated by unprotected alloys. CMC's are also able to tolerate minor flaws [25].

4.7 **Fuel Injection**

Selection and design of the fuel injector is critical to a high-efficiency combustor design. General Electric's lean burning Twin Annular Premixing Swirler (TAPS) will be used on the SF-1600. Each TAPS injector contains a central pilot, surrounded by the main injector. For low power operation, only the pilot is fueled. At high power the main receives the majority of the fuel [23]. The SF-1600 will use 12 fuel injection nozzles, a reduction from the 14 used on the baseline.

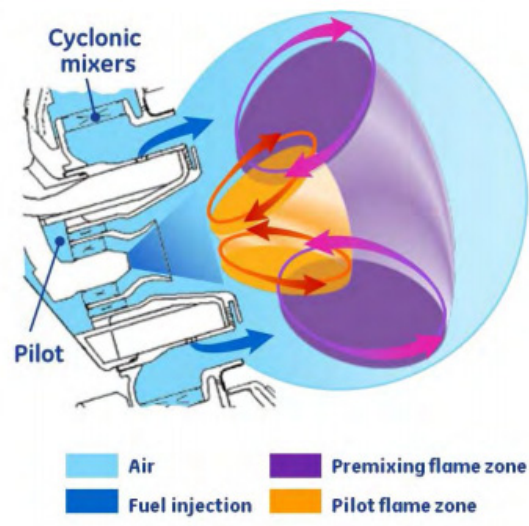


Figure 4.6: TAPS Fuel Injector [26]

GE has begun mass production of 3D-printed fuel nozzles. Using this new manufacturing technology on the SF-1600 nozzles allows them to be printed as a single piece, which helps reduce

the part count, and these nozzles are also five times more durable than traditionally made nozzles [27].

4.8 Ignition Source

Surface discharge igniters will be used on the SF-1600. This type of igniter was chosen due to its superior performance over other forms of ignition. It is also the most commonly used ignition source for aircraft engines [25]. The SF-1600 will use two igniters, located on opposite sides of the annulus.

4.9 Emissions

Combustor design teams need to address the critical question of combustor emissions. Both NO and NO₂, referred to as NO_x, are pollutants generated by combustion. Equation 4.4 was used to find the NO_x Severity Parameter, S_{NOx}. The ‘war’ term in Equation 4.4, is the water-air-ratio. The SF-1600 does not utilize a water injection system, so the ‘war’ term is always zero. Equation 4.5 was used to find the NO_x Emission Index. Equations 4.4 and 4.5 are found in the GasTurb manual [15].

$$S_{NOx} = \left(\frac{P_3}{2965 \text{ kPa}} \right)^4 * e^{\left(\frac{T_3 - 826 \text{ K}}{194 \text{ K}} + \frac{6.29 - 100 * war}{53.2} \right)} \quad \text{Eqn. 4.4}$$

$$EI = .032 * S_{NOx} \quad \text{Eqn. 4.5}$$

Table 4.4: Comparison of NO_x Emissions

	SF-1600	Baseline
S _{NOx} (~)	0.419	0.206
EI (lbm/lbm of fuel)	0.0134	0.00658

Table 4.4 shows that the SF-1600 will produce more NO_x emissions than the baseline engine per pound of fuel. However, because the SF-1600 has a lower fuel mass flow rate than the baseline, some of the additional NO_x production will be offset. The increased pressures and temperatures from the baseline had enough benefits in other aspects of the design to outweigh the increased NO_x emissions.

The TAPS fuel injectors will play a key role in reducing emissions. The TAPS combustor, used in the LEAP engine, significantly reduces NO_x, CO, unburned hydrocarbons, and smoke, when compared to the engine it replaced. This technology has also been shown to outperform double annular combustors in reducing emissions [23].

4.10 Three-View of the Combustor

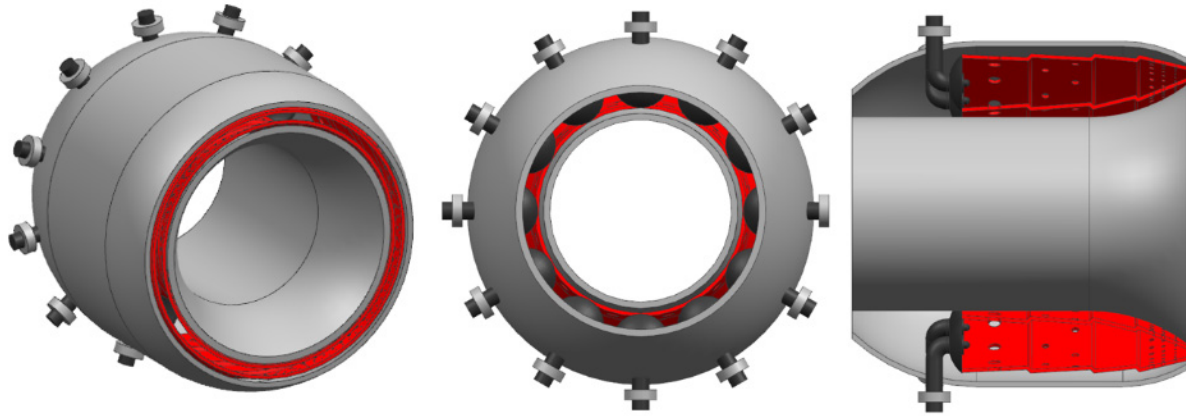


Figure 4.7: Isometric, Side, and Front View of the Combustor

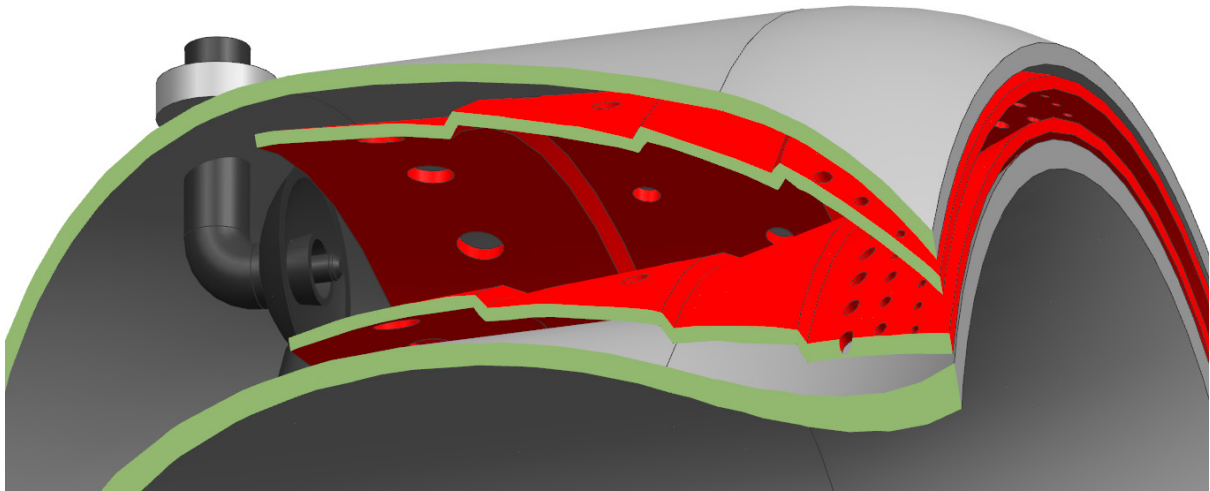


Figure 4.8: Combustor Cutaway

4.11 Burner Flow Parameters

Table 4.5: Burner Flow Data

Flow Station Data: Burner	
Inflow (lb/s)	8.05
Corrected Inflow (lb/s)	0.846
Inflow Total Pressure (psi)	207.3
Inflow Total Temperature (°R)	1242
Inflow Fuel-air-Ratio	0
Inflow Mach #	0.31
Inflow Area (in ²)	4.92
Pressure Ratio	0.95

5.0 Axial-Flow Turbine Design

The SF-1600 gas turbine engine is composed of a single spool high-pressure turbine (HPT) which powers the compressor in gas generator (GG), and a single spool low pressure turbine (LPT) which powers the propeller. The spools are counter rotating to minimize the net moment induced on the aircraft from the engine. Multiple designs were analyzed and the team chose to use a two-stage gas generator and a two stage free turbine. This section outlines the design selections in both the HPT and LPT and the rationale for their selections.

5.1 Pitchline Design Parameters

The first design selection uses a constant axial velocity for both spools. The temperature, pressure, and mass flow rate at the inlet to the HPT are obtained from the GasTurb analysis. The angular speed for the HPT has been set by the requirements of the compressor while the angular speed for the LPT and

Table 5.1. Pitchline Inlet Design Parameters

Inlet Design Parameter at Pitchline	Value
\dot{m}_1 (lbm/s)	8.22
T_{t1} (R)	2560
P_{t1} (psi)	207
M_2 (~)	1.1
α_1 (deg)	0
α_2 (deg)	70
ω_{HPT} (rpm)	43446
ω_{LPT} (rpm)	34000
$C_{\theta,LPT\ Exit}$ (ft/s)	~0

the other parameters shown in Table 5.1 are chosen to optimize LPT-gearbox-propeller

system efficiency. In accordance with the design parameters set by Farokhi [7], the first nozzle throat of each spool is choked, therefore M_2 is designed at Mach 1.1. Mattingly [16] claims that the best performance is obtained when $60^\circ < \alpha_2 < 75^\circ$, thus the pitchline nozzle exit angle is set to $\alpha_2 = 70^\circ$. The angular velocity of the LPT is chosen at 34000 rpm, which is much lower than the HPT. The design selection produces a smaller gear reduction for the propeller. Furthermore, the LPT is designed to have minimum exit swirl. The kinetic energy tied up in the turbine exit swirl is deemed as a loss in turbine efficiency, which is also of no use in the exhaust nozzle.

5.2 Turbine Flow Calculations and Aerothermodynamics

The flow calculations for the HPT and LPT are performed using a stage analysis as shown in Ref. 1 and 2. Figure 5.1 shows an example of the velocity triangles used in the analysis. The inlet design parameters are used to begin the calculations. The nozzle angles and rotor relative exit Mach numbers are the principal design choices that influence the rest of the calculations. Table 5.2 and Table 5.3 show the critical flow parameters of the three-stream analysis for the HPT and LPT respectively. Since the HPT and LPT are counter rotating, the positive θ axis is reversed for the LPT calculations.

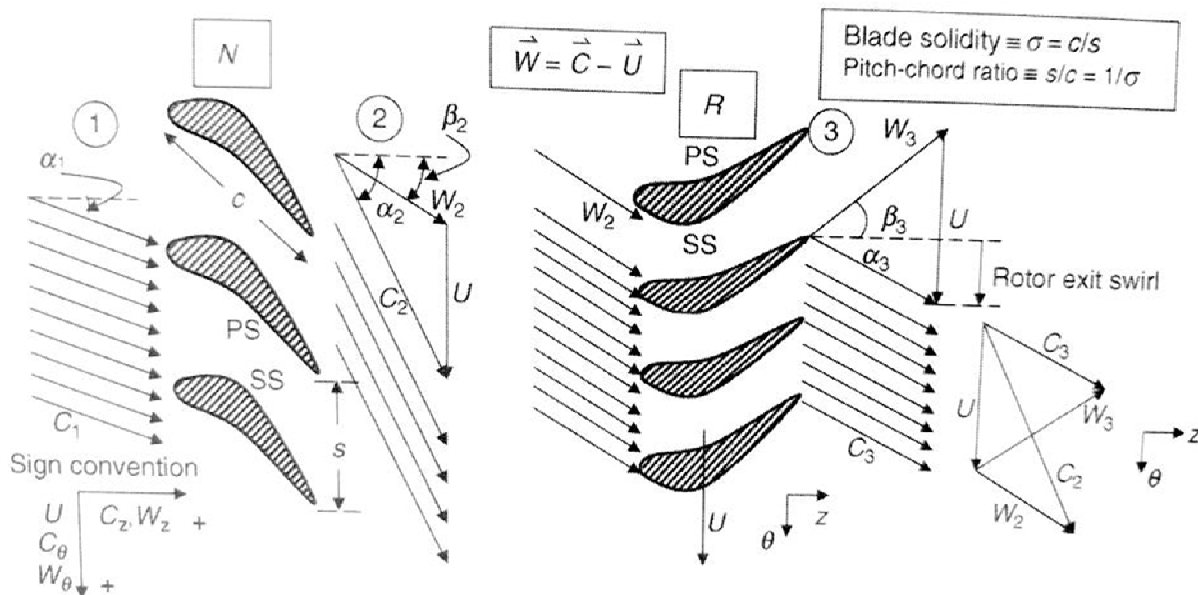


Figure 5.1: Definition Sketch for Turbine Stage Analysis [7]

GasTurb and the RFP determine the power requirements for the HPT and the LPT respectively. Given that the shaft has a mechanical efficiency $\eta_m = 0.995$ for power transmission, the power required is calculated to be 2060 hp for the HPT and 1608 hp for the LPT. The Euler Turbine Equation (Eqn. 5.1) is used at pitchline to calculate the power produced from each rotor.

$$\dot{\phi}_{\text{rotor}} = -\dot{\phi}_{\text{fluid}} = \dot{m}\omega[(r_2C_{\theta 2}) - (r_3C_{\theta 3})] \quad \text{Eqn. 5.1}$$

Furthermore, the thermodynamic relations for power and total temperature are used to calculate the total temperature drop across each turbine spool.

$$\dot{w}_{\text{rotor}} = -\dot{w}_{\text{fluid}} = \dot{m}[h_{t2} - h_{t3}] = \dot{m}c_p[T_{t2} - T_{t3}] \quad \text{Eqn. 5.2}$$

Table 5.2. Stage Design for the High-Pressure Turbine

		HPT							
		streamline	M (~)	Mr (~)	C (ft/s)	α (deg)	β (deg)	Um (ft/s)	W (ft/s)
Stage 1	Inlet (1)	hub	0.35		828	0.0	0.0	0	0
		mean	0.35		828	0.0	0.0	0	0
		tip	0.35		828	0.0	0.0	0	0
	N (2)	hub	1.10	0.70	2422	70.0	57.6	972	1544
		mean	1.10	0.67	2422	70.0	56.1	1045	1483
		tip	1.10	0.65	2422	70.0	54.4	1117	1424
	R (3)	hub	0.40	0.70	891	-21.6	-57.5	972	1541
		mean	0.26	0.70	852	-13.4	-57.4	1097	1537
		tip	0.38	0.70	831	-4.7	-57.3	1222	1533
Stage 2	N (4)	hub	0.90	0.52	1889	64.0	41.2	972	1101
		mean	0.87	0.47	1824	63.0	32.7	1094	984
		tip	0.84	0.42	1764	62.0	22.4	1216	896
	R (5)	hub	0.42	0.72	869	-17.6	-56.1	972	1487
		mean	0.40	0.72	831	-4.2	-55.8	1158	1474
		tip	0.40	0.75	830	3.9	-57.2	1343	1530

The total power produced by the HPT is 2063 hp, a 3 hp increase from the desired value. As can be seen in Table 5.2, the nozzle exit Mach number is 1.1 and the flow is subsonic through the rest of the spool. Similarly, Table 5.3 shows that the first nozzle exit Mach number is 1.1 and the flow is subsonic throughout the rest of the spool. Furthermore, as can be noted by the flow angle α , there is little swirl at the exit of the LPT.

Table 5.3. Stage Design for the Low-Pressure Turbine

LPT									
		streamline	M (~)	Mr (~)	C (ft/s)	α (deg)	β (deg)	Um (ft/s)	W (ft/s)
Stage 1	Inlet (6)	hub	0.38		793	0.0	0.0	0	0
		mean	0.36		759	0.0	0.0	0	0
		tip	0.35		724	0.0	0.0	0	0
	N (7)	hub	1.10	0.75	2118	68.0	56.6	761	1441
		mean	1.10	0.68	2117	69.0	54.6	909	1310
		tip	1.10	0.61	2117	70.0	52.1	1058	1180
	R (8)	hub	0.47	0.75	910	-29.3	-56.7	760	1444
		mean	0.40	0.71	768	-8.7	-55.9	1005	1353
		tip	0.38	0.70	735	10.0	-57.2	1250	1336
Stage 2	N (9)	hub	0.96	0.43	1748	63.0	45.1	760	1124
		mean	0.83	0.41	1541	60.5	24.2	1001	832
		tip	0.67	0.38	1263	55.0	-16.0	1241	753
	R (10)	hub	0.46	0.44	826	-16.1	-51.3	760	1268
		mean	0.42	0.42	764	6.6	-53.2	1101	1266
		tip	0.40	0.40	724	0.3	-63.3	1443	1611

The degree of reaction plays a critical role in stage loading and efficiency. The stage degree of reaction is calculated using equation Eqn. 3 and summarized in Table 5.4.

$${}^{\circ}R = 1 - \frac{C_{\theta 2} + C_{\theta 3}}{2U} \quad \text{Eqn. 5.3}$$

Table 5.4. Stage Degree of Reaction

	HPT		LPT	
	Stage 1	Stage 2	Stage 1	Stage 2
°R	0.053	0.324	0.074	0.351
Pressure Ratio	0.50	0.57	0.50	0.59
Power (hp)	1205	859	977	641

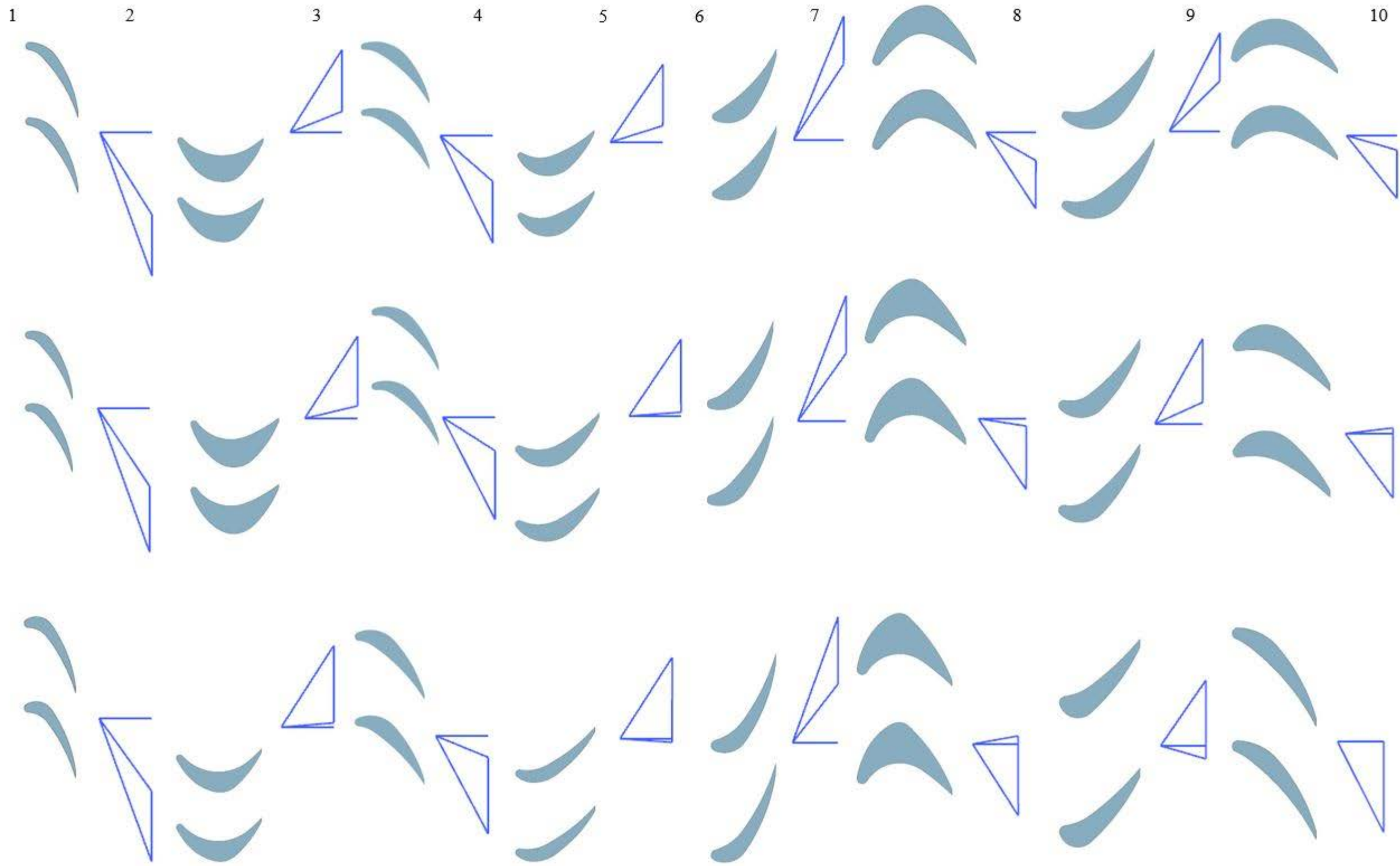


Figure 5.2 Velocity Triangles at Hub, Mean and Tip

In light of an un-cooled design strategy for the SF-1600 gas turbine engine, an adiabatic flow is assumed for the aerothermodynamic analysis of the turbine. The maximum total temperature in the turbine is designed to be $T_t = 2560^\circ\text{R}$, the maximum gas static temperature in the turbine is calculated to be $T_g = 2513^\circ\text{R}$, and the maximum adiabatic wall temperature in the turbine is calculated to be $T_{aw} = 2516^\circ\text{R}$. Using a ceramic matrix composites (CMCs), defined in section 10.3, all temperatures lie below the maximum allowable temperature of the CMCs of 2660°R [4]. The inlet properties are obtained from GasTurb and then the calculations are performed using the procedures outlined in Ref 7 and Ref 14. For the turbine, $\gamma_{\text{HPT}} = 1.31$ and $\gamma_{\text{LPT}} = 1.33$ [29]. With the aerothermodynamic calculations and Mach number, the annulus area is calculated and the blade height is obtained. Thus, with the blade height and pitchline known, the three-stream analysis can be calculated at hub, mean, and tip. Table 5.5 and Table 5.6 show the results of the aerothermodynamic calculations.

Table 5.5: Temperatures and Pressures in the High Pressure Turbine

HPT						
		streamline	Tt (R)	T _{aw} (R)	Pt (psi)	P (psi)
Stage 1	Inlet (1)	hub	2560	2516	207	192
		mean	2560	2516	207	192
		tip	2560	2516	207	192
	N (2)	hub	2560	2182	205	99
		mean	2560	2184	205	99
		tip	2560	2186	205	99
	R (3)	hub	2211	2167	108	97
		mean	2202	2164	104	95
		tip	2198	2164	102	93
Stage 2	N (4)	hub	2211	1981	106	65
		mean	2202	1990	103	65
		tip	2198	2001	101	65
	R (5)	hub	1948	1906	61	55
		mean	1947	1911	59	53
		tip	1947	1914	57	51

Table 5.6. Temperatures and Pressures in the Low Pressure Turbine

LPT						
		streamline	Tt (R)	T _{aw} (R)	Pt (psi)	P (psi)
Stage 1	Inlet (6)	hub	1948	1905	61	56
		mean	1947	1909	59	54
		tip	1947	1913	57	53
	N (7)	hub	1948	1644	61	29
		mean	1947	1647	59	28
		tip	1947	1651	56	27
	R (8)	hub	1683	1633	32	28
		mean	1670	1639	30	27
		tip	1666	1640	27	24
Stage 2	N (9)	hub	1683	1476	32	18
		mean	1670	1513	29	19
		tip	1666	1562	27	20
	R (10)	hub	1487	1445	19	16
		mean	1490	1459	17	16
		tip	1481	1465	15	13

5.3 Turbine Blade and Annulus Sizing

As stated previously, the flow characteristics and choice of pitchline determine the blade height and hub and tip radii. Given that the blade heights are known, the aspect ratios are chosen to determine the chord length. It is recommended to use low aspect ratios ($AR < 2$) since they result in less separation along the wall [30]. As the blade height increases, however, larger aspect ratios are chosen to reduce the weight of the component. The choice of aspect ratio also affects the solidity. The optimum axial solidity is calculated by using Zweifel's methodology and a Zweifel Coefficient of 1. Zweifel introduced a loading parameter (ψ_z) that is "the ratio of the blade tangential force per unit span and axial chord to the difference of inlet stagnation pressure and the exit static pressure" [7]. This results in the following equation for the axial solidity:

$$\sigma_z \psi_z = \frac{2 \cos(\beta_2)}{\cos(\beta_1)} \sin(\beta_1 - \beta_2) \quad \text{Eqn. 5.4}$$

Choosing a loading parameter of $\psi_z = 1$, the optimum axial solidity is obtained. This is then corrected using the stagger angle (γ°) to give the optimum solidity. However, Farokhi [7] claims

that the optimum solidity calculated using Zweifel's methodology is not always accurate, therefore, the solidity is slightly modified. Given that noise is reduced when the number of blades follows the prime number rule [31], the aspect ratio is chosen to satisfy these requirements and those stated in the previous paragraph. The throat sizing of the nozzle and rotor is calculated using Eqn. 5.5 where α is used for nozzles and β is used for rotors.

$$o = s \cos(\alpha)$$

Eqn. 5.5

Figure 5.3 shows the Campbell frequency diagram. For the number of blades (Table 5.8 and Table 5.7) and the rotor speeds of the HPT and LPT, the blades lie outside of the range of the first and second bending and torsional modes.

Using the parameters obtained from these calculations, the blades can be designed with smooth area-contraction as shown in Figure 5.4. A constant-hub radius is chosen for both the HPT and the LPT. The area of the annulus can be calculated using Eqn. 10.16 [7]. Shrouded blades are chosen for the rotors to eliminate tip losses. Given the size of the spools, the team determined that the benefits far outweigh the minor weight/stress penalty. The thickness of the bling is calculated for each blade row and the thickness of the shroud is calculated for the rotors using

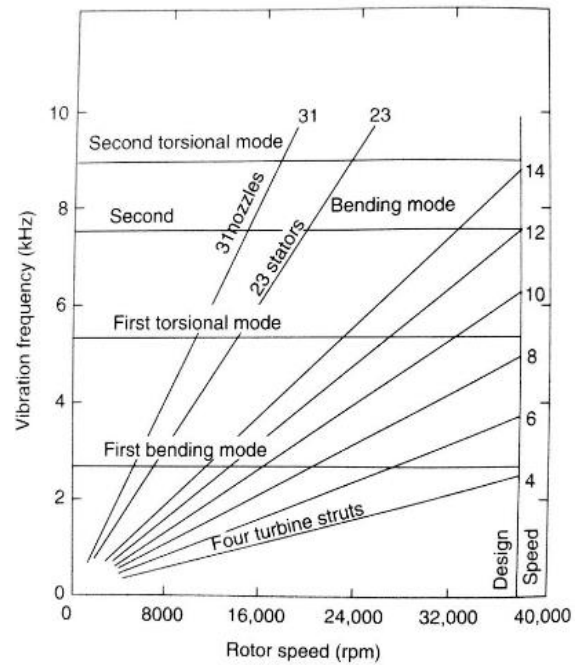


Figure 5.3: Campbell Frequency Diagram for a Turbine Blade [7]

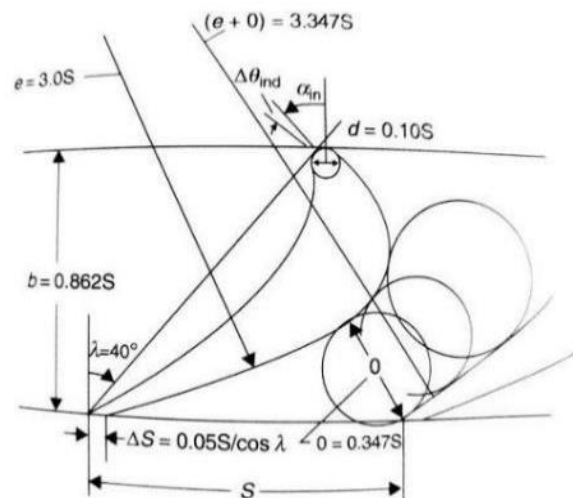


Figure 5.4: Blade Design [7]

standard equations for stress analysis. The blade and annulus design parameters are presented in Table 5.8, Table 5.7, and Table 5.9. The contour of the turbine is shown in Figure 5.5.

Table 5.8. Blade and Annulus Design Parameters

	HPT				LPT			
	Stage 1		Stage 2		Stage 1		Stage 2	
	N	R	N	R	N	R	N	R
h (in)	0.38	0.52	0.64	0.98	1.00	1.33	1.62	1.96
AR	0.47	1.16	0.80	1.30	0.90	1.80	1.30	1.90
σ	1.09	1.30	1.20	1.20	1.11	1.00	1.00	1.00
γ°	53.9	-2.2	40.8	-22.5	51.6	-2.0	38.9	-23.9
c (in)	0.81	0.45	0.80	0.75	1.11	0.74	1.25	1.03
s (in)	0.74	0.34	0.67	0.63	1.00	0.74	1.25	1.03
o (in)	0.25	0.19	0.30	0.35	0.36	0.41	0.61	0.62
n	23	53	27	31	19	29	17	23
cz (in)	0.48	0.45	0.61	0.70	0.69	0.74	0.97	0.94
Area(ft ²)	0.05	0.08	0.08	0.13	0.13	0.24	0.24	0.37

Table 5.7. Blade and Shroud Thicknesses

	t_bling (in)	t_shroud (in)
HPT	0.48	0.05
LPT	0.16	0.05

Table 5.9. Hub, Mean, and Tip Radii

	r (in)									
	I (1)	N (2)	R (3)	N (4)	R (5)	I (6)	N (7)	R (8)	N (9)	R (10)
hub	2.56	2.56	2.56	2.56	2.56	2.56	2.56	2.56	2.56	2.56
mean	2.76	2.76	2.89	2.89	3.05	3.09	3.06	3.39	3.37	3.71
tip	2.96	2.94	3.22	3.20	3.54	3.61	3.56	4.21	4.18	4.86

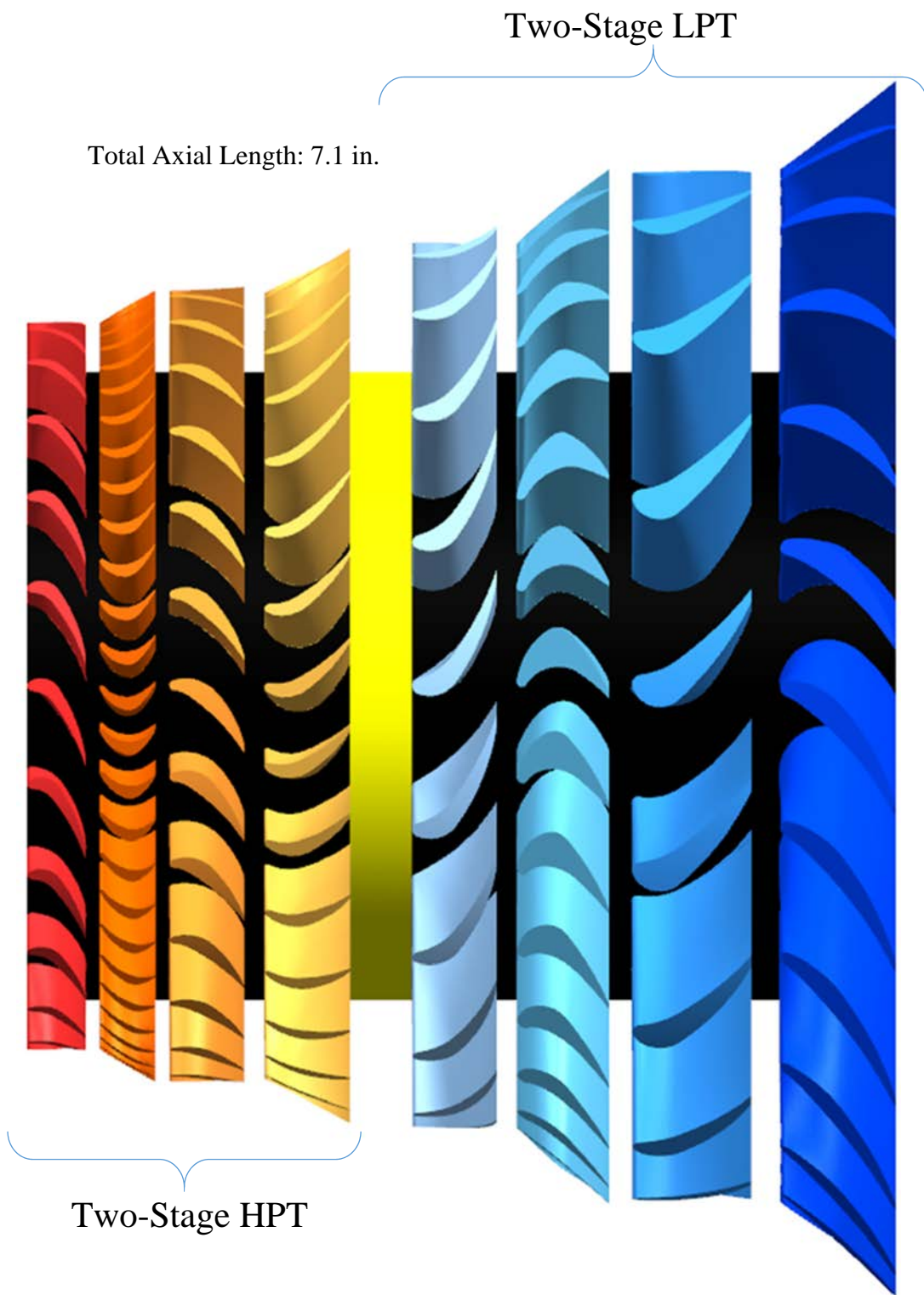


Figure 5.5: Contour of Turbine

5.4 Turbine Blade Material Selection and Stress Calculations

The SF-1600 uses ceramic matrix composites to eliminate the necessity of cooling in the gas turbine. Given that the maximum temperature of the turbine is 2100°F, COI Ceramics Nextel AS-N610 Oxide Ceramic Matrix Composite – Aluminosilicate is chosen for the gas turbine since it has a maximum temperature of 2660°R [4]. Since the maximum $T_t = 2560^\circ\text{R}$, the maximum $T_g = 2513^\circ\text{R}$, and the maximum $T_{aw} = 2516^\circ\text{R}$, the choice of this material guarantees an uncooled turbine. The blade stress due to centrifugal force is calculated using the AN^2 rule where A is the flow area and N is the shaft angular speed [7]. Equation 5.7 gives the relationship of the centrifugal stress to AN^2 . The thermal expansion stress on the blades is significant given the temperature changes experienced by the gas turbine. Equation 5.8 is used to calculate the thermal stresses on the blades.

$$A = 2\pi r_m(r_t - r_h) \quad \text{Eqn. 5.6 [7]}$$

$$\sigma_c = \frac{\rho_{blade}\omega^2 A}{4\pi} \left(1 + \frac{A_t}{A_h}\right) \quad \text{Eqn. 5.7 [7]}$$

$$\sigma_t = \alpha E \Delta T \quad \text{Eqn. 5.8 [7]}$$

Table 5.10 shows that the total stresses lie beneath the tensile strength of 52900 psi resulting in positive margins of safety for each blade.

Table 5.10: Turbine Blade Stresses and Margins of Safety

	σ_c (psi)	σ_T (psi)	total (psi)	AN^2 (in ²)	MS
N (2)		-2.85E+04	2.85E+04	1.37E+08	0.85
R (3)	1.04E+04	-2.75E+02	1.07E+04	2.48E+08	3.95
N (4)		-1.43E+04	1.43E+04	2.42E+08	2.69
R (5)	1.64E+04	-5.84E+03	2.22E+04	3.89E+08	1.38
N (7)		-2.26E+04	2.26E+04	2.45E+08	1.34
R (8)	1.87E+04	3.81E+02	1.83E+04	4.45E+08	1.89
N (9)		-1.03E+04	1.03E+04	4.35E+08	4.13
R (10)	2.86E+04	-4.05E+03	3.27E+04	6.81E+08	0.62

5.5 Smith Chart

A Smith Chart is used to show the effect of stage loading and flow coefficient on the efficiency of an axial turbine [32]. The calculations for the stage-loading factor and stage flow factor are plotted onto the smith chart for each stage respectively. Equations 5.6 and 5.7 are used to determine the stage-loading factor and stage flow coefficient respectively. After plotting these points on the Smith Chart, the turbine efficiencies range between 90+% to 94+%, which are deemed excellent in the preliminary design stage.

$$\varphi = C_z/U \quad \text{Eqn. 5.6 [7]}$$

$$\psi = 1 + \varphi(\tan(\beta_2) - \tan(\beta_1)) \quad \text{Eqn. 5.7 [7]}$$

Table 5.11: Flow Coefficient and Stage Loading Factor for Each Stage

	HPT		LPT	
	Stage 1	Stage 2	Stage 1	Stage 2
flow coefficient	0.755	0.716	0.755	0.689
stage loading factor	2.25	1.46	2.08	1.14

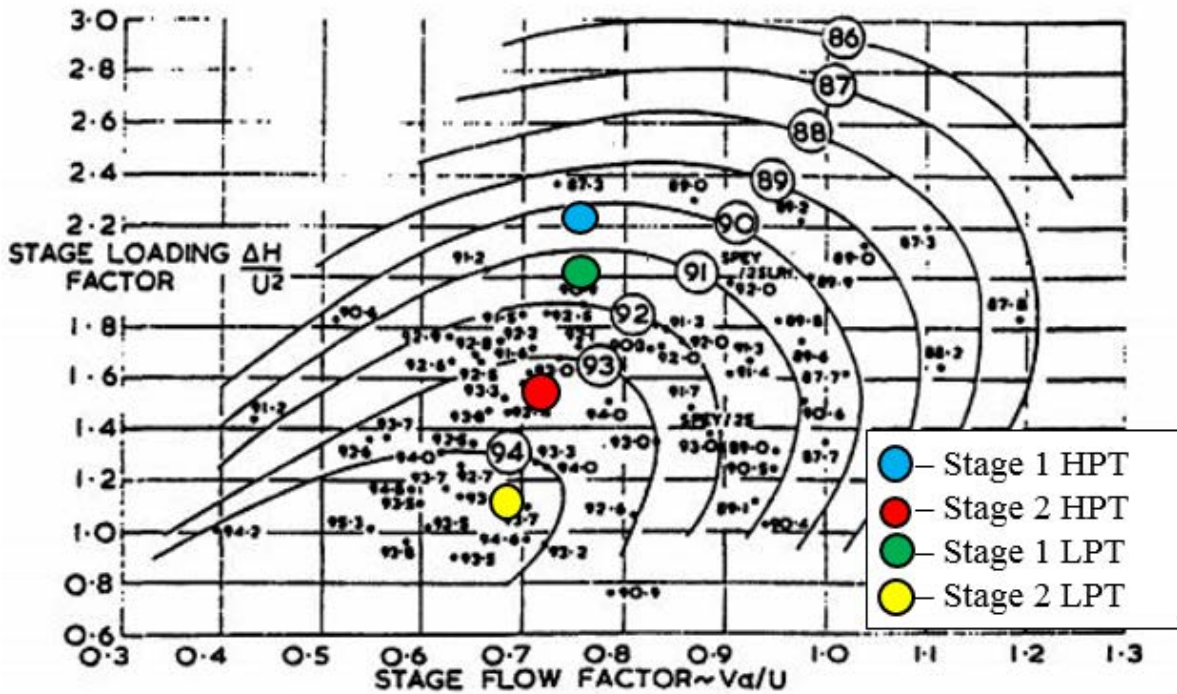


Figure 5.6: Smith Chart [31]

5.6 Turbine Flow Parameters

Table 5.12: HP Turbine Flow Data

Flow Station Data: HP Turbine	
Inflow (lb/s)	8.22
Corrected Inflow (lb/s)	1.295
Inflow Total Pressure (psi)	207
Inflow Total Temperature (°R)	2560
Inflow Fuel-air-Ratio	0.0209
Inflow Mach #	0.348
Inflow Area (in ²)	6.9408
Pressure Ratio	0.29

Table 5.13: PT Flow Data

Flow Station Data: Power Turbine	
Inflow (lb/s)	8.22
Corrected Inflow (lb/s)	4.01
Inflow Total Pressure (psi)	59.3
Inflow Total Temperature (°R)	1950
Inflow Fuel-air-Ratio	0.0209
Inflow Mach #	0.364
Inflow Area (in ²)	20.304
Pressure Ratio	0.29

6.0 Subsonic Nozzle

The nozzle is sized such that the nozzle pressure ratio matches that set forth by the cycle analysis performed in GasTurb. The characteristics of this bifurcated nozzle can be seen in Table 6.1. This nozzle will be made of Nickel 22. This alloy has excellent temperature, anti-corrosion properties, and it has good resistance to impact [68]. The nozzle will be manufactured by hydroforming extruded tubing. Tooling will be designed to match the nozzle geometry. Figure 6.1 shows the CAD model of the SF-1600 nozzle.

The geometric characteristics of the nozzle are depicted on Table 6.1.

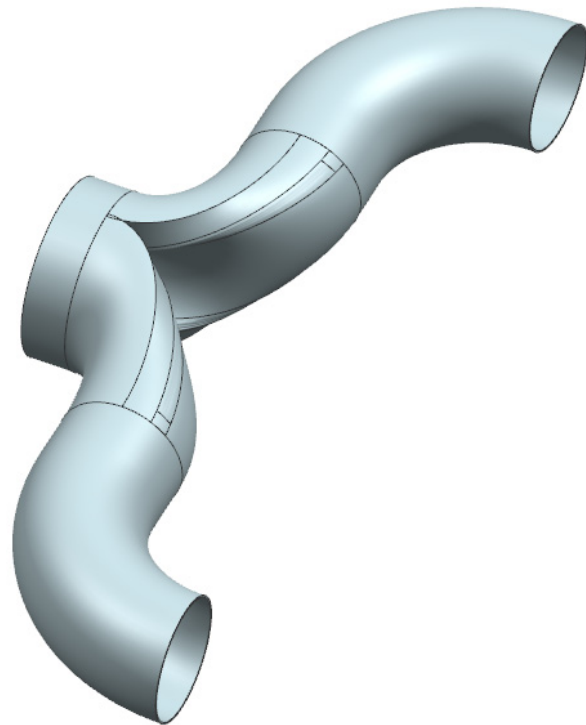


Figure 6.1: SF-1600 bifurcated nozzle

Table 6.1: SF-1600 Nozzle Parameters

Parameter	Value
Exit Area(in ²)	73.6
Exit Velocity at takeoff (ft/s)	578
Exit Velocity at cruise (ft/s)	615
Length(ft)	1.47

6.1 Nozzle Flow Station Data

Table 6.2: Exhaust Duct Flow Data

Flow Station Data: Exhaust Duct	
Inflow (lb/s)	8.22
Corrected Inflow (lb/s)	12.72
Inflow Total Pressure (psi)	15.88
Inflow Total Temperature (°R)	1451
Inflow Fuel-air-Ratio	0.0209
Inflow Mach #	0.267
Inflow Area (in ²)	53.712
Pressure Ratio	0.99

Table 6.3: Nozzle Flow Data

Flow Station Data: Nozzle	
Inflow (lb/s)	8.22
Corrected Inflow (lb/s)	12.85
Inflow Total Pressure (psi)	15.72
Inflow Total Temperature (°R)	1451
Inflow Fuel-air-Ratio	0.0209
Inflow Mach #	0.319
Inflow Area (in ²)	73.6
Pressure Ratio	1.07

7.0 Gearbox Design

This section explains the gearbox system concept for the SF-1600, which shows both the reduction and accessories gearing systems. The gearbox system design, as a whole, was guided by both the SF-1600 inlet design, and current industry examples.

7.1 Reduction Gearbox Design and Configuration

Using industry-proven practice, the configuration chosen is a two-stage gear reduction with both primary

and secondary stages being planetary gears. The gearbox internal configuration is shown in Figure

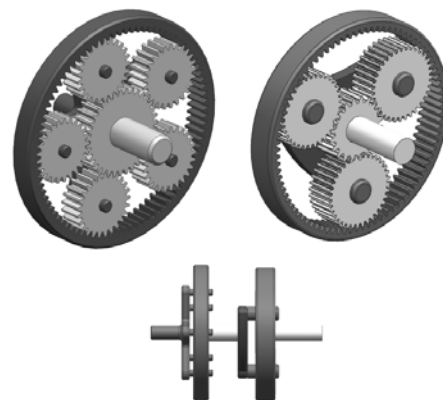


Figure 7.1: Internal Reduction Gear Configuration [33]

7.1, while Figure 7.2 shows the overall engine configuration used for the SF-1600. Two configurations were considered for this engine and would work for this type of reduction gear, in-line or offset. After comparing at both options, the design team chose an in-line reduction gearbox for a multitude of reasons. The in-line gearbox is the industry standard for current similar-sized engines, such as the General Electric GE93 and PT6A-68C. The in-line configuration is also better for the reduction ratio achieved by the SF-1600, while the off-axis gearboxes are better for lower reduction ratios. Another main disadvantage of the off-axis gearing is the added weight and volume that the engine needs, while the in-line gearing is more compact and lighter. As discussed in the turbine section, the angular shaft speed of the low-pressure or power turbine (LPT) turns the power shaft that connects to the two-stage reduction gearbox. The inlet is placed below the reduction gearbox. This inlet configuration minimizes any intake interference from the gearbox or power shaft.

7.2 Reduction Gear Calculations

There are a few calculations that can be accomplished to determine weight and sizing of the reduction gear system. First, the gear reduction ratio needed for the SF-1600 can be calculated by taking the ratio of the

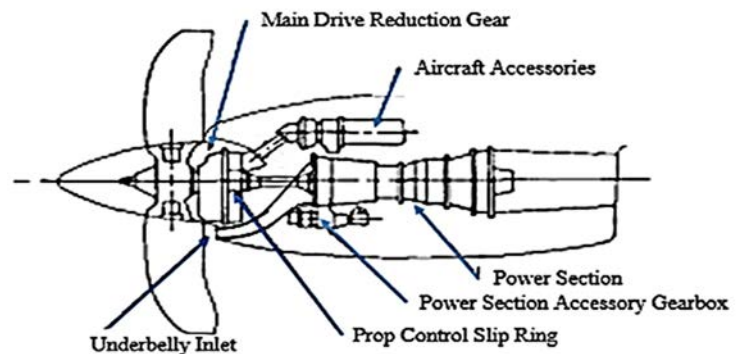


Figure 7.2: Overall Gearbox System Configuration [35]

angular speed of the power shaft at takeoff before the reduction gearbox and the angular speed of the output shaft that connects to the propeller at the same flight condition. The gear reduction can be seen in the equation below,

$$Total\ Reduction\ Ratio,\ RR_{tot} = \frac{\omega_{shaft@TO}(rpm)}{\omega_{prop@TO}(rpm)} = \frac{34,000\ rpm}{2,000\ rpm} = 17:1 \quad Eqn.\ 7.1$$

The reduction ratio needed is a driving design factor in the sense that it mainly decides how many stages of reduction will be needed. According to Table 1.4 from Reference 66 and Dr. Sorem, a mechanical engineering professor at the University of Kansas, two reduction stages should be used for reduction ratios between 5:1 and 25:1.

Then, given that the power shaft is connected directly to the reduction gear, the angular speed of the first sun gear and the LPT are equal. The teething arrangement will then be chosen for each part of the reduction gearing. This arrangement will affect the angular speed, torque, and reduction ratio experienced in each gear. The angular speed, ω , of each portion of the first stage reduction gearing are,

$$\omega_{sun} = \omega_{carrier(previous\ stage)} = \omega_{LPT} = 34,000\ rpm\ (3,560\ \frac{rad}{s}) \quad \text{Eqn. 7.2}$$

$$\omega_{Total\ Planet} = N_{sun} + \frac{N_{planet} - N_{ring}}{N_{planet} * N_{ring}} = -11,333\ rpm\ (-1187\ \frac{rad}{s}) \quad \text{Eqn. 7.3}$$

$$\omega_{Carrier} = \frac{N_{sun}}{N_{sun} + N_{ring}} = 6,800\ rpm\ (712\ \frac{rad}{s}) \quad \text{Eqn. 7.4}$$

with N being the number of teeth on each gear and the +/- sign denoting clockwise (CW) or counterclockwise (CCW) rotation (+ being CCW) [66]. The second stage can be calculated in the same way.

The torque, τ on each of the first stage sun gear can be calculated by using the actual power from the LPT,

$$\tau_{sun} = \frac{P_{actualLPT}}{\omega_{sun}} = 279\ lb - ft\ (380\ N - m) \quad \text{Eqn. 7.5}$$

The rest of the torques can be calculated using the angular velocity ratios between each gear.

Finally, the weight of the gearbox is calculated using the density of the material used, ρ_{gb} , and the overall volume of the gearbox, given in the CAD modeling program, Siemens NX 8.5.

The weight is,

$$W_{GB} = \rho_{gb} \left(\frac{lb}{in^3} \right) * V_{gb}(in^3) = 17.9 lbf$$

Eqn. 7.6

7.3 Accessory Gearing

While the power shaft drives the gears for to the prop, and torque meter, it also drives the accessory gears, which include the oil and fuel pumps using a series of bevel gears, shown in Figure 7.3. It also drives the gearing for the starter motor. Figure 7.2 shows how the accessories will be configured as well.



Figure 7.3: Bevel Gear Connection to Propeller Shaft

7.4 Gearbox Systems Materials

The gearbox weight accounts for a sizable portion of the engine weight because of the material needed to handle the speed and torque seen by the reduction gearing. The material was chosen based on current industry materials and material properties needed. The material chosen is the steel alloy Carburizing Bearing and Gear Steel (CBS) 600. The alloy has relatively high strength and fracture toughness, as well as a long service life. The alloy also contains chromium, which helps with controlling grain structure and adds wear resistance. The gearing will be carburized to increase surface hardness and fracture toughness, while keeping the density relatively low compared to other alloys. Carburizing, which is a type of case hardening, is the process of hardening a thin layer of a component made of steel, while leaving the inner metal the same. It is done by placing a steel gear is put in a carbon rich environment and leaving it at a high temperature for a set amount of time, and then finish by quenching the component [39]. The material properties of this carburized steel alloy are shown below.

Table 7.1: Gearbox Material Properties [68]

Material	Density (lb/in ³)	Hardness (HRC)	Tensile Strength, Yield/Ultimate (ksi)	Fracture Toughness (ksi-in ^{1/2})	Critical Temperature (°F)
CBS-600	0.282	62	181/220	42-52	1480

7.5 Conclusions and Overall Design Parameters

The gearbox for a turboprop engine allows each rotor section of the engine to operate at their respective max efficiency. The helical gearing used will increase reliability, and service life. The author concludes with the initial design parameters for the gearbox, which can be found in Table 7.3 and Table 7.2.

Table 7.3: Gearbox Design Parameters at Takeoff

Gearbox Volume, V_{gb} (in ³)	63.4
Gearbox Weight, w_{gb} (lbf)	17.9
First Stage Reduction Ratio	5
Number of Teeth on Sun Gear, N_{sun1}	24
Number of Teeth on Planet Gears, $N_{planet1}$	36
Number of Teeth on Ring Gears, N_{ring1}	96
Second Stage Reduction Ratio	3.4
Number of Teeth on Sun Gear, N_{sun2}	40
Number of Teeth on Planet Gears, $N_{planet2}$	28
Number of Teeth on Ring Gears, N_{ring2}	96
Total Reduction Gearbox Ratio	17
Gearbox Efficiency (From Ref. 7)	.995

Table 7.2: Gearing Angular Speeds and Torque at Takeoff

Angular Speed of the LPT, ω_{LPT} (rpm)	34,000 (3,560 rad/s)
First Stage Gearing	
Angular Speed Sun, ω_{sun1} (rad/s)	3560
Angular Speed Planet, $\omega_{planet1}$ (rad/s)	-1187
Angular Speed Carrier, $\omega_{carrier1}$ (rad/s)	712
Torque on Sun Gear, τ_{sun1} (lbf-ft)	279
Torque on Planet Gears, $\tau_{planet1}$ (lbf-ft)	-93.1
Torque on Carrier Gear, $\tau_{carrier1}$ (lbf-ft)	55.8
Second Stage Gearing	
Angular Speed Sun, ω_{sun2} (rad/s)	712
Angular Speed Planet, $\omega_{planet2}$ (rad/s)	-509
Angular Speed Carrier, $\omega_{carrier2}$ (rad/s)	209
Torque on Sun Gear, τ_{sun2} (lbf-ft)	55.8
Torque on Planet Gears, $\tau_{planet2}$ (lbf-ft)	-69.9
Torque on Carrier Gear, $\tau_{carrier2}$ (lbf-ft)	19.9
Angular Speed of the Propeller, ω_{prop} (rpm) (From RFP)	2000 (209 rad/s)

8.0 Bearing Systems

This section will cover the bearing system configuration for the SF-1600 engine. The bearing systems were designed using the descriptions and methods of Kerrebrock [40] as a key reference.



Figure 8.1: Ball and Roller Bearing Depiction [41]

8.1 Bearings Design

The bearings of an engine provide stability and enhance efficiency for the rotating machinery. The characteristics of these bearings are affected by three major design aspects: type, material, and configuration or placement on the parts. The two main types of bearings looked at for the SF-1600 were the standard ball and roller bearings combination, depicted in Figure 8.1, and the more recently investigated active magnetic bearings. There are valid reasons to use both systems. The ball and roller systems have been studied and used for a long period, which makes the manufacturing process easier, and provides exact performance limits. Also, they provide a higher load capacity in terms of the surface area of the bearing sleeve than their magnetic bearing counterparts [42]. On the other hand, magnetic bearings have a higher theoretical documented operating speed (DN) and max operating temperature. They also have a lower power consumption. The problem with active magnetic bearings is that they have not yet been proven on aircraft turbomachinery and, given the RFP entry into service date of 2025, the technology may not be

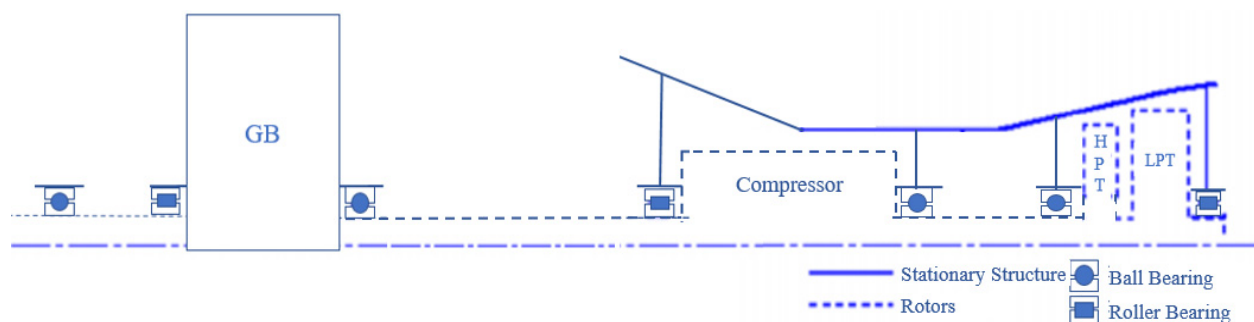


Figure 8.2: Ball and Roller Bearing Configuration [40]

available to use. Because of this, the decision was made to use the standard ball and roller bearings on the SF-1600. The configuration for the bearings can be seen in Figure 8.2

8.2 Bearing Materials

The design requirements for bearings for jet aircraft turbomachinery include spatial stability, high heat and wear resistance, a long service life as well as high reliability, and high strength. There

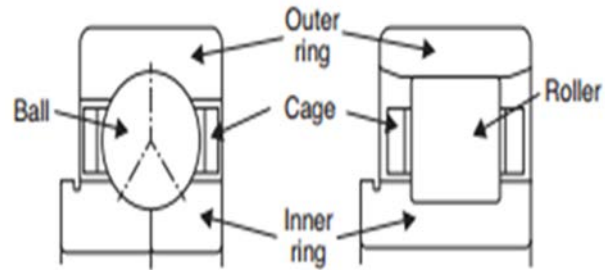


Figure 8.3: Roller and Ball Bearing Components [43]

are several parts to each type of bearing used, which is shown in Figure 8.3. The inner and outer rings, as well as the ball and roller bearings need to be made of a material that has a high heat-resistance and a high fracture toughness. The carburized steel known as American Iron and Steel Institute (AISI) M50NiL fits both needs. The material for the cage must also be chosen. Using current aircraft examples, the cages will be Society of Automotive Engineers (SAE) 4340 alloy steel [43]. The properties of both materials can be seen in the table below.

Table 8.1: Bearing Material Properties [43-46]

Material	Density (lb/in ³)	Hardness (HRC)	Tensile Strength, Yield/Ultimate (ksi)	Fracture Toughness (ksi-in ^{1/2})	Fatigue Life (L ₁₀ Dynamic Life Factor)
AISI M50NiL	0.285	47	174/203	50-52	12-16
SAE 4340	0.284	30	103/161	45.5	~

9.0 Flow Path Through the SF-1600

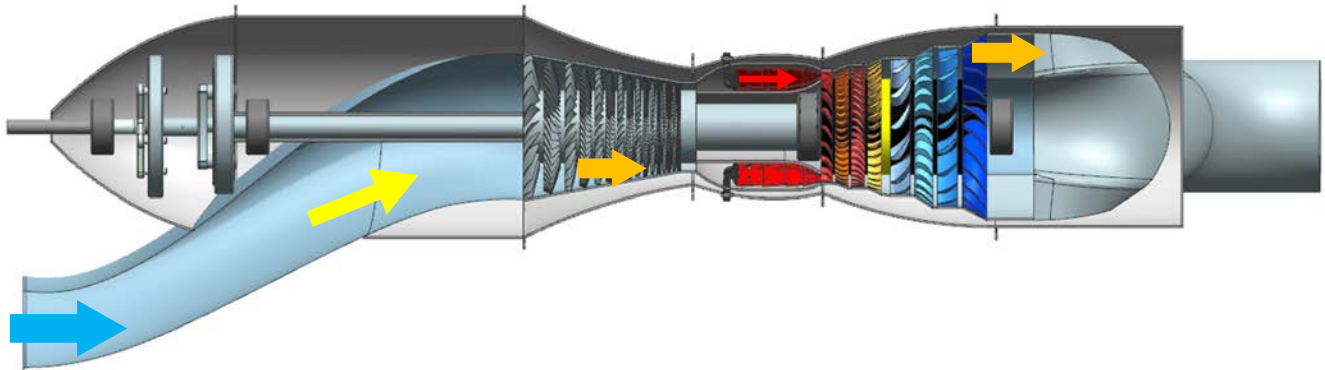


Figure 8.1: SF-1600 Flow Path

10.0 Manufacturing

10.1 Inlet materials

The inlet is made from composite materials in order to save weight, increase the smoothness of the structure, and recreate the complex geometries. For the manufacturing process of the inlet, prepreg fiberglass will be hand laid into the mold. After this, it is cured in an autoclave.

Figure 10.1 shows the manufacturing process of the inlet.

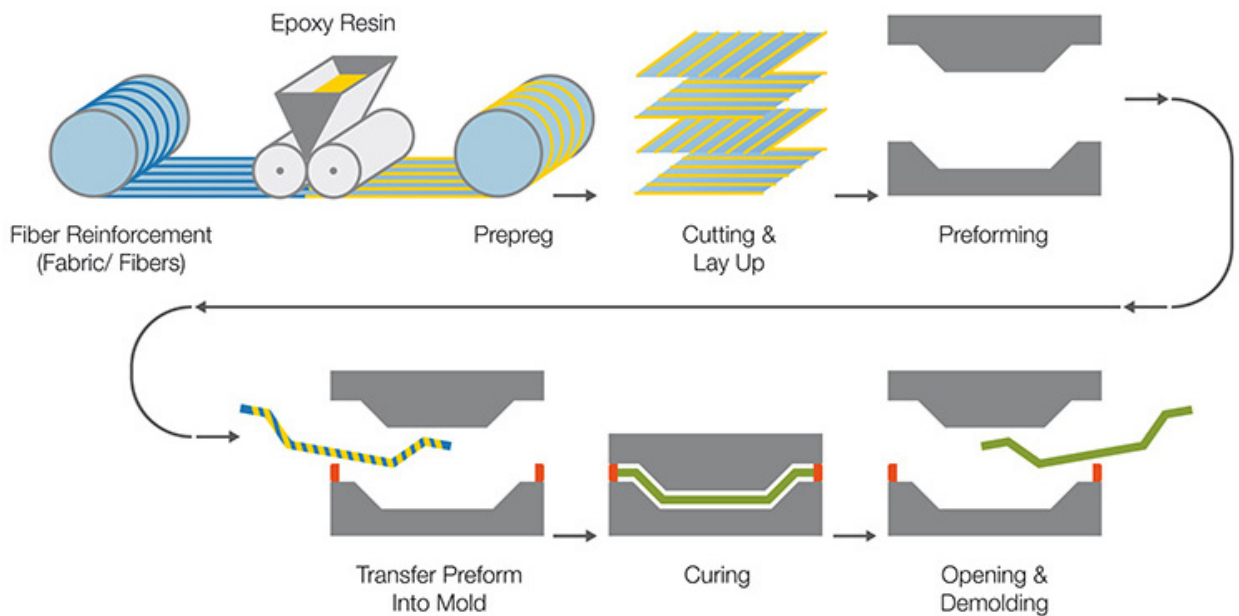


Figure 10.1: Manufacturing Process of the Inlet [63]

10.2 Compressor and Shaft New Technologies and Manufacturing Process

Compressor materials not only have to be able to resist high temperature generated by the compression of airflow, but they need to have high stiffness to weight ratio. The compressor will employ bladed rings or blings. The compressor rotor and stators of the engine will be made of TI-5Al-2.5Sn titanium alloy. This alloy has an allowable stress of 120 ksi which is higher than the 27550 psi centrifugal stress the blade will be subjected to. The blings will be manufactured using computer numerical control (CNC) milling. Figure 10.2 depicts a bling.



Figure 10.2: Bladed Ring [11]

10.3 Turbine and Combustor Liner Materials and Manufacturing

The aerospace industry in general is moving toward composite materials. In recent years, engine manufactures are investing heavily to replace as many metal parts with lighter composite materials. Ceramic matrix composites, or CMCs, are a type of composite material that is significantly lighter than other metals, such as nickel, used in engines.

CMCs can reduced fuel burn and CO₂ emissions because CMCs do not need as much cooling as metal. When the cooling flow is reduced, more air can be used in the combustor, reducing unburned hydrocarbon (UHC) emissions. The material cost of CMCs is generally 5% less than super alloys. SIC CMC (silicon carbide) has a capability to withstand temperatures of up to 2660 F [4] will be used for the turbine parts of the SF-1600.

The manufacturing process consist of SIC fibers woven at 90 and 0 degree angles, then they go through a chemical vapor infiltration process that grow the fibers of the SIC. After this,

the material goes through vapor infiltration one more time to increase the density and create the matrix.

In addition, the CMC can go through an additional process called polymer impregnation pyrolysis. After, the CMC has gone through the chemical vapor infiltration process, the CMC is impregnated with polymer. Finally, the material is put in the furnace. Some shrinkage will occur, so it is recommended to infiltrate the materials multiple times in order to compensate for this and reduce porosity. Figure 10.3 depicts the manufacturing process of SIC CMCs.

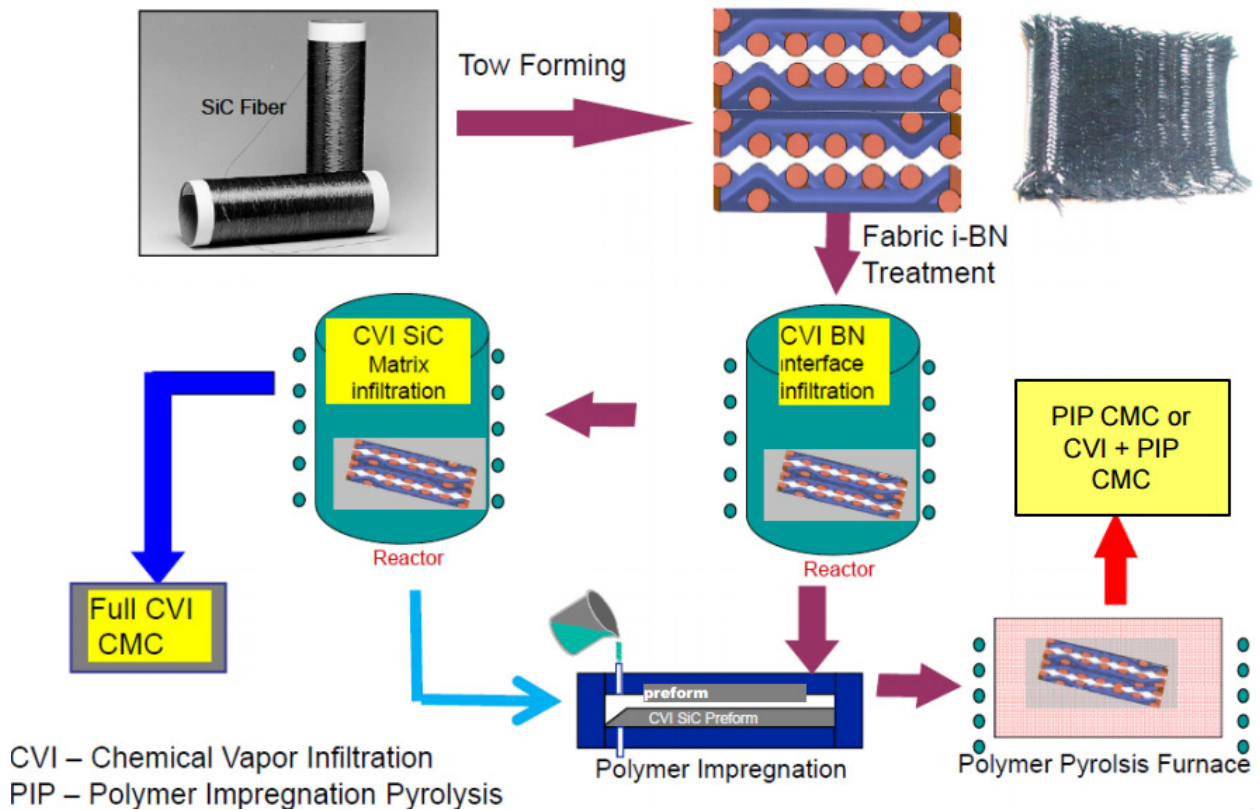


Figure 10.3: SIC CMC's Manufacturing Process [47]

The use of CMC in moving parts of the turbines has already begun. General Electric has developed a type of CMC that is capable of withstand higher temperatures than nickel alloys and it need less cooling than metals [48].

According to GE, this type of technology could reduce fuel consumption by 25%, improve the range by 30%, and provide 10% higher thrust [50]. The PT-6 will use CMCs in the turbine blades, vanes, shrouds, and flaps and seals.

10.4 **Combustor Liner Materials and Manufacturing Process**

The combustor liner of the SF-1600 will be made from CMCs. According to recent studies [4], the use of CMC in combustor liner system that operate at temperatures of 2660 F and 60 atm could mean a 60% reduction in cooling necessity and 40% reduction in NOx emission compare to metallic liners. Fretting coating can be used to prolong the wear life. NASA has developed advanced fretting coating that can offer 3 to 10 times fretting resistance [64]. The liner will be manufacture using the same process shown on the turbine section (Figure 10.3).

10.5 **SF-1600 Materials**

The SF-1600 engine materials are depicted in the following figure:

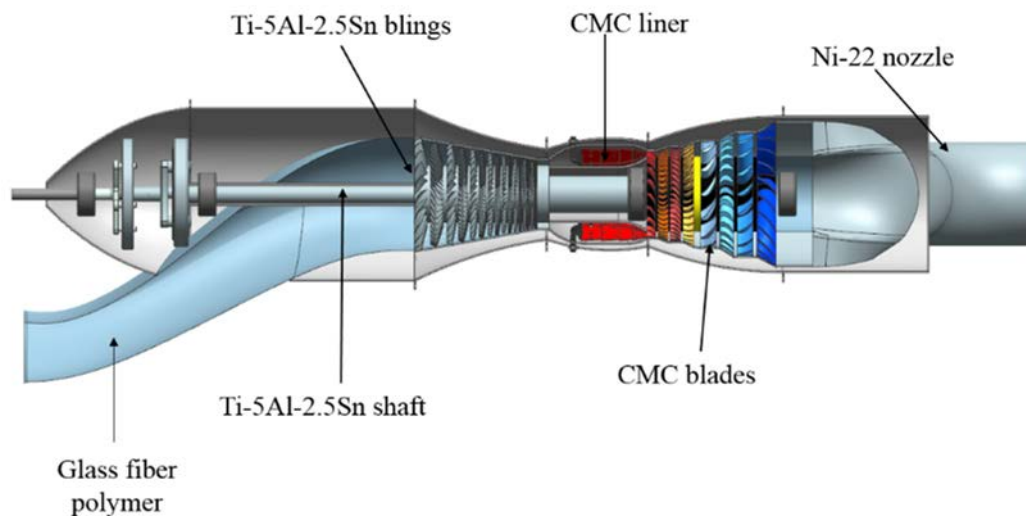


Figure 10.4: Cutout View of the SF-1600

11.0 **Engine Weight Savings Analysis**

Weight savings of the SF-1600 come from many sources. All of the following sources are listed below:

- 18% decrease in mass flow yields approximately an 18% decrease in flow area. Using the $r^2 - r^3$ rule, this gives an approximate engine volume decrease of 25% and corresponding decrease in weight.
- CMC's are used for the turbine and combustor, which yields an additional 30% reduction in weight for those components from the density decrease.
- Integrally bladed rings are used for the turbine and compressor, which provide up to a 70% weight savings in those components [7, 54].

Oil and fuel piping as well as wiring weights are approximately the same between the SF-1600 and the PT6. The gearbox of the SF-1600 will be slightly higher due to the increase in power over the PT6. All of these combined together will reduce the weight of the SF-1600 well more than the 5% RFP requirement. Using CAD volumes and densities, a baseline core weight can be found and the engine dry weight can be calculated by adding system weights calculated using methods from Raymer [69].

Table 11.1: Component Weight

	Inlet	Compressor	Combustor	Turbine	Nozzle	Gearbox	Outer Case	Shafts	FADEC
Volume (in ³)	42.7	49.5	21.11	100	136.5	63.4	177	77.2	12
Density (lbs/in ³)	0.075	0.162	0.141	0.102	0.162	0.282	0.162	0.199	0.9
Weight (lbs)	3.2	6.885	5.188	10.2	22.1	17.9	28.6	15.35	10.8

Table 11.2: Engine Dry Weight

W_{engine} (lbs)	W_{cooling} (lbs)	W_{controls} (lbs)	$W_{\text{engine start}}$ (lbs)	W_{DRY} (lbs)
121.8	24.6	16.7	15.7	178.8

12.0 Identification and Selection of Engine Subsystems

The following sections outline the design of the SF-1600 engine subsystems.

12.1 Oil and Lubrication System

The SF-1600 will employ a dry-sump type lubrication system. This system consists of seven spur-gear pumps, one pressure and five scavenge. Each one uses the HPT shaft to drive the gears. The configuration used for the SF-1600 is shown in Figure 12.1. The oil cooler was chosen as a fuel-oil heat exchanger, which is standard for jet engines, instead of an air-oil heat exchanger. The fuel-oil heat exchanger has a few advantages over the air-oil type. It requires a smaller volume, and still provides the same cooling capacity. The fuel-oil type also does not need airflow to function properly. Therefore, it allows for flexibility regarding where it is placed in the engine, and it also works during any ground maneuvering. The pressure pump allows the oil to move from the oil tank and be distributed to the reduction and accessory gearbox systems as well as the bearings for each compartment. The oil tank is monitored by using a thermostatic sensor. The engine also can use oil to heat the fuel passing between the fuel tank and the pressure pump. This fuel will then help with any de-icing, if needed.

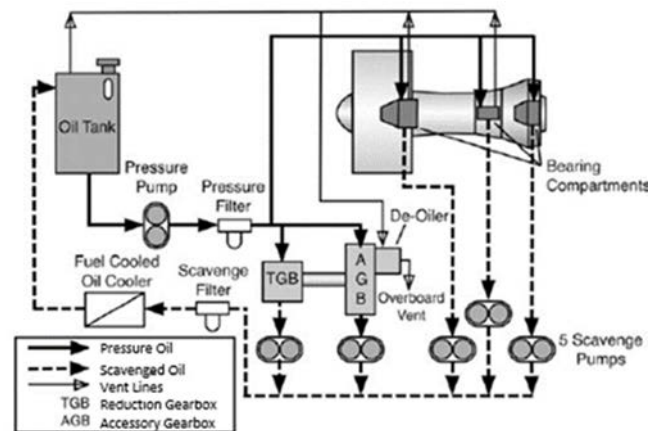


Figure 12.1: Lubrication System Configuration [55]

12.1.1 Oil Selection

For oil selection, the standard for current jet aircraft, and jet aircraft for the near future, follow the lubricating oil performance specification, MIL-PRF-23699F STD or O-156 [43]. The exact oil used for this engine is the AeroShell Synthetic Turbine Oil 500. AeroShell 500 oil meets and exceeds the performance specification. This includes a low pour point and a high flash point, as well as providing thermal stability for the engine. Another oil key characteristic is a high viscosity at low temperature and low viscosity at high temperatures. It is also resistant against pressure and oxidation. The properties of this lubricant is shown in Table 12.1.

Table 12.1: AeroShell 500 Oil Properties compared to Mil-Spec [56]

Property	MIL-RPF-23699F STD Requirements	AeroShell 500 Typical Properties
Oil Type	Synthetic ester	Synthetic ester
Viscosity @ 212°F, cSt	4.9-5.4	5.4
@ 100°F, cSt	25 min	25.56
@ -40°F, cSt	13,000 max	8,996
Flash Point, °F	475 min	493
Pour Point, °F	-65.2 max	-103

12.2 Engine Control System

Full Authority Digital Engine Controllers (FADECs) are used to decrease the workload of the pilot. The FADEC monitors all engine aspects, aircraft aspects, and pilot inputs in order to come to a decision on things such as fuel flow, stator positions, bleed valve positions and more [57]. While there is no direct connection from pilot to engine, hence the engine controller is “full authority”, there are overrides for shutting down an engine quickly if need be.

The control system consists of an electronic controller that processes the signals and outputs the commands. The next unit of the FADEC is fuel-metering unit. Gear pumps on the auxiliary gearbox provide fuel pressure and flow. The fuel itself is used as a hydraulic fluid to actuate valves that regulate fuel flow into the injectors. This is also the primary source of actuation in the engine. The same fuel pressure actuates the variable stators and bleed valves.

Along with these control outputs of the FADEC, it also has feedback from sensors throughout engine. Thermocouples measure temperatures through the compressor, combustor diffusor, and after the turbines. RTD’s measure temperatures in the inlet as they are more robust. In the very hot oxidizing environment of the combustor and turbine section, optical pyrometers measure surface temperatures of blades, stators, and combustor liners. Pressure transducers are used throughout the engine for gas path total pressure, gas path static pressure, oil pressure, and fuel pressure measurements. For various necessities of bandwidth and precision, the transducers

are either remote mounted in the control unit with pressure taps, or mounted on engine with signal wires to the control unit [57]. Rotor speed pickups are variable reluctance pickups on the power turbine and gas generator shafts. Actuator position is measured with linear variable differential transformers as opposed to potentiometers for the superior mechanical robustness. Torque measurement is done with a phase shift torque meter on the output shaft. Finally, accelerometers will measure engine vibration for fatigue analysis and rotor imbalance checks.

FADEC operation starts with engine startup. The FADEC accelerates the engine to a stable operational speed. From here, a control loop has begun. The control loop first checks engine parameters to see if they are within operational limits. If they are all within limits, aircraft parameters and pilot inputs are collected from the aircraft serial bus. With current engine parameters and commanded settings, the FADEC calculates required fuel flows and actuator positions in order to accelerate, decelerate, or maintain current engine power. After this time step, the whole operation is performed again and the engine control loop is closed. Figure 12.2 shows the block diagram of the FADEC.

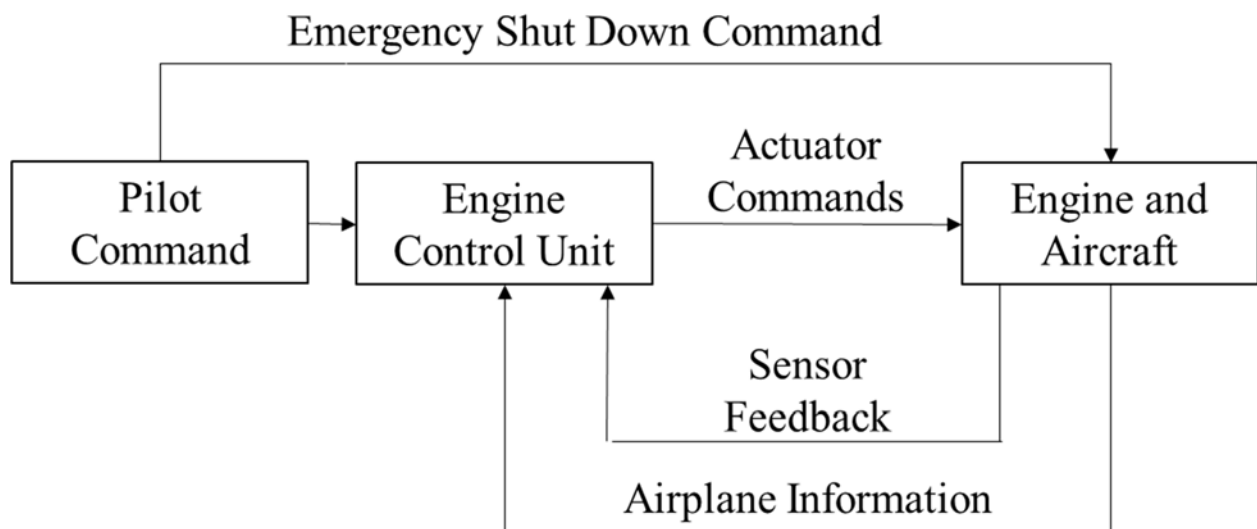


Figure 12.2: FADEC Block Diagram

12.3 Fuel System

The SF-1600 uses an electronically controlled fuel system, with signals from the full authority digital engine control (FADEC). FADEC replaces most of the hydro-mechanical and pneumatic engine controls used on older engines, like the baseline [55].

A low pressure system will pump the fuel from the fuel tanks and transfer it to the high pressure system. From the high pressure system the fuel will flow through the fuel injectors into the combustor. Both system will use fuel filters to protect the engine from foreign matter in the fuel. The engine will use a fuel oil heat exchanger (FOHE) to preheat the fuel, which increases combustion efficiency, while virtually eliminating the risk of ice formation in the fuel [56].

13.0 Engine Airframe Integration

The SF-1600 will be mounted in the nose of the next generation fighter trainer, similarly to the mounting of the PT-6 in the Pilatus PC-21. A frame mounted to the fore pressure bulkhead will then connect to the aft ring frame of the engine. The SF-1600 bracket will attach to the forward pressure bulkhead at 4 points. Typical mounting brackets attach to the engine ring frame with a U-shaped or O-shaped portion of the bracket, shown in the figures below.

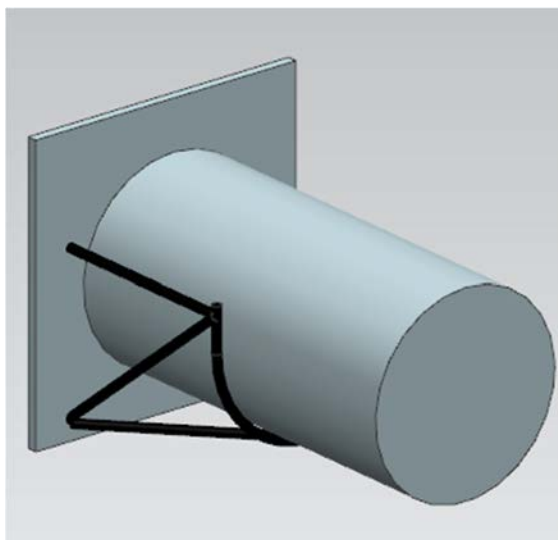


Figure 13.2: U-Shaped Mount

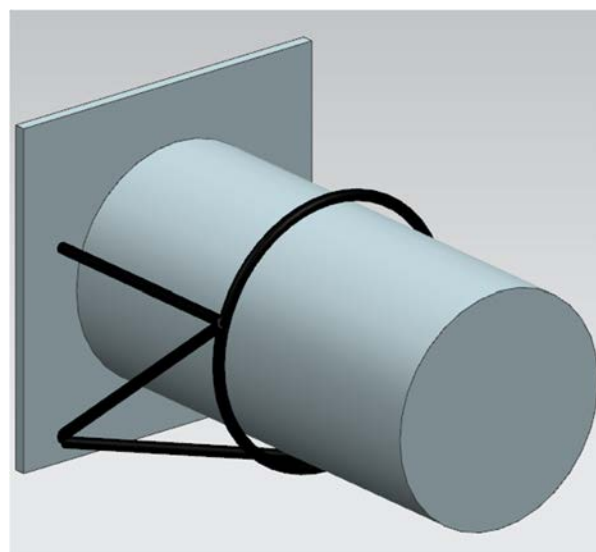


Figure 13.2: O-Shaped Mount

The aft engine ring frame is connected to the bracket with either two or three bolts, depending on the structural requirements. The frame is sized to accommodate the acoustic, gyroscopic, thermal, vibrational, cruise, maneuvering and any additional loads.

14.0 **SF-1600 Exploded View**

Table 14.1: SF 1600 Exploded View Material Legend

Color	Material
Plum	CBS-600
Silver	Ti-5 Al-2.5 Sn
Brown	CMC
Green	Fiberglass
Blue	Ni-22
Crimson	M50NiL

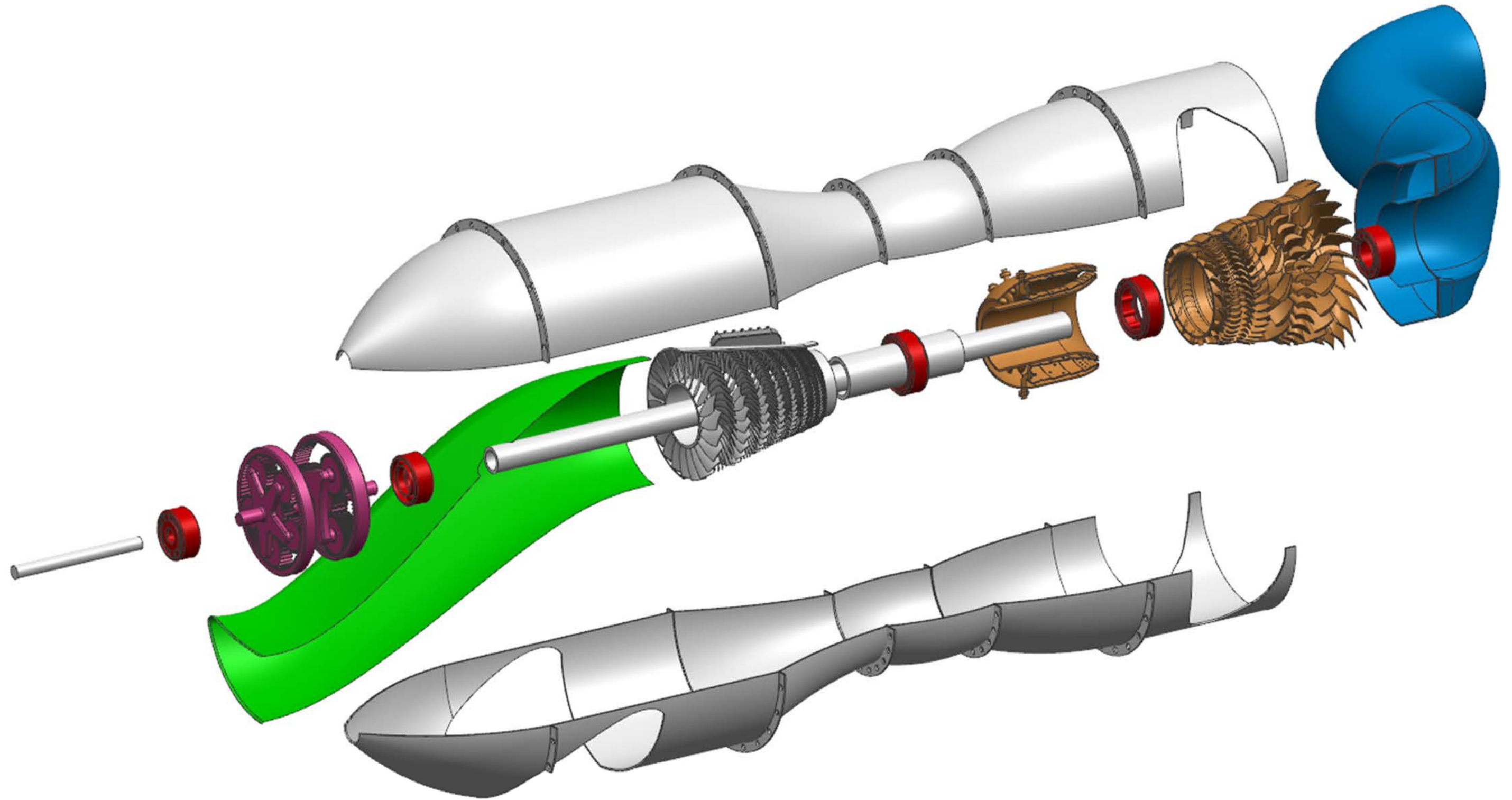


Figure 14.1: SF-1600 Exploded View

References

1. American Institute of Aeronautics and Astronautics, "Candidate Engines for a Next Generation Single-Engine Turboprop Aircraft", 2016-2017 AIAA Undergraduate Team Engine Design Competition
2. Kurzke, Joachim, "GasTurb 12: A Design & Off-Design Performance Program for Gas Turbine,"[<http://www.gasturb.de>], GasTurb GmbH, Templergraben 55, 52062 Aachen, Germany, 2012.
3. Jackson DJ, Lee KL, Ligrani PM, Johnson PD. Transonic Aerodynamic Losses Due to Turbine Airfoil, Suction Surface Film Cooling. ASME. J. Turbomach. 1999;122(2):317-326. doi:10.1115/1.555455.
4. Anon., "MatWeb Material Properties AS-N610," MatWeb Web Site, [<http://www.matweb.com/search/DataSheet.aspx?MatGUID=e11fa5d9f9c649c9a766ee721bfc4c98>], Spring, 2017.
5. Benzakein, M. J., GE Aircraft Engines "The Future of the Jet Engine," Cincinnati, OH, USA, Spring, 2017.
6. Farokhi, S., Technical Conversation, "Maximum Allowable Pressure Ratio for a Single Spool," Lawrence, KS, 2017.
7. Farokhi, S., "*Aircraft Propulsion.*" 2nd Edition, John Wiley & Sons Ltd, West Sussex, United Kingdom, 2014. Print.
8. Kundu, A., "*Theory and Practice of Aircraft Performance,*" 1st Edition, John Wiley & Sons Ltd, West Sussex, United Kingdom, 2016, Print.
9. Kurzke, J, GasTurb. Computer software. Gasturb GmbH, n.d.
10. Farokhi, S. "Shortcourse Notes on Preliminary Inlet Sizing and Engine Matching." University of Kansas Department of Aerospace Engineering. Lawrence, KS. 2017
11. Ahmed F. El-Sayed and Mohamed S. Emeara (2016) Aero-Engines Intake: A Review and Case Study. J Robot Mech Eng Resr 1(3): 35-42.
12. Rosenthal, H., D. Nelepovitz, and H. Rockholt. De-Icing of Aircraft Turbine Engines. Tech. no. DOT/FAA/CT-87 /37. N.p.: n.p., n.d. Print.
13. Farokhi, S. "The Helmholtz Resonator," University of Kansas Department of Aerospace Engineering, Lawrence, KS, 2017.
14. Hale, R., Private Communication, March 2017
15. Kurzke, J., "GasTurb 11," GasTurbine Performance, GasTurb Website, 15 May 2011, [<http://www.gasturb.de/index.html>] 22 January 2017.
16. Mattingly, J. and W. Heiser and D. Pratt, Aircraft Engine Design, 2nd ed., AIAA Education Series, Reston, VA, 2002
17. Dixon, S., Fluid Mechanics, Thermodynamics of Turbo-machinery, 3rd ed., Pergamon, Oxford, 1979
18. Wisler, D.C., "Advanced Compressor and Fan Systems," Short course notes on Aero-Propulsion Systems, April 2000.
19. Farokhi, S., Private Communication, February 2017.
20. Farokhi, S., "Excerpt from Aircraft Propulsion Notes: Compressor," The University of Kansas Department of Aerospace engineering, Lawrence, KS, 2016.
21. Farokhi, S., "Excerpt from Aircraft Propulsion Notes: Axial Length Estimation," The University of Kansas Department of Aerospace engineering, Lawrence, KS, 2016.
22. Farokhi, S., "Excerpt from Aircraft Propulsion Notes: Axial Compressor Design Principles," The University of Kansas Department of Aerospace engineering, Lawrence, KS, 2016.

-
23. Benzakein, M. J., "The Future of the Jet Engine," Cincinnati, Ohio GE Aircraft Engines.
 24. Levy, D., "Ceramic Matrix Composites Take Flight in LEAP Jet Engine," PHSX.ORG Website [https://phys.org/news/2017-01-ceramic-matrix-composites-flight-jet.html] PHSX.ORG, 24 February 2017, 12:35 pm.
 25. Lefebvre, H.A. and Ballal, R. D., Gas Turbine Combustion, 3rd Edition, CRC Press, Boca Raton, FL 33487, 2010.
 26. Hossaini, M. K., "Chapter 6: Review of the New Combustion Technologies in Modern Gas Turbines," Progress in Gas Turbine Performance, InTech Online Publishing, June 2013.
 27. Kellner, T., "World's First Plant to Print Jet Engine Nozzles in Mass Production," GE Reports, July 2014.
 28. Conner, J., "Maintaining Airworthiness Limitations for Life-Limited Parts in Mature Engines," GE Aviation, 2014.
 29. . Anon. "Dry Air Properties." The Engineering ToolBox. The Engineering ToolBox, n.d. Web. 18 Mar. 2017.
 30. Fligg, J. A., "Tests of a Low Speed Three-Stage Axial Flow Compressor at Aspect Ratios of One, Two and Four", AIAA Second Propulsion Joint Specialist Conference, 13-17 June 1966, Colorado Springs, Colorado.
 31. Farokhi, S., "A Discussion on Turbines", The University of Kansas Aerospace Engineering Department. 4:00-4:30pm, February 21, 2017.
 32. MacLean, C., "Effects of Real Fluid Properties on Axial Turbine Meanline Design and off-Design Analysis", Diss. Carleton U, 2012, Ottawa.
 33. "Fixed Shaft Turboprop Engine." Imgrum. N.p., n.d. Web. 14 Mar. 2017.
 34. "Jane's All the World Aero Engines." Jane's Aero Engines | IHS Markit. N.p., n.d. Web. 06 Mar. 2017.
 35. McIntire, W. L., and D. A. Wagner. "Next Generation Turboprop Gearboxes," ASME Digital Collections. American Society of Mechanical Engineers, 18 Apr. 1982. Web. 14 Mar. 2017.
 36. Dudley, Darle W., Stephen P. Radzevich, and Darle W.. Dudley. Dudley's Handbook of Practical Gear Design and Manufacture. 2nd ed. Boca Raton, FL: CRC, 2012. Print.
 37. Kerrebrock, Jack L. Aircraft Engines and Gas Turbines. 2nd edition. MIT Press, Cambridge, MA, 1992.
 38. The Editors of Encyclopædia Britannica. "Ball Bearing." Encyclopædia Britannica. Encyclopædia Britannica, Inc., 25 Sept. 2008. Web. 26 Feb. 2017.
 39. Clark J. Daniel, Jensen J. Mark, Montague T. Gerald, An Overview of Magnetic Bearing Technology for Gas Turbine Engines. University of Toledo, U.S. Army Research Laboratory. 2004.
 40. Nishikawa, Takashi. Hayashi, Nao. Hayakawa, Akiko. Technical Trend of Aircraft Bearings, NTN Kuwana Works, NTN Technical Review No. 82. 2014.
 41. Carey, Steve, and Dan Herring. "Low-Pressure Carburizing Process of M50 NiL." Heat Treating Progress. N.p., May/June 2007. Web. 26 Mar. 2017
 42. "AISI 4340 Steel, Normalized." ASM Material Data Sheet. N.p., n.d. Web. 28 Mar. 2017.
 43. "Steel M50NiLYW" Aubert & Duval. N.p., 6 Mar. 2017. Web. 28 Mar. 2017.
 44. Halbig, M. "Ceramic Matrix Composites for Rotorcraft Engines." (1980): n. pag. National Aeronautics and Space Administration. NASA, 15 Mar. 2011. Web. 10 Feb. 2017.
 45. Anon. "GE Successfully Tests World's First Rotating Ceramic Matrix Composite Material for Next-Gen Combat Engine." GE Website, 10 Feb. 2015. Web. 28 Feb. 2017.
-

-
46. Hurst, J., D. Zhu, and R. Bhatt. CMC Combustor Liner Development within NASA's Environmentally Responsible Aviation Project (n.d.): n. pag. NASA, 2012. Web. 2017.
 47. Halbig, M., Jaskowiak M., Kiser J., and Dongming Z. "Evaluation of Ceramic Matrix Composite Technology for Aircraft Turbine Engine Applications." *Composites 22.1* (1991): 73. NASA. Web. 10 Feb. 2017.
 48. PENG, H. "Manufacturing Titanium Metal Matrix Composites by Consolidating Matrix Coated Fibres." University of Bristol, 20 June 2005. Web. 15 Feb. 2017.
 49. "Metal Matrix Composites." University of Princeton, n.d. Web. 2017.
 50. Singh, R. *Composites Manufacturing*. Bombay: Indian Institute of Technology Bombay, n.d. IIT Bombay. Web. 2017.
 51. Bhadeshia, H. "Nickel Based Superalloys." *Nickel Based Superalloys*. University of Cambridge, n.d. Web. 20 Feb. 2017.
 52. "Jet Aircraft Engine Lubrication Systems." Navy BMR. N.p., n.d. Web. 25 Mar. 2017.
 53. "AeroShell Synthetic Turbine Oil 500 Data Sheet." Global Industrial Solutions. N.p., n.d. Web. 27 Mar. 2017.
 54. Rolls-Royce, "The Jet Engine" 5th Edition, John Wiley & Sons Ltd, West Sussex, United Kingdom, 2015. Print.
 55. Lee, C.C. and Boedicker, C. "Subsonic Diffuser Design and Performance for Advanced Fighter Aircraft", AIAA Paper Number, AIAA-85-3037, 1985.
 56. "Style 6781 S2-Glass." *Fibre Glast*. N.p., n.d. Web. 23 Apr. 2017.
 57. "PAMG-XR1 5052 Aluminum Honeycomb, AMS C7438." *Plascore*. N.p., n.d. Web. 11 Apr. 2017.
 58. "Inlet Performance." NASA. NASA, n.d. Web. 24 Apr. 2017.
 59. Thurber, M., "Finally, Autothrottles for the PT6," AIN Online Web Site [<http://www.ainonline.com/aviation-news/business-aviation/2015-11-17/finally-autothrottles-pt6>] AIN Online, 2015.
 60. Anon., *Aviation Maintenance Technician Handbook-Powerplant Volume 1*, U.S. Department of Transportation, Federal Aviation Administration, 2012.
 61. Halbig, M., Jaskowiak M., Kiser J., and Dongming Z. "Evaluation of Ceramic Matrix Composite Technology for Aircraft Turbine Engine Applications." *Composites 22.1* (1991): 73. NASA. Web. 10 Feb. 2017.
 62. Burnette, Heyward. "Ceramic Matrix Composite Seals Proving Reliable for Jet Engine Nozzles." Wright-Patterson Air Force Base. Air Force, 19 Sept. 2008. Web. 25 Mar. 2017
 63. "Prepreg Process." Hexion.com - Prepreg - Hexion Processing R& D Meets Manufacturers' Need for Speed - Automotive Process. N.p., n.d. Web. 20 Apr. 2017.
 64. Hurst, J., D. Zhu, and R. Bhatt. CMC Combustor Liner Development within NASA's Environmentally Responsible Aviation Project (n.d.): n. pag. NASA, 2012. Web. 2017.
 65. Klaas, O., "Modeling of Integrally Bladed Rotor (IBR) Blends." [http://www.navysbir.com/13_A/36.htm]. N.p., n.d. Web. 1 Apr. 2017.
 66. Maciejczyk, Andrzej, and Zbigniew Zdziennicki. "DESIGN BASIC OF INDUSTRIAL GEAR BOXES." *CYBRA - Lodz Regional Digital Library*. N.p., n.d. Web. 27 Feb. 2017.
 67. "Gear Design." *NC State Engineering in Havelock*. N.p., n.d. Web. 22 Apr. 2017.
 68. "CBS-600 Carburizing Bearing and Gear Steel." *MatWeb: Material Property Data*. N.p., n.d. Web. 22 Apr. 2017.
 69. Raymer, Daniel P., "Aircraft Design: A Conceptual Approach". AIAA Education Series. Washington D.C. 1989. Print.